Jonas Crosby

Ultrasound-based quantification of myocardial deformation and rotation

Thesis for the degree of Philosophiae Doctor

Trondheim, February 2009

Norwegian University of Science and Technology
Faculty of Medicine
Department of Circulation and Medical Imaging

NTNU
Norwegian University of
Science and Technology

NTNU
Norwegian University of Science and Technology

Thesis for the degree of Philosophiae Doctor

Faculty of Medicine
Department of Circulation and Medical Imaging

ISBN 978-82-471-1435-3 (printed ver.)
ISBN 978-82-471-1436-0 (electronic ver.)
ISSN 1503-8181

Doctoral theses at NTNU, 2009:33

Printed by NTNU-trykk

Ultralydbasert tallfesting av hjertemuskelens deformasjon og rotasjon

I dette doktorgradsarbeidet er det blitt utviklet nye ultralydbaserte metoder for å vurdere hjertefunksjonen.
Hjertets rotasjon er foreslått som en mulig indikator på hjertesykdom, men i dag er magnetisk resonansavbildning (MR-avbildning) eneste klinisk tilgjengelige metode for å måle hjertets rotasjon. Da avbildning med MR er forholdsvis tidkrevende og kostbart, og har lav bilderate, ville det være hensiktsmessig med et ultralydbasert alternativ. Vevsdoppler og speckle-tracking er to ultralydmetoder for å måle bevegelsen i hjertet. Vevsdoppler måler hastigheten til kroppsvev i forhold til ultralydmottakeren basert på dopplerskiftet, og speckle-tracking er en teknikk som følger det karakteristiske mønsteret i ultralydbildet fra bilde til bilde. Denne avhandlingen viser hvordan disse metodene kan utnyttes til å måle rotasjon av hjertet. De nye metodene har blitt prøvd ut på friske og syke hjerter, og har vist seg å gi målinger som samsvarer med MR-metoden.
Mens konvensjonell medisinsk ultralyd bare avbilder et snitt av hjertet, har det nylig blitt lansert ultralydmaskiner med mulighet for å samle inn data i tre dimensjoner (3D). Speckle-tracking basert på konvensjonelle todimensjonale ultralydbilder har vært begrenset av at vevet flytter seg inn og ut av avbildningsplanet, mens det med 3D volumavbildning vil være mulig å følge de samme materielle punktene i vevet over tid. I dette doktorgradsarbeidet er derfor speckle-tracking metoden blitt utvidet til å følge hjertebevegelsen i 3D. Den nye metoden har blitt testet på syntetiske ultralyddata samt demonstrert på et utvalg personer med karakteristisk hjertefunksjon, der den klarte å skille mellom friskt og sykt hjertevev.
Det er ofte vanskelig å teste ut nye metoder for å måle bevegelsen i hjertet, da det sjelden finnes en kjent fasit. Det har derfor de siste årene blitt etablert metoder for å generere virkelighetsnære syntetiske ultralydbilder basert på matematiske modeller av hjertet, der bevegelsen er kjent. Disse modellene har ikke klart å gjenskape variasjonen i intensitet som man ser i hjerteveggen i virkelige ultralydbilder. I dette doktorgradsarbeidet er det derfor blitt utviklet en ny metode for å modellere hjertet som tar hensyn til den varierende retningen på muskelfibrene gjennom veggen, og det viser seg at denne gjør det mulig å forklare de observerte intensitetsforskjellene.

Kandidat:	Jonas Crosby
Institutt:	Sirkulasjon og bildediagnostikk
Hovedveileder:	Hans Torp
Biveiledere:	Espen W. Remme og Bjørn Skallerud
Finansieringskilde:	Strategisk universitetsprogram i medisinsk teknologi

Overnevnte avhandling er funnet verdig til å forsvares offentlig for graden philosophiae doctor (PhD) i medisinsk teknologi. Disputas finner sted i auditoriet, Medisinsk-teknisk forskningssenter, fredag 20. februar 2009, kl. 12:15.

Abstract

The overall aim of this thesis was to provide new non-invasive methods for assessing the contractile function of the heart. More specifically, the thesis work has been concentrated on methods for measuring deformation and rotation for use with echocardiography. Left ventricular deformation and rotation are quantities that are closely related to contractility, and are expected to give valuable diagnostic and prognostic information.

Although noninvasive measurements of LV rotation have been attainable using tagging techniques in magnetic resonance imaging (MRI), the clinical use of this method has been limited by low frame rate, high costs, and limited availability. Two new ultrasound-based methods for measuring left ventricular (LV) rotation in short-axis images of the left ventricle have therefore been developed in this project: A speckle tracking method and a tissue Doppler method. The speckle tracking method estimates LV rotation based on frame-to-frame block-matching of a set of tracking regions placed within the LV wall in conventional B-mode (brightness-mode) images. The tissue Doppler method utilizes the velocity field provided by tissue Doppler imaging (TDI) to estimate LV rotation. Application of the methods to estimate left ventricular twist in healthy and pathological heart showed results comparable with measurements by MRI in terms of agreement and repeatability, except for a systematic underestimation of absolute rotation for the tissue Doppler method.

An extension of the speckle tracking method for tracking LV deformation in 3D full-volume ultrasound data has also been developed. Tracking in three dimensions overcomes the problem with out-of-plane motion, which is an inherent limitation in tracking based on conventional two-dimensional images. However, tracking in full-volume ultrasound data is made difficult by lower temporal resolution and generally poorer image quality. The method was tested in simulated ultrasound data and on a small selection of human subjects with adequate image quality, where it successfully distinguished between pathological and healthy LV segments. However, the method has to be validated in a larger unselected population before any conclusions on its clinical value could be made.

Recent improvements in hardware and software have made it possible to obtain realistic computer-simulated ultrasound data that could be used in the development and testing of tracking methods. However, the existing models of the left ventricle have not reproduced the inhomogeneous distribution of backscatter intensities seen within the walls of the heart in real echocardiograms. As a part of this thesis work, a refined model of the left ventricular wall was developed that incorporated the structural anisotropy of cardiac muscle fibers by inducing an increased correlation of the point scatterers in the local directions of the fibers. The methodology was used to model an excised specimen from the septal wall of a pig's heart, where the simulation successfully reproduced the angle dependent variation in backscatter intensities.

Preface

This thesis is submitted in partial fulfilment of the requirements for the degree *philosophiae doctor* (PhD) in Medical Technology at the Norwegian University of Science and Technology (NTNU). The present work was carried out at the Department of Circulation and Medical Imaging in the years 2003 to 2008. The research project was funded by the Norwegian Research Council as a part of the Strategic University Programme in Medical Technology at NTNU (Phase II 2003-2008). In addition, Rikshospitalet University Hospital in Oslo has given financial support for parts of the project.

My main supervisor has been professor Hans Torp, who also is the one responsible for coaxing me into pursuing a PhD degree. His expertise and professional insight has been crucial for the project. Being a real full time professor, Hans is capable of giving instant e-mail feedback on drafts sent past midnight. Co-supervisors have been Professor Bjørn Skallerud at the Department of Structural Engineering at NTNU, whom was mostly involved in the early stages of the project, and Espen Remme at Institute for Surgical Research at Rikshospitalet, who agreed to guide me in the finalization stage of the project.

It has been a privilege to work in the ultrasound research group in Trondheim, surrounded by dedicated, capable and pleasant colleagues. Especially, I would like to thank Torbjørn Hergum, whom has — with help from his faithful server — provided me with a vast amount of simulated ultrasound data; Svein Arne Aase and Tore Bjåstad for sharing their knowledge; and Lasse Løvstakken for being such an exemplary office mate.

On the clinical side, I have had the pleasure of a long and exciting collaboration with Brage H. Amundsen. Brage constitutes a quiet momentum that makes things happen. I would also thank Thomas Helle-Valle and his colleagues at Rikshospitalet in Oslo for the fruitful collaboration on left ventricular twist and rotation.

Furthermore, I am grateful to the developers at GE Vingmed Ultrasound AS for providing access to ultrasound hardware and software, and for kind technical support. Looking back, I can not think of anyone employed in the Trondheim and Oslo offices that has not helped me in one way or another, but I would in particular emphasize the indefatigable GcMat assistance from Svein Brekke, and the assistance with the ultrasound simulations from Stian Langeland.

Radiographer Per Arvid Steen at the Department of Medical Imaging at St. Olavs Hospital has been the key figure when we needed to achieve tagged MR images, and I am also thankful for the help from Jørn Kværness at Philips Medical Systems Nordic in this process. Likewise, Professor Atle Bjørnerud and Dr. Frédéric Courivaud at the Interventional Center at Rikshospitalet have helped us to assess MR diffusion tensor images of the heart. Associate Professor Ivar Skjåk Nordrum, at Department of laboratory medicine at NTNU has kindly helped us with the preparation of porcine hearts.

Finally, a special thanks is reserved for my wife, Bente, for being there. Always.

Oslo, September 2008

Jonas Crosby.

Table of Contents

Introduction: **1**

1 Motivation and aims of study **1**

2 Background **5**
2.1 Cardiac structure and deformation 5
2.1.1 Gross Function 5
2.1.2 The cardiac cycle 6
2.1.3 Cardiac structures 6
2.2 Ultrasound imaging 13
2.2.1 Ultrasonic pulse-echo imaging 13
2.2.2 Tissue Doppler imaging 17
2.2.3 Full volume imaging 18
2.3 Tracking methodology 20
2.3.1 Speckle 20
2.3.2 Speckle tracking 21
2.3.3 Similarity measures in block matching 23
2.3.4 Optical flow 25
2.4 Left ventricular rotation and strain 25
2.4.1 Rotation, twist and torsion 25
2.4.2 Strain and deformation 28
2.5 Reference methods 31
2.5.1 Magnetic resonance imaging (MRI) 31
2.5.2 Sonomicrometry 36

3 Contributions **39**
3.1 Methods for ultrasound-based quantification of rotation and twist . . . 39
3.2 Quantification of deformation and rotation in 3D ultrasound data . . . 41
3.3 Improving simulated ultrasound images 42

4 General discussion and future directions **45**
4.1 Methods for ultrasound-based quantification of rotation and twist . . . 47
4.2 Quantification of deformation and rotation in 3D ultrasound data . . . 52
4.3 Improving simulated ultrasound images 53

5 Conclusions **55**

List of publications **57**

References **59**

Papers: 67

A New Noninvasive Method for Assessment of Left Ventricular Rotation: Speckle Tracking Echocardiography. **67**
Circulation,112(20):3149-3156, 2005
T. Helle-Valle, J. Crosby, T. Edvardsen, E. Lyseggen, B.H. Amundsen, H.-J. Smith, B.D. Rosen, H. Torp, H. Ihlen, and O. Smiseth

A.1 Introduction . . . 67
A.2 Methods . . . 68
A.2.1 Experimental study . . . 68
A.2.2 Clinical study . . . 71
A.2.3 Reproducibility of the STE method . . . 72
A.2.4 Statistical analysis . . . 72
A.3 Results . . . 72
A.3.1 LV rotation and torsion by STE versus sonomicrometry: Experimental study . . . 72
A.3.2 LV rotation and torsion by STE versus MRI tagging: Healthy humans . . . 77
A.3.3 Effect of pericardiotomy on LV rotation and torsion . . . 78
A.3.4 Interobserver variability . . . 80
A.4 Discussion . . . 80
A.4.1 Apical rotation . . . 81
A.4.2 Basal rotation . . . 81
A.4.3 Comparison with previous studies . . . 82
A.4.4 Limitations . . . 82
A.5 Conclusions . . . 84
A.6 Acknowledgements . . . 84
References . . . 84

B A new Tissue Doppler Method for Examination of Left Ventricular Rotation **89**
Ultrasound Med. Biol., 2008 [available online]
J. Crosby, B.H. Amundsen, T. Helle-Valle, P.A. Steen, and H. Torp

B.1 Introduction . . . 89
B.2 LV rotation by TDI . . . 90
B.2.1 Rotation from two tangential velocities (TDI_0) . . . 90
B.2.2 The extended TDI method (TDI_1) . . . 90
B.3 Methods . . . 93
B.3.1 Study sample . . . 93
B.3.2 Definitions . . . 93

B.3.3 Echocardiography . . . 93
B.3.4 MRI tagging . . . 94
B.3.5 Statistics . . . 94
B.4 Results . . . 94
B.4.1 Agreement . . . 98
B.4.2 Regional rotation . . . 101
B.4.3 Reproducibility . . . 102
B.5 Discussion . . . 103
B.5.1 Agreement . . . 103
B.5.2 Regional rotation . . . 105
B.5.3 Reproducibility . . . 105
B.5.4 Limitations . . . 106
B.6 Conclusions . . . 106
B.7 Acknowledgements . . . 106
References . . . 106

C 3D Speckle Tracking for Assessment of Regional Left Ventricular Function 109
Accepted for publication in Ultrasound Med. Biol., 2008
J. Crosby, B.H. Amundsen, T. Hergum, E.W. Remme,
S. Langeland, and H. Torp
C.1 Introduction . . . 109
C.2 Methods . . . 111
C.2.1 The 3D speckle tracking algorithm . . . 111
C.2.2 Generation of synthetic ultrasound data . . . 112
C.2.3 Testing of the algorithm on synthetic data . . . 114
C.2.4 Testing of the algorithm on human data . . . 116
C.3 Results . . . 116
C.3.1 Testing of the algorithm on synthetic data . . . 116
C.3.2 Testing of the algorithm on human data . . . 121
C.4 Discussion . . . 124
C.4.1 General discussion of the 3D speckle tracking algorithm . . . 124
C.4.2 Testing of the algorithm on synthetic data . . . 126
C.4.3 Testing of the algorithm on human data . . . 126
C.4.4 Limitations . . . 127
C.5 Conclusions . . . 128
C.6 Acknowledgements . . . 128
References . . . 128

D The Effect of Including Myocardial Anisotropy in Simulated Ultrasound Images of the Heart. 133
Accepted for publication in IEEE Trans. Ultrason. Ferroelectr. Freq. Control, 2008
J. Crosby, T. Hergum, E.W. Remme and H. Torp
D.1 Introduction . . . 133

D.2 Background 136
D.3 Method 137
D.3.1 Data acquisition and fiber angle estimation 139
D.3.2 Point scatterer model 140
D.3.3 Ultrasound simulation 141
D.4 Results 142
D.5 Discussion and conclusion 142
References 147

Chapter 1

Motivation and aims of study

A world of broken hearts. The heart is the workhorse of the human body. Assuming an average frequency of 70 beats per minute and a stroke volume of 70 ml, the cardiac cycle of contraction and relaxation is repeated more than 100.000 times per day, which gives a daily pumping volume of 7000 liters. Although this flow capacity can be matched by man-made pumps, the additional specifications – life-long maintenance-free non-stop operation that adapts to the changing need of the body while pumping an oxygen-rich fluid at a pressure of 16 kPa without damaging the blood cells — could make an industrial pump supplier turn pale. But every now and then hearts malfunction, mainly due to blocked or reduced blood supply to the cardiac muscle cells and surrounding tissue, summing up to be the main cause of death in developed countries today (WHO, 2002). The stunning or death of cardiac muscle (myocardium) leads to structural and functional changes in the heart that may be evaluated non-invasively by a cardiologist using imaging modalities as cardiovascular Magnetic Resonance Imaging (MRI), Computed Tomography (CT), or echocardiography. Due to availability, portability, safety and low operating cost associated with ultrasound scanners, echocardiography has become the primary cardiac imaging modality.

Quantifying cardiac function. In echocardiography, evaluation of the myocardial function has traditionally been done by visual interpretation of the apparent motion in the ultrasound image. This is — and will continue to be — a powerful approach for skilled echocardiologists to obtain information about cardiac function (Silcocks et al., 1997). However, there are a number of reasons for agreeing on a set of standardized quantitative measures. Standardized measures allow the cardiologist to use optimal threshold values based on statistics from large clinical trials as guidance for their decision-making. It also makes it easier to communicate the results from an ultrasound examination to other medical professionals, even if they are not trained in echocardiography. Standardized measurements also makes it easier for less experienced sonographers to perform ultrasound examinations, and thereby reduce the risk of misdiagnosis. Moreover, quantitative measures are suitable for documentation, allowing the hospital to learn from experience. The establishing of quantitative measurements in echocardiography has the additional advantage that they prepare the grounds for automated methods. In many cases, automatic or semi-automatic measurements can reduce the time needed to obtain measurements, and relieve the sonographer/cardiologist from tedious routine procedures. This can lead to reduced costs, increased number of examinations, or an increased number of measurements to support the decision-making. In many cases automated methods

would make the measures less dependent on the user, decreasing the inter- and intra-observer variabilities. Automatization aids standardization, and might also simplify the ultrasound examination so that routine examinations can be performed by less experienced sonographers.

The quest for clinically useful parameters. In this thesis, the information of interest is the true deformation of the cardiac myocardium. However, the deformation pattern of the myocardium is quite complex, and the number of parameters needed to describe this deformation is far beyond what's meaningful in a diagnostic decision-making process. What clinicians (and patients) need is a few parameters that could provide information of the state of the examined heart and that can be reliably measured in the largest possible percentage of the patient population. It is also uttermost important that invalid results can be detected so that these are not used in the decision-making. The particular parameters to be used will most probably depend on the particular case of application, and finding good candidates is the goal of many research studies. The role of engineers in this process is to provide the algorithms, software and hardware needed to measure a larger selection of parameters, so that their clinical value can be determined in experimental and clinical trials. As the measurements in ultrasound will often be limited by the measurement process, it is also important that these limitations are communicated to the clinicians.

It's just an image. Like all medical imaging modalities, ultrasound imaging is based on the interaction of wave energy with human tissue (or with an induced contrast medium). In ultrasound pulse-echo imaging, some of the energy in the propagating sound waves is reflected or scattered due to local variations in the density ρ and compressibility κ, giving rise to redirected sound waves that can be detected and displayed as an image. As abrupt variations in density and compressibility often is related to tissue boundaries, the ultrasound image can be used to obtain meaningful structural information of the body. Likewise, information of the motion and deformation of the structures can be obtained by the temporal changes in the reflected waves. The actual appearance of the ultrasound images will however depend on the characteristics of the imaging system as well as the actual structures.

Aims of study. Several ultrasound-based quantitative measures of cardiac function have been proposed. Most common is the ejection fraction (EF) based on measurements of changes in ventricular volume. Ejection fraction has shown to be a good indicator of global left ventricular function, but its ability to give information about the contractility of the cardiac muscle is unfortunately limited by its load-dependence (Robotham et al., 1991). The topic of this thesis is *Ultrasound-based quantification of myocardial deformation and rotation*, as deformation and rotation are expected to be more direct indicators of the contractile function and might also provide information of the regional performance of the cardiac muscle. LV rotation and torsion have been proposed as sensitive markers of LV function, but MRI tagging has been the only clinically available method to obtain these parameters. Myocardial

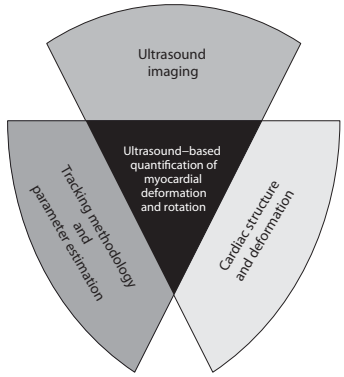

Figure 1.1: Ultrasound-based quantification of myocardial deformation and rotation. The estimates of deformation and rotation are functions of both the ultrasound imaging system and the choice of motion estimation methodology, in addition to the true underlying deformation and motion of the myocardial tissue.

deformation has been measurable based on two-dimensional ultrasound using methods such as Tissue Doppler Imaging (TDI) and speckle tracking. However, the development of commercial matrix ultrasound arrays capable of acquiring volume data makes it possible to measure deformation in three-dimensions.

The aims of this thesis can thus be summarized as follows:

Aim 1: To develop and investigate methods for quantification of rotation and twist based on short-axis ultrasound images of the left ventricle.

Aim 2: To extend the speckle tracking method to be able to measure deformation and rotation in full-volume ultrasound data of the left ventricle.

Aim 3: To investigate and discuss fundamental limitations associated with ultrasound-based assessment of left ventricular deformation and rotation.

The developed methods should be applicable to existing commercial state-of-the-art ultrasound scanners, and should be suited for clinical use.

Thesis outline

This thesis is organized in an introductory section followed by four self-contained papers. The introductory section consists of four chapters in addition to the present motivational chapter. Chapter 2 provides some information on the constituent parts of ultrasound-based estimation of deformation and rotation (Fig. 1.1), and some supplementary information on the different reference methods utilized in the main papers. In Chapter 3, a brief presentation of the scientific contributions of the PhD-project is given, followed by a general discussion in Chapter 4 and an overall conclusion in Chapter 5. The papers are presented in chronological order and are equivalent to the versions submitted to the journals, but layout and citations have been adapted to the general style of the thesis.

Chapter 2

Background

2.1 Cardiac structure and deformation

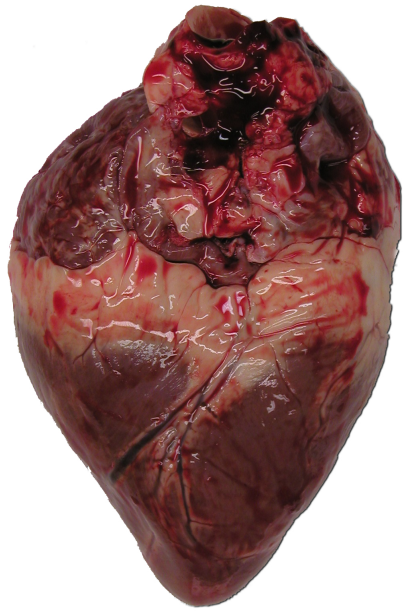

Figure 2.1: Porcine heart.

This section describes the anatomy and physiology of the human heart in general, and the behavior of the left ventricle in particular. The purpose is to obtain a physiological understanding of the system we want to measure.

2.1.1 Gross Function

Figure 2.1 shows the exterior of an excised porcine heart. The heart consists of two functional units: The left side pumps oxygenated blood from the lungs and out to all the cells of the body, while the right side of the heart pumps the returning oxygen-poor blood back to the lungs. Each half consists of two chambers, an atrium and a

ventricle.

The right atrium receives blood through three veins. The blood flows from the atrium through the tricuspidal valve and into the right ventricle. The ventricle ejects the blood through the pulmonary valve and into the pulmonary trunk.

The left atrium receives blood through four pulmonary veins. The blood flows from the atrium through the mitral valve and into the left ventricle. The ventricle ejects the blood through the aortic valve and into the aorta.

2.1.2 The cardiac cycle

The cardiac cycle is usually divided into two main phases: *Systole*, where the ventricles contracts and blood is driven into the aorta and the pulmonary artery; and *diastole*, where the ventricles dilates and fill with blood. Systole and diastole can be subdivided into the phases illustrated with echocardiograms in Tables 2.1 and 2.2. Figure 2.2 shows a modified Wiggers diagram that gives a qualitative summary of the changes in velocities, pressure and ventricular volume during one cardiac cycle. Due to the different pressure conditions, the exact timing of the cardiac events differ somewhat between the left and the right side. The ventricles do not empty completely during systole; the average left ventricular ejection fraction is 0.65 (Hess and Carroll, 2008), equivalent to a stroke volume of about 70 ml. Some of the residual end-systolic volume acts like a reserve, which can be utilized to increase stroke volume during exercise.

The contraction of the myocardium is triggered by an electrical potential that is initiated in a bundle of specialized muscle cells called the sinoatrial node (SA-node) in the upper lateral region of the right atrium. This potential propagates through the atrial myocardium leading to atrial contraction. When the potential reaches the atrioventricular node (AV-node) at the bottom of right atrium, it is slowed down by approximately 100 ms before it is conducted along the right and left bundle branches. Finally, the potential spreads through specialized fibres (Purkinje fibres), and to the myocardial cells, causing ventricular contraction. The propagation pathways governs the sequence of ventricular contraction. First, the intraventricular septum contracts. Then the activation of the rest of the two ventricles follows from apex to base and from endocardium to epicardium. The electrical activity of the heart can be easily measured using an electrocardiograph (ECG) which has become an invaluable tool in the diagnosis of several cardiac diseases, and especially in the diagnosis of abnormal cardiac rhythms. As the sequence of the electrical activation is of great importance for the overall performance of the pumping function of the heart, the electrical propagation pattern in the heart is also essential in the design and calibration of artificial pacemakers.

2.1.3 Cardiac structures

This subsection describes the anatomical features and physical properties of the main structure of interest in this thesis, namely the left ventricular myocardium. In addition, the subsection provides a brief review of the properties of other neighboring structures that might influence the ultrasound-based estimates of LV deformation and rotation.

Table 2.1: Cardiac phases — Systole

Cardiac Phases — Systole		
A4ch	Plax	Description

At the beginning of the systole the left ventricle is maximally dilated, the ventricular pressures are low and all four valves are closed.

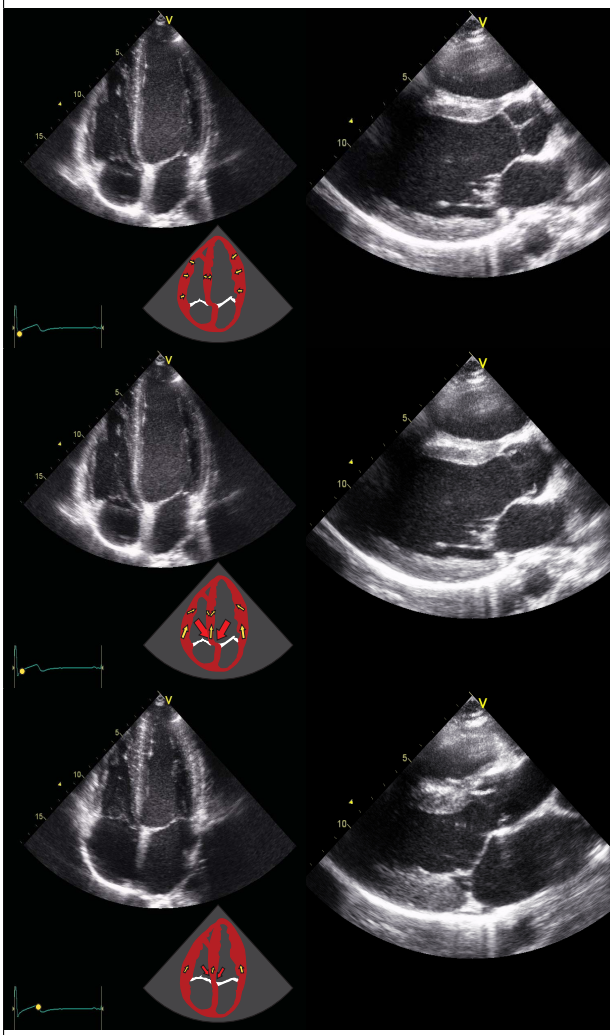

Isovolumic contraction. The ventricular contraction causes the pressure inside the ventricles to rise rapidly, but, as it still is lower than the pressure in the arteries, the aortic and pulmonary valves stay closed.
(Duration: $\sim 50\ ms$)

Maximum ejection. When the ventricular pressures exceed the arterial pressures the aortic and pulmonary valves open, blood from the ventricles streams into the arteries, and the ventricles contract. The end of the maximum ejection phase is defined by the peak ventricular pressures.
(Duration: $\sim 90\ ms$)

Reduced ejection. The reduced ejection is a result of reduced muscle contraction in the ventricles combined with less aortic compliance. Near the end of systole, the aortic pressure can be higher than the ventricular pressure but the aortic valve stays open due to inertia of the blood flow.
(Duration: $\sim 170\ ms$)

A4CH: Apical 4-chamber view; PLAX: Parasternal long-axis view;

The given phase durations are average values from adult men (Katz, 1992).

Table 2.2: Cardiac phases — Diastole

Cardiac Phases — Diastole		
A4ch	Plax	Description
At the onset of diastole the ventricular pressures decline rapidly. The pressure in the ventricles has dropped below the pressures in the aortic and pulmonary trunks, and the consequent deceleration of the blood flow leads to the closure of aortic and pulmonary valves.		
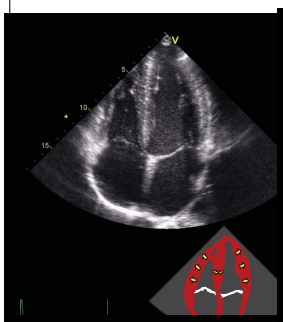	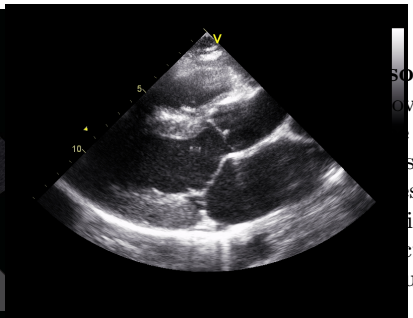	**sovolumic relaxation.** The ovolumic relaxation lasts from aortic and pulmonary valve sures, and until the ventricular ssures have fallen below the ial pressures and the mitral and cuspidal valves open. uration: $\sim 80\ ms$)
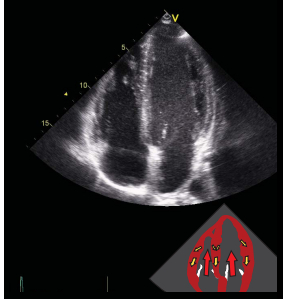	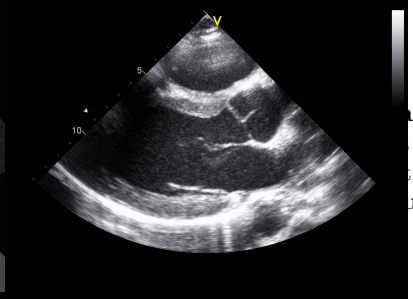	**pid inflow.** Blood from the atrium flows through the open ral valve and refills the ventricle. uration: $\sim 110\ ms$)
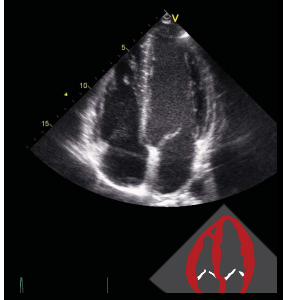	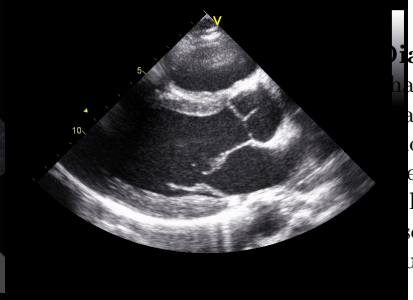	**iastasis.** The rapid inflow ase is followed by a quiescent ase called diastasis where the ow is considerably reduced. e diastasis shortens dramatically h increasing heart rate, and is ent at very high heart rates. uration: $\sim 190\ ms$)
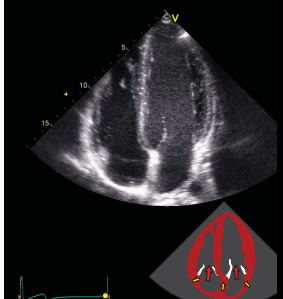	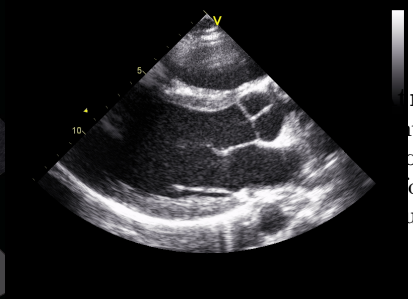	**rial systole.** The atrial walls tract, forcing a last flow of blood o the ventricle ("atrial kick") ore the mitral valve closes. uration: $\sim 110\ ms$)

A4CH: Apical 4-chamber view; given phase durations are average values adult men (Katz, 1992).

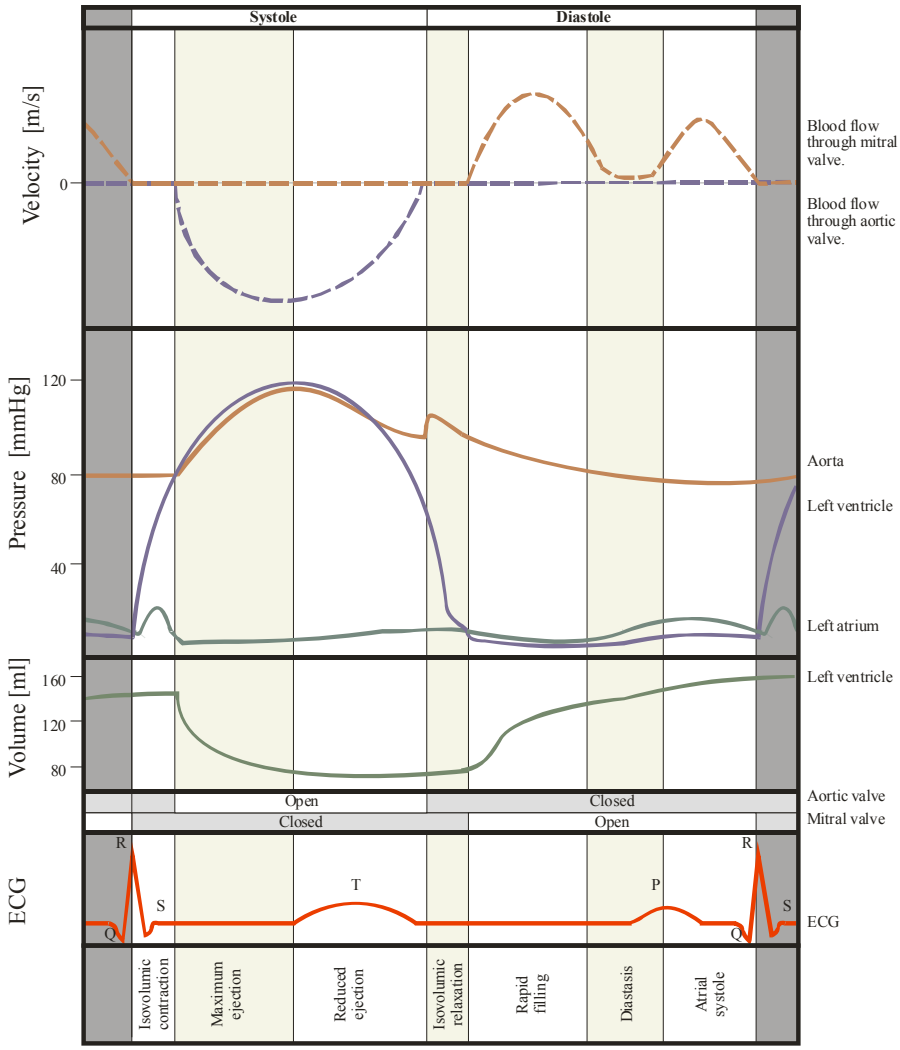

Figure 2.2: Wiggers diagram showing velocities, pressure and volume traces from one cardiac cycle of a healthy heart. (Based on diagrams in Bjålie et al. (2001) and Katz (1992)).

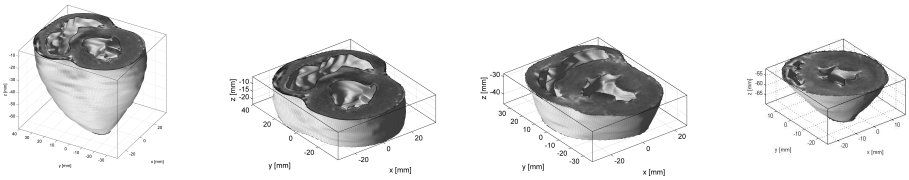

(a) Ventricles. (b) Basal slice. (c) Mid slice. (d) Apical slice.

Figure 2.3: Model of left and right ventricles based on MRI.

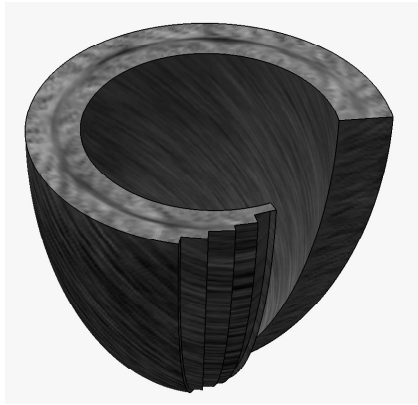

Figure 2.4: Schematic illustration of the fiber orientations in the left ventricular myocardium.

Left ventricular myocardium

The myocardium is a complex structure with density about 1.05 g/ml constituted of cardiac muscle cells (myocytes), coronary blood vessels, connective tissue (e.g. collagen and elastin) and interstitial fluid.

While the outer surfaces of the heart is quite smooth, the inner surfaces of the ventricles are mostly irregular due to the presence of *trabeculae carneae* that is projections of the myocardium into the ventricular lumen that gives the wall a ridgy appearance. However, a smooth region is found immediately below the aortic orifice. A set of characteristic stalks of myocardium — the papillary muscles — arise from the trabeculae in the distal part of the wall. Typically, two distinct papillary muscles can be observed within the left ventricle; most commonly located antero-laterally and postero-medially. The overall shape of the left ventricle resembles a truncated prolate ellipsoid. The LV walls are generally thicker than in the right ventricle, but the LV lateral wall is usually very thin at the apex. Figure 2.3 shows short-axis sections of the left and right ventricles constructed from MRI data.

Although the cardiac muscle have been thoroughly examined at both macroscopic

and microscopic scales, there is an ongoing dispute concerning the functional organization of the cardiac cells within the myocardial mass. A systematic review of the different views is given in Gilbert et al. (2007). The extensive branching of the cardiac muscle cells makes it difficult to capture the general three-dimensional organization based on small conventional two dimensional histological sections. Recently, efforts has been made to obtain larger reconstructed volumes by assembling a large set of confocal microscopy volume images in order to "bridge the scale gap" (Trew et al., 2006). In addition, diffusion tensor magnetic resonance imaging (DT-MRI, see Subsection 2.5.1) constitute a powerful technique to reveal the three-dimensional myocardial architecture in whole hearts.

The cardiac muscle cells (myocytes) have diameters of about $10 - 20\ \mu m$ and length about $50 - 150\ \mu m$ (Gilbert et al., 2007). This is much smaller than for skeletal muscle fibers that have diameters in the range $10 - 100\ \mu m$, and often have lengths of several centimeters. It has been found — both by histology and DT-MRI — that the orientations of the myocytes in the LV roughly follow a helical pattern spanning the entire length of the ventricle: Subendocardially, the myocytes constitute a right-handed helix. This helical configuration changes gradually through the wall, so that the myocytes becomes circumferentially oriented in the center of the wall, and ends up as a left-handed helix at the epicardium. This helical organization of the myocardial structure is illustrated in Fig. 2.4. In reality, there are large local deviations from this general description. Specifically, the myocytes are not necessarily parallel to the epicardial surface but might intrude into the thickness of the wall (Lunkenheimer et al., 2006). Furthermore, the cardiac myocytes are organized in layers about 4-5 cells thick separated by complex networks of interstitial collagen, fibroblasts and other components of the extracellular matrix (Trew et al., 2006). These layers run approximately radially through the LV wall, and follow the local helical myocyte orientations tangentially (LeGrice et al., 1995). Moreover, it has been suggested that the cleavage planes between these loosely coupled layers play a significant role in the LV wall thickening (LeGrice et al., 1995).

Samples of myocardial tissue have been shown to exhibit stress relaxation under maintained stretch and creep under maintained stress, which implies that the resting myocardium can be considered a *viscoelastic* material (Fung, 1981). The variation of myocardial volume due to coronary flow is likely to be less than one percent during a cardiac cycle (Spaan, 1985), so the myocardial volume is generally regarded as incompressible. However, it has been argued that soft tissue like the myocardium, consisting of fluid in an extracellular matrix of connective tissue, might behave like a *poroelastic* material, meaning that blood and interstitial fluid can move within the myocardium when exposed to stress (D'hooge et al., 2006; Lu and Wang, 2008). Consequently, volumes are not necessarily conserved at a local level. Furthermore, the mechanical properties of the myocardium have been shown to be anisotropic —i.e. dependent on the local fiber directions — and nonlinear (Sachse, 2004)

Pericardium

The pericardium is the fibrous fluid-filled sac that encloses and restrains the heart. The pericardium consists of two layers separated by the serous cavity. Normally, the serous cavity contains up to 30 ml of fluid (Hess and Carroll, 2008), which reduces the friction between the moving heart and its surroundings. The inner layer — called epicardium or visceral pericardium — is firmly attached to cardiac wall. The outer layer — the parietal pericardium — is strongly attached to the sternum, the great vessels and the diaphragm, and keeps the twisting, contracting, and squeezing heart in place in the thorax. The pericardium stands out clearly in echocardiograms, especially in the regions where the ultrasound beams are close to perpendicular to the smooth surface.

Endocardium

Endocardium is the thin layer that covers the inner surfaces of the heart – including the cardiac valves – similar to the endothelial cells that line blood vessels.

The cardiac skeleton

The fibrous connective tissue that separates the atria from the ventricles is called the cardiac skeleton. This structure acts as an electric insulator between the atrias and the ventricles, and supports the cardiac valves and the myocardium. The cardiac skeleton can be subdivided into the mitral, tricuspidal, aortic and pulmonary valve rings, the fibrous trigones (small triangular zones of connective tissue between the valve rings), and the membranous basal part of the intraventricular septum. The high density of the cardiac skeleton compared to the surrounding tissue results in high backscatter intensities in echocardiograms, as seen in the images in Tables 2.1 and 2.2.

The mitral valve and the chordae tendineae

The mitral (bicuspid) valve prevents backward flow from the left ventricle to the atrium during systole. The mitral valve consists of an anterior and a posterior leaflet, where the anterior leaflet is the wider but occupies less of the mitral annulus. The leaflets are normally thin, smooth, and translucent, consisting of soft connective tissue and a fibrous skeleton. The mitral leaflets are anchored by numerous thin cords — chordae tendineae — to the tips of the papillary muscles, in order to prevent the valves to be everted into the atrium by the left ventricular systolic pressure. The area of the mitral valve orifice is normally about $4 - 6\ cm^2$.

The mitral valve is seen clearly in most echocardiograms, and the cords are observable in subjects with good image quality.

Aortic valve

The aortic valve prevents backward flow from the aorta to the left ventricle during diastole. The circular aortic valve is usually just above 2 cm in diameter and consists of three nearly equal-sized cusps: the right, left and posterior semilunar cusps. The

histological structure is the same as in the mitral valve, a collagenous core covered by fibroelastic tissue and lined with an endothelial layer.

Blood

The cavities of the heart are completely filled with blood. Blood can — like other liquids — be considered incompressible as an almost infinitesimal increase in the blood density produces a substantial rise in pressure. Blood consists of approximately equal volumes of *plasma* and *cells*. Plasma consist of about 90 percent water, 7 percent protein and 2 percent other organic and inorganic substances. The cellular volume consist mainly of red blood cells (erythrocytes) and less than one percent of white blood cells and platelets (Fung, 1981). As there is little local variation of cell concentration in blood, the compressibility and density is almost homogenous within the blood pool. This makes the blood appear as black regions in the echocardiograms.

2.2 Ultrasound imaging

2.2.1 Ultrasonic pulse-echo imaging

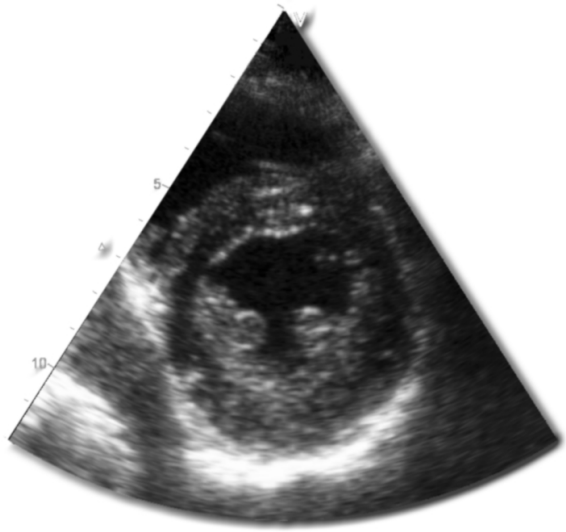

Figure 2.5: Echocardiogram showing a short-axis view of the left ventricle.

Ultrasound pulse-echo imaging utilizes that some of the energy in a propagating ultrasound wave is reflected or scattered due to local variations in the density ρ and compressibility κ, giving rise to redirected waves that can be detected and displayed as an image. The ultrasound waves are usually generated by an array (or matrix)

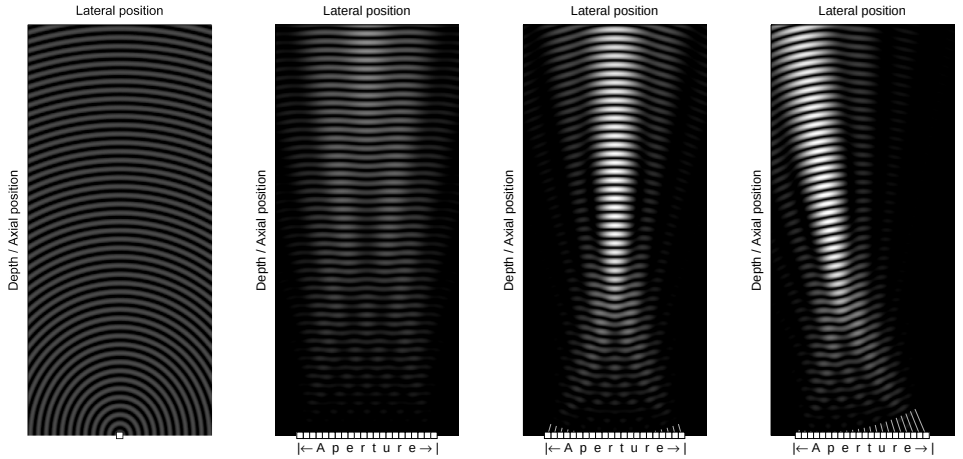

(a) Single transducer element (b) Unfocused transducer (c) Focused transducer (d) Beam steering

Figure 2.6: Beamforming.

of ceramic piezo-electric transducer elements. When an alternating voltage signal is applied to a such an element, it will start to vibrate and thereby give rise to a compression wave. Conversely, when a piezo-electric element is exposed to a compression wave, it will generate voltage signal. In order to achieve axial resolution, short ultrasound pulses are transmitted. When the propagation medium is soft tissue, the propagation velocity c can be assumed to be fairly constant (i.e. $\approx 1540\ m/s$), so that the time interval between the pulse is emitted and a reflected signal is picked up by the transducer is proportional to the depth of the reflector. The axial detail resolution — i.e. the minimum spacing Δr of distinguishable infinitesimal point scatterers — is therefore dependent on the pulse length τ of the transmitted signal, which is inverse proportional to the transducer bandwidth B:

$$\Delta r = {}^{c\tau}/_{2} = {}^{c}/_{2B} \tag{2.1}$$

The transmitted pulse always contains a few oscillations due to physical limitations in the pulse generation (e.g ring-down effects). High transmit frequency increases the maximal bandwidth and would generally result in better resolution. However, the attenuation of the ultrasound signal increases considerably with frequency, and cardiac imaging is therefore normally limited to frequencies below 5 MHz to achieve sufficient penetration depth.

Lateral resolution is achieved by focusing the transducer array by manipulating the phase by applying delays in the emitted signal for each element, so that positive interference occur in one specified direction, while the signal is canceled out elsewhere (see Fig. 2.6). Together, all elements contributing to the signal constitute the active aperture D. The backscattered signal picked up by the transducer would mainly stem from scatterers within the main lobe of the beam, and the lateral resolution is thereby

determined by the width of the main lobe. It can be shown that the lateral beam profile of a rectangular aperture assumes a Fraunhofer diffraction pattern shaped as a *sinc* function (Goodman, 1996). Correspondingly, the to-way (transmit-receive) lateral beam profile become a $sinc^2$ function. The lateral resolution is commonly defined by the Rayleigh resolution criterion as the distance to the first minimum of this $sinc^2$ diffraction pattern, namely:

$$\Delta\Theta = \sin^{-1}\left(\frac{\lambda}{D}\right) \approx \frac{\lambda}{D} \tag{2.2}$$

where $\Delta\Theta$ is the lateral angular resolution and *lambda* is the wavelength. The last approximation is valid for small angles. The spatial resolution Δl at depths equal to the focal length F becomes thereby:

$$\Delta l = \Delta\Theta \; F = f_{/\#}\lambda \tag{2.3}$$

where the f-number $f_{/\#}$ denotes the focal ratio defined as $f_{/\sharp} = F/D$. In order to achieve a more homogenous lateral resolution, dynamic focusing and expanding aperture can be performed during receive, aiming to keep the f-number unchanged with depth. The amplitudes of the side lobes may be reduced by lowering the signal amplitude towards the edges of the aperture, at the expense of a wider main lobe. The 2D ultrasound image is constructed by putting together several beams that cover different parts of the object under investigation. Three different array-element configurations are represented in this PhD work: The linear sequential array, the linear (1.5D) phased array, and the 2D array. The linear sequential array has typically up to 512 transducer elements resulting in a large transducer footprint. The image is formed by transmitting pulses perpendicular to the face of the transducer from a sub-aperture. The transmitting sub-aperture is sequentially shifted along transducer aperture, resulting in a rectangular field of view, where the width equals the transducer footprint. In cardiac imaging, the transducer footprint is limited by the spacing between the ribs. In order to achieve a wider field of view, the beams are steered in different azimuthal directions resulting in the sector-shaped view seen in e.g. Fig. 2.5. In the so called 1.5D array, the aperture consist of a 2D array of elements — but with a very limited number of elements in the elevational direction — allowing improved elevational focusing but no elevational steering. A 2D phased array consists of a large number of elements in both directions, which makes it possible to steer the beam in elevation as well as in azimuth within a pyramidal field of view.

Assuming linear wave propagation and neglecting multiple scattering, the imaging process may be regarded as a linear filter applied to an object function, which describes the real variations of density and compressibility. This is seen in Fig. 2.7(a), where filtering of the object function to the left results in the ultrasound image to the right. The filter is the system's point spread function (PSF). The PSF is defined as the spatial impulse response of the system, i.e. the output of the system in the case of a single ideal point scatterer. The bright regions in the ultrasound image – in the areas where the structures are close to perpendicular to the beams – have also become narrower although this effect is cushioned by the lateral blurring.

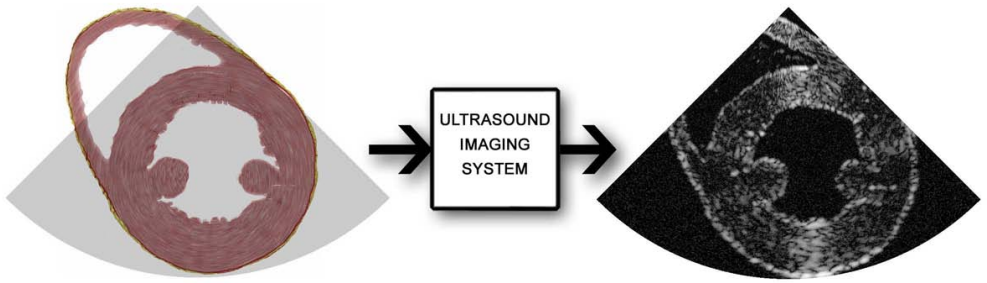

(a) Spatial domain

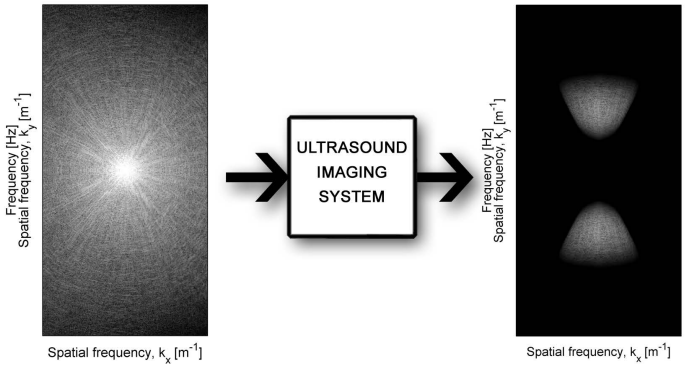

(b) Frequency domain

Figure 2.7: Illustration of the ultrasound imaging process of a short axis slice of the heart.

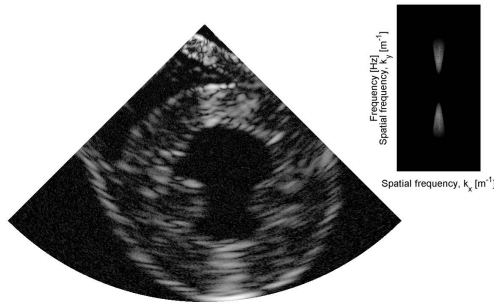

Figure 2.8: Simulated ultrasound image of the same short-axis model as in Fig. 2.7 using an imaging system with a higher f-number.

The echogenic properties of an object is given by the acoustic impedance Z, which is a function of the density ρ and the compressibility κ :

$$Z = \rho c = \sqrt{\frac{\rho}{\kappa}} \tag{2.4}$$

Due to the directivity of the compression waves and the finite aperture size, the ultrasound imaging process provides an orientation-dependent view of the acoustic properties of the object. In other words, the image consist only of the scatterer signal that is reflected back to the aperture. The lateral frequency content of the image is therefore limited by the critical angles $\pm\theta_c$ in elevation and azimuth, defined by:

$$\theta_c = tan^{-1}\left(\frac{1}{2f_{/\#}}\right) \tag{2.5}$$

The effect of this directional limitation is apparent in Fig. 2.7(a). In the object function to the left, the acoustic impedance of the object is correlated circumferentially inside the myocardium to resemble circumferentially orientated muscle fibers. The resulting ultrasound image shows increased backscattering where the normal to these circular layers are within the critical angles. If we look at the spatial frequency content of the object and the images (Fig. 2.7(b)), i.e. their 2D Fourier transforms, the limitations of the imaging process become evident. Such a spatial frequency description of an imaging system may be referred to as the *k-space*. Only parts of the spatial frequency content of the object function is apparent in the ultrasound image. In the axial direction the imaging process is bandlimited due to the non-infinitesimal pulse length. In the lateral direction the imaging process is a low-pass function limited by the critical angles. (A schematic drawing of the spatial frequency response is shown in Fig. D.2 in the last paper.) Figure 2.8 shows the effect of using a smaller aperture and thus, a higher f-number. The region of the support in the frequency domain has become narrower laterally, resulting in worse lateral resolution in the ultrasound image.

To sum up, the appearance of the ultrasound image is not just a function of the acoustic impedance of the investigated tissue, but is highly dependent on the imaging system. Particularly, the frequency content of the transmitted pulse and the scanning geometry given by the f-number determine how much of the spatial frequency content of the tissue could be observed in the resulting ultrasound image.

2.2.2 Tissue Doppler imaging

Due to the Doppler effect, tissue motion causes a frequency change in the returned echoes, known as the Doppler shift f_d, that is proportional to the tissue velocity parallel to the beam $v_{\shortparallel}$:

$$f_{obs} = f_0 + f_d = f_0\left(1 - \frac{2v_{\shortparallel}}{c}\right) \tag{2.6}$$

where f_{obs} is the observed echo frequency, f_0 is the transmit frequency, and c is the sound velocity.

According to this equation, it should be possible to calculate the tissue velocity from one single ultrasound pulse by measuring the Doppler shift. However, a very long observation time is needed to achieve a frequency estimate with resolution high enough to quantify the small Doppler shifts associated with tissue motion. This is incompatible with the demand for axial resolution. Moreover, the frequency is also changed during propagation due to for example frequency dependent attenuation. Consequently, it is preferable to calculate the tissue velocities from the observed phase shift $\Delta\phi$ from a packet of pulse transmissions (Torp, 2000):

$$\widetilde{v}_{\shortparallel} = \frac{c\widetilde{\Delta\phi}}{4\pi f_0 T} \tag{2.7}$$

where T is the pulse repetition time. The phase shift can be found from the autocorrelation estimator with lag 1 ($\widetilde{R}_1$):

$$\widetilde{\Delta\phi} = args\left(\widetilde{R}_1\right) = tan^{-1}\left(\frac{Im\{\widetilde{R}_1\}}{Re\{\widetilde{R}_1\}}\right) \tag{2.8}$$

$$\widetilde{R}_1 = \frac{1}{N-1}\sum_{k=1}^{N-1} z(k+1)z(k)^* \tag{2.9}$$

where N is the number of pulses in each packet, and $z(k)$ is the complex time-discrete signal sample at time kT. Consequently, $z(k)$ and $z(k+1)$ are signal samples, corresponding to the same depth, from two consecutive pulses within the same packet. The phase angles are resolved in the interval $[-\pi, \pi]$ only, and phase angles outside these limits would therefore be folded into the interval. This effect is called velocity aliasing. The maximal absolute velocity is named the Nyquist velocity and is given by:

$$v_{Nyq} = \frac{c}{4f_0 T} \tag{2.10}$$

The two-dimensional tissue Doppler image consists usually of fewer (and wider) ultrasound beams than a B-mode image with the same field of view. The estimated tissue velocities are usually shown as a color overlay on top of the B-mode images acquired between the Doppler images, in order to make it easier to identify anatomical structures. Most commonly, the velocities towards the probe are shown as red colors, while velocities away from the probe are shown as blue.

2.2.3 Full volume imaging

Although acquisition of three-dimensional ultrasound has been possible by mechanized or free-hand translation or rotation of 1D (or 1.5D) arrays or by sparse 2D arrays, the complex acquisition, limited commercial availability, or poor image quality has prevented its use in daily clinical practice. The first commercial transducer with a fully sampled 2D array was the *X4 xMatrix* transducer introduced by Philips in 2002 as a part of the *SONOS 7500* scanner (Savord and Solomon, 2003; Salgo, 2007). Since then,

other large providers of ultrasound systems have released ultrasound systems with real-time 3D capabilities, bringing promises of a new spring for 3D echocardiography.

Construction of 2D array transducers is complicated by the large number of elements involved and the high impedance due to the tiny elements. While 64-128 elements are sufficient for an 1D array, a fully sampled 2D array typically consists of 2000–3000 elements. Using a traditional phased array design, this would result in an interconnect cable with approximately ten times the normal diameter, which is naturally not acceptable. This is solved by performing parts of the beam forming in integrated circuits within the transducer housing. In this way, the base system can treat the 2D array as a simpler array with just a fraction of the number of elements.

In echocardiography, high temporal resolution is needed to evaluate the structural changes within a cardiac cycle, which usually lasts less than one second. At the same time, it is preferable to maintain a field of view that is wide enough to cover the entire left ventricle. As the pulse repetition time is determined by the time needed for a pulse to propagate the entire depth of the field of view and back again, the speed of sound in soft tissue ($c \approx 1540\ m/s$) limits the achievable frame rate. Performing 3D cardiac imaging using a simple pulse-echo approach and a wide field of view would consequently result in volume rates about 1 Hz, which is undoubtedly far too low. Increased temporal resolution could be achieved by reducing the number of transmit beams at the cost of poorer lateral resolution. However, a preferred solution is to increase the volume rate by using multi-line acquisition (MLA), i.e. several receive beams per transmit beam (Shattuck et al., 1984). In contrast to 1D arrays, a 2D array allows MLA in two dimensions, which makes it even more beneficial. However, the increased volume rate comes at a cost. The use of MLA requires a wider beam width to fit the receive beams, and thereby leads to poorer image quality. Furthermore, the misalignment of the transmit and receive beams inherent in the MLA approach results in block artifacts corresponding to the MLA groups in the ultrasound data. Wavefront aberrations — i.e. distortions of the beams due to inhomogeneities in the body wall, especially in fat – make it difficult to compensate for this artifact in real patients (Bjåstad et al., 2007). The MLA artifact becomes worse when the angle between the transmit and receive beams increases, which also places a limitation on the feasible number of parallel receive beams.

By reducing the number of beams in a MLA , real-time full volume imaging could be performed (Frey and Chiao, 2008). However, in order to achieve a large enough field of view with better lateral resolution, MLA is often combined with ECG-gated capture. Using gated capture, the imaging volume is built up over several (usually four) heart beats (Brekke et al., 2007). A subvolume is acquired in each cardiac cycle, as seen in Fig. 2.9. (In contrast to the figure, the central parts of the volume are normally acquired first, e.g. in the order 2–3–1–4.) For each subvolume, the previously acquired cardiac cycle is replayed until a new update is available. The alignment of the subvolumes could therefore be corrupted by variations in cardiac rhythm, breathing, or probe motion.

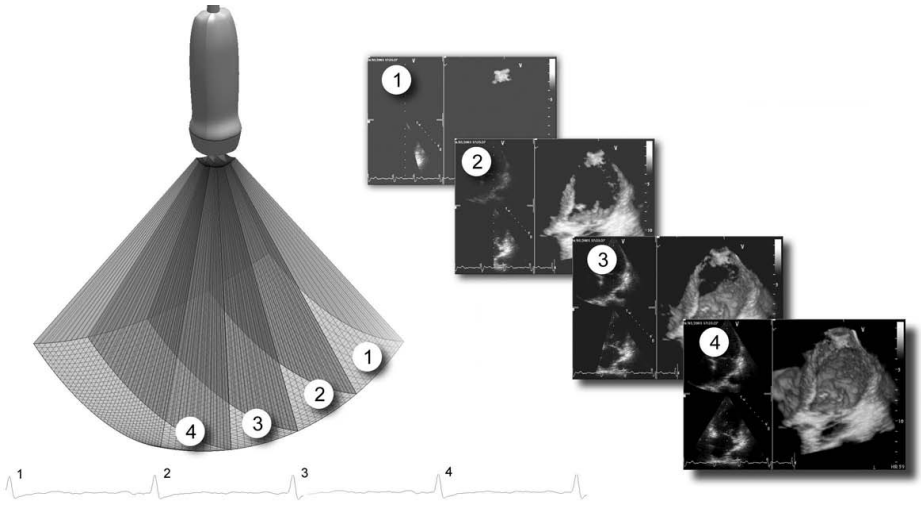

Figure 2.9: Gated acquisition.

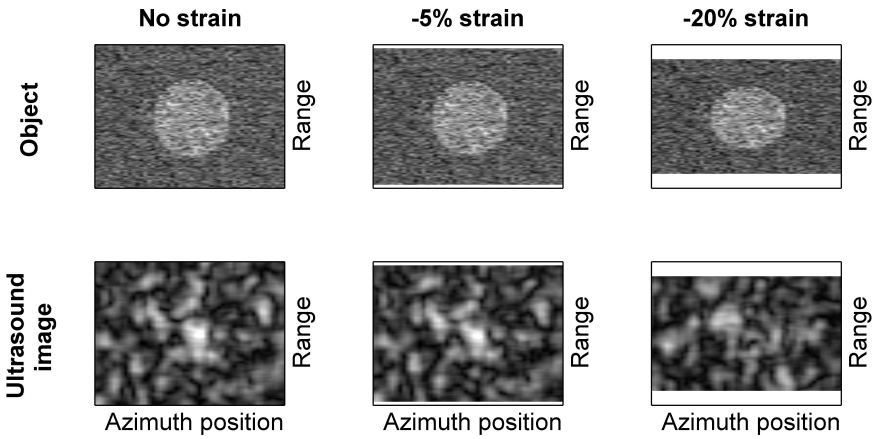

Figure 2.10: Illustration of the decorrelation of the speckle pattern in ultrasound images due to tissue deformation.

2.3 Tracking methodology

2.3.1 Speckle

Speckle is the characteristic texture seen in ultrasound images as spatial fluctuations in the intensity. Speckle is a consequence of the interference between waves with different

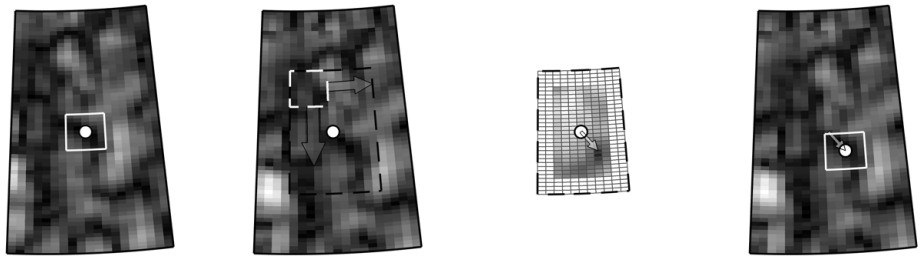

(a) A tracking kernel (white square) is defined around the track point in an initial frame *k*.

(b) The tracking kernel is compared with target regions of the same size in frame *k+1* within a limited search region (dashed black line) using a block similarity measure.

(c) The inter-frame displacement is found from the optimum of the similarity function.

(d) The position of the track point is updated according to the estimated displacement and a new tracking kernel is defined.

Figure 2.11: Speckle tracking. Determination of the inter-frame displacement of a track point using block matching

phases, and can also be observed in electromagnetic waves, for example when a laser beam is scattered of a rough surface. In pulse-echo ultrasound, the numerous sub resolution scatterers give rise to new waves. The waves have different phases, which creates seemingly random amplitude variations in the resultant signal.

Although the speckle pattern does not directly reflect real structures, it is deterministic in the sense that the speckle pattern remains the same (for fixed transmit/receive frequencies) as long as the distance between the scatterers is unchanged in the beam direction. This means that the speckle pattern is preserved under tissue translation (assuming unchanged insonification angle). If the distance between the scatterers changes due to deformation or rotation, the axial phase contribution from each point scatterer is altered, resulting in a different diffraction pattern in the received signal. Therefore, as long as the inter-frame deformation (or rotation) of the tissue is small, the speckle pattern is expected to degrade gradually. Figure 2.10 illustrates that the speckle pattern still is recognizable after a small axial compression, but is completely changed by a larger compression.

2.3.2 Speckle tracking

Speckle tracking is a block-matching method for tracking motion in ultrasound images. It is based on the assumption that the local speckle patterns is sufficiently preserved between frames to allow tracking of the local tissue motion from displacements of local intensity patterns.

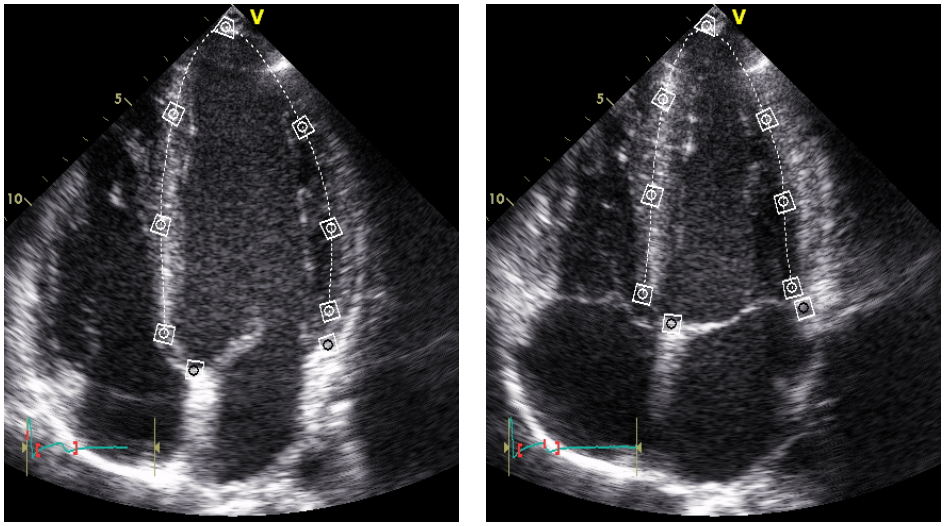

(a) Initial configuration in end-diastole. (b) Tracked positions in end-systole.

Figure 2.12: Speckle tracking of nine left ventricular points in an apical 4-chamber view. The regions of interest (ROIs) are shown as white quadrilaterals (which correspond to rectangular ROIs in beam-space).

Usually, several regions of interest (ROIs) are place within the structures to track. Figure 2.11 shows how the speckle pattern within such an ROI is tracked from one frame to another. The ROI in a frame k (Fig. 2.11(a))— the tracking kernel — is compared with all possible target ROIs of the same size in frame $k+1$ within a defined search region (Fig. 2.11(b)). The search region is usually defined using *a priori* knowledge of the maximum expected inter-frame displacement. The comparison is performed using a similarity measure, and results in a spatial similarity map (Fig. 2.11(c)). The displacement is found as the optimum of this similarity map, corresponding to the best match. A new displaced ROI is then defined in frame $k+1$ (Fig. 2.11(d)) that could be used to track the speckle motion between frame $k+1$ and frame $k+2$. Figure 2.12 shows an example of speckle tracking in a 4-chamber view using seven ROIs placed within the left ventricular myocardium and two ROIs on the cardiac skeleton.

Speckle tracking can be applied to the raw radio frequency (RF) data, the envelope detected beam-space data, or the displayed scan-converted data. Using RF-data, better axial resolution of displacements could be achieved, but due to the strong cyclic component the matching function becomes less smooth, and this might increase the possibility of false matches. For the same reason, RF data are associated with more decorrelation than envelope data for high strain values (Alam and Ophir, 1997). Furthermore, tracking in RF data generally requires more computation time because of the higher sampling rates and increases the difference between axial and

lateral resolution. For these reasons, RF tracking is mostly used in applications associated with small deformation (and preferably in the axial direction), as for example elastography (Wilson et al., 2000).

In the description above all possible blocks in the search region were evaluated. In order to save computation time, a search algorithm could be applied that tries to find the optimum based on evaluation of a few blocks. Such methods are unfortunately not guaranteed to end up in the global optimum of the search area. Hierarchical (or multi-scale) block matching is another approach (Basarab et al., 2007), where the displacement estimates are refined by performing the matching at different resolution scales in order to make the tracking estimates more robust or to reduce computation time.

The coarse resolution in the beam directions introduces quantification error in the lateral tracking. This problem can be reduced by introducing sub-pixel methods to improve the lateral resolution. Relevant sub-pixel methods could be to calculate the displacement vector as an average of tracked neighboring points, interpolate the similarity map across the search area, or interpolate beam space data in the two lateral directions.

2.3.3 Similarity measures in block matching

The three similarity measures most commonly used in speckle tracking are the normalized cross-correlation (the cross-correlation coefficient), the sum of absolute differences (SAD), and the sum of squared differences (SSD). The equations of these are found below. The normalized cross-correlation (NC) is generally expected to yield optimal estimates (Viola and Walker, 2003). However, SSD and SAD have been shown to give comparable 2D tracking results with reduced computational complexity (Bohs and Trahey, 1991; Langeland et al., 2003).

Other measures includes polarity-coincidence correlation (one bit correlation), hybrid-sign correlation, and the Meyr-Spies method. These have been shown to have inferior performance for 1D tracking in ultrasound RF data (Viola and Walker, 2003) and are rarely used. In addition, the two first are dependent on the sign of the signals and are therefore not well suited for tracking envelope data. Invariant moments (Ding et al., 2001) provides a means of comparing data templates irrespective of their rotational differences. However, due to the rotational dependence of the speckle pattern (Subsection 2.3.1) the benefits of this method are limited for ultrasound data.

Normalized cross-correlation. If C_k and C_{k+1} is the image data in frame k and $k+1$, respectively, and (x_0, y_0) is the center of the ROI of size $(2m+1) \times (2n+1)$ in frame k, then the normalized cross-correlation coefficient r_{nc} for a given displacement

$[dx, dy]$ is given by:

$$r_{nc}(dx,dy) = \frac{\sum_{j=-n}^{n}\sum_{i=-m}^{m} C_k(x_0+i, y_0+j)C_{k+1}(x_0+dx+i, y_0+dy+j)}{\sqrt{\sum_{j=-n}^{n}\sum_{i=-m}^{m} C_k^2(x_0+i, y_0+j)}\sqrt{\sum_{j=-n}^{n}\sum_{i=-m}^{m} C_{k+1}1^2(x_0+i, y_0+j)}} \tag{2.11}$$

The denominator is a normalization factor. When the kernel and the target regions are normalized so that they have zero means, i.e.:

$$\sum_{j=-n}^{n}\sum_{i=-m}^{m} \frac{C_k(x_0+i, y_0+j)}{(2m+1)(2n+1)} = \sum_{j=-n}^{n}\sum_{i=-m}^{m} \frac{C_{k+1}(x_0+i, y_0+j)}{(2m+1)(2n+1)} = 0 \tag{2.12}$$

the correlation coefficient r_{nc} will be a value in the interval $[-1, 1]$. If $r_{nc} = 1$, the intensity variations in the kernel and the target regions are completely correlated and there is a perfect linear relationship between the two regions. Lower values of r_{nc} signify a weaker linear relation between the regions, and $r_{nc} = 0$ means that the intensity patterns in the two regions are completely independent. Negative values indicate inverse dependence of the regions, and $r_{nc} = -1$ means that there is a negative linear relationship between the regions.

Sum of absolute differences. Using the same notation as in eqn 2.11, the similarity measure r_{SAD} is defined by:

$$r_{SAD}(dx,dy) = \sum_{j=-n}^{n}\sum_{i=-m}^{m} |C_k(x_0+i, y_0+j) - C_{k+1}(x_0+dx+i, y_0+dy+j)| \tag{2.13}$$

Consequently, $r_{SAD} = 0$ means that the kernel and target regions are equal. The value of r_{SAD} is restricted to the interval $[0, (2m+1)(2n+1)(C_{max} - C_{min})]$, where C_{max} denotes the maximal absolute pixel value. (The upper limit corresponds to a completely black kernel region and a white target region, or vice versa.)

Sum of squared differences. The similarity measure r_{SSD} is quite similar to the sum of absolute differences in eqn 2.13, but weighs larger deviations in intensity values more than smaller deviations:

$$r_{SSD}(dx,dy) = \sum_{j=-n}^{n}\sum_{i=-m}^{m} \left(C_k(x_0+i, y_0+j) - C_{k+1}(x_0+dx+i, y_0+dy+j)\right)^2 \tag{2.14}$$

The value of r_{SSD} lies within the interval $[0, (2m+1)(2n+1)(C_{max} - C_{min})^2]$.

Mutual information

Mutual information is a measure based on correspondence of the number of pixels at each intensity level between the kernel and the target region, and not on the intensity values themselves (Maes et al., 1997; Pluim et al., 2003). It assumes that there exists an one-to-one correspondence between the intensity levels in the two images but not necessarily a linear relationship as assumed by NC, SAD and SSD. This property makes mutual information well suited for intermodality registration, and it has become a popular similarity measure in e.g. registration of MRI and CT images. The recent deployment of 3D ultrasound systems has also led to an increased interest in mutual information within the field of echocardiography (Shekhar and Zagrodsky, 2002; Elen et al., 2007). Unfortunately, the speckle pattern in ultrasound data might violate the assumption of one-to-one correspondence. Therefore, ultrasound data are usually filtered in order to reduce the negative impact of the speckle pattern.

2.3.4 Optical flow

The block-matching approach is often considered to be a subgroup of optical flow (Barron et al., 1994; Angelini and Gerard, 2006). The common goal of the optical flow methods is to quantify or visualize motion based on spatio-temporal data sets. Often the entire velocity field in each frame is calculated, but the motion estimation can also be done by tracking the motion of a set of ROIs, like in the speckle tracking approach. Besides block matching, the optical flow methods can be divided into differential and frequency techniques (Boukerroui et al., 2003). The differential techniques estimate the velocity field from derivatives of the intensity values. They are often limited to sub-pixel (or sub-voxel) inter-frame displacement and as they involve numerical differentiation, they might be sensitive to noise. The frequency techniques are based on the observation that motion corresponds to orientation in the spatio-temporal frequency domain, so that the velocity could be estimated from the energy distribution in the spatio-temporal Fourier transform. In the differential and frequency techniques, the calculation of the velocity fields is preferably based on a number of frames with little temporal change in velocities. The velocity estimates in block matching, on the other hand, is usually based on only two frames. A thorough review of the different optical flow techniques is found in Barron et al. (1994).

2.4 Left ventricular rotation and strain

2.4.1 Rotation, twist and torsion

In three dimensions, rotation is the change in angular position relative to an axis of rotation. Figure 2.13 shows how the motion of a material point p from time k to time $k+1$, results in a rotation θ relative to the rotation axis $\vec{k}$. Any motion radially away from $\vec{k}$ or parallel to $\vec{k}$ does not contribute to the measured rotation. If the axis of rotation is aligned with the z-axis, the angle (θ_0) of a point, relative to the x-axis,

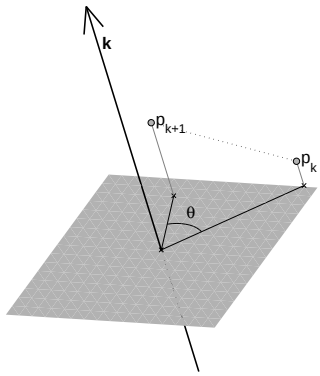

Figure 2.13: Rotation angle (θ) around an arbitrary axis of rotation ($\vec{k}$).

could be determined by its x- and y-components:

$$\cos\theta_0 = \frac{x}{\sqrt{x^2+y^2}} \;\wedge\; \sin\theta_0 = \frac{y}{\sqrt{x^2+y^2}} \tag{2.15}$$

The angle θ_0 in the range $(\pi, \pi]$ could be found by using the four quadrant inverse tangent function:

$$\theta_0 = \text{atan2}(y,x) \equiv \begin{cases} -atan2(-y,x) & y < 0; \\ \pi - arctan(-y/x) & y \geq 0, x < 0; \\ arctan(y/x) & y \geq 0, x > 0; \\ \pi/2 & y > 0, x = 0; \\ 0, & y = 0, x = 0; \end{cases} \tag{2.16}$$

The rotation θ in Fig. 2.13, with respect to the material position in frame k, could thereby be calculated by:

$$\theta = \theta_{0,k+1} - \theta_{0,k}. \tag{2.17}$$

The possible wrapping from positive to negative angles, and vice versa, could in most cases easily be detected and accounted for.

The angular velocity ω is the first derivative of angular displacement, which is related to the tangential velocity $v_{\shortparallel}$ at distance r from the rotation center:

$$\omega = \frac{d\theta}{dt} = \frac{v_{\shortparallel}}{r} \tag{2.18}$$

This relation is important for the calculation of rotation from tissue Doppler velocities in Paper B.

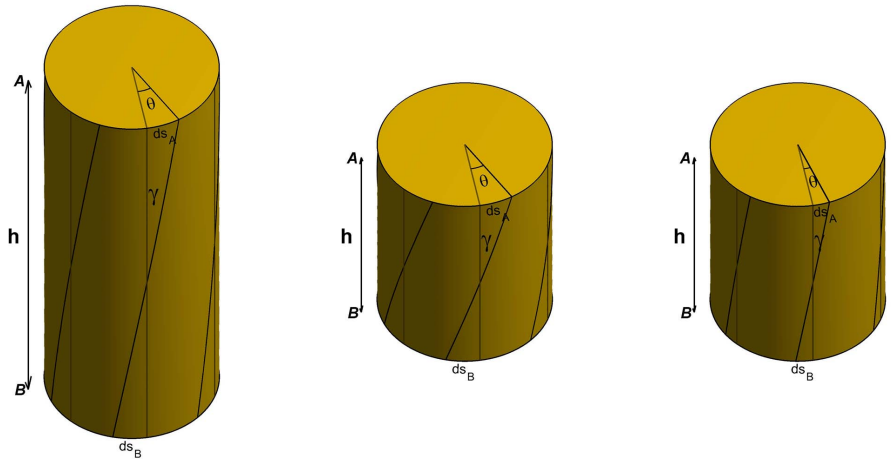

(a) Circular bar twisted relative to a reference configuration (dashed lines). $Height:\ h\ =\ 1.00\ cm$; $Rotation:\ \theta\ =\ 22.5°$; $Twist:\ \Delta\theta_{AB}\ =\ 45°$; $Torsion:\ \Theta\ =\ 45°/cm$.

(b) Short circular bar with the same twist angle as in (a). $Height:\ h\ = 0.50cm$; $Rotation:\ \theta\ =\ 22.5°$; $Twist:\ \Delta\theta_{AB}\ =\ 45°$; $Torsion:\ \Theta\ =\ 90°/cm$.

(c) Short circular bar with the same torsion as in (a). $Height:\ h\ = 0.50cm$; $Rotation:\ \theta\ =\ 11.25°$; $Twist:\ \Delta\theta_{AB}\ =\ 22.5°$; $Torsion:\ \Theta\ =\ 45°/cm$.

Figure 2.14: Illustration of rotation, twist and torsion.

In 2D geometries, counter-clockwise rotations are usually given positive signs. In 3D, clockwise and counterclockwise directions have to be defined relative to some reference in order to be unambiguous. In the papers in this thesis, positive numbers represents counter-clockwise rotation when viewed from the base, but not when viewed from the apex. As an apical point of view is most common, both in imaging and in open-chest surgery, it might be generally more convenient to let positive numbers represents counter-clockwise rotation when viewed from the apex. This has also become the most widespread convention.

Angle of twist (or *twist angle*) may be defined as the rotational difference between two material points that initially have the same angle with respect to an axis of rotation. From the field of solid mechanics, a typical example is the twisting of a circular bar under action of external torques in both ends. The angle of twist is given by the resultant rotation due to the torque measured in one end minus the rotation measured at the other end. This is illustrated in Fig. 2.14, where the rotation in the upper end (A) and the lower end (B) results in an angle of twist:

$$\Delta\theta_{AB} = \theta_A - \theta_B \tag{2.19}$$

that is independent of the height (h) of the cylinder. It should be noted that the papers in this thesis deviates somewhat from these definitions: In Paper B the angle

of twist is calculated from two short-axis levels, where the observed material points might change during rotation. Furthermore, in Paper A, the same measure is referred to as torsion, in order to be in agreement with previous studies.

In engineering, torsion (Θ) is usually calculated as the angle of twist per unit height:

$$\Theta = \frac{\Delta\theta_{AB}}{h} \tag{2.20}$$

For the cylinder in Fig. 2.14, the shear angle γ is related to torsion by:

$$\gamma \approx \frac{ds_A - ds_B}{h} \approx \frac{(\theta_A - \theta_B)r}{h} = \Theta r \tag{2.21}$$

where ds_A and ds_B is the circumferential displacements at the ends in distance r from the rotation axis.

2.4.2 Strain and deformation

One-dimensional strain

The change of length in a line segment may be quantified using the one-dimensional Lagrangian strain ϵ:

$$\epsilon(t) = \frac{L(t) - L_0}{L_0} = \frac{L(t)}{L_0} - 1 \tag{2.22}$$

where $L(t)$ is the length of the line segment at time t and L_0 is a reference length — usually the length of the segment before deformation. Strain is a dimensionless quantity – often expressed as a percentage – where positive values denotes lengthening and negative denotes shortening. Lagrangian strain is also called Cauchy strain or engineering strain.

Strain rate is the time derivative of strain:

$$\dot{\epsilon}(t) = \frac{\dot{L}(t)}{L_0} \tag{2.23}$$

Strain rate has the unit s^{-1}. It is also possible to define strain rate with respect to the instantaneous length $L(t)$ rather than a reference length:

$$\dot{\epsilon}_N(t) \equiv \frac{\dot{L}(t)}{L(t)} = \frac{\frac{dL(t)}{dt}}{L(t)} \tag{2.24}$$

This is a convenient measure in for example color Doppler imaging as the strain rate could be determined in each frame from the velocities in the end points:

$$\dot{\epsilon}_N(t) = \frac{v_2 - v_1}{L} \tag{2.25}$$

Integration of eqn 2.24 results in another strain measure $\epsilon_N(t)$, which is referred to as logarithmic, true, natural, or Eulerian strain:

$$\epsilon_N(t) = \int_{t_0}^{t} \frac{\frac{dL(t)}{dt}}{L(t)} dt = \int_{L_0}^{L} \frac{1}{L(t)} dL = \ln\left(L(t)\right) - \ln\left(L_0\right) = \ln\left(\frac{L(t)}{L_0}\right) \tag{2.26}$$

where the change of integration variable was done using the substitution rule. This yields the relation between Eulerian and Lagrangian strain:

$$\epsilon_N = \ln(\epsilon + 1) \tag{2.27}$$

$$\epsilon = e^{\epsilon_N} - 1 \tag{2.28}$$

Eqns 2.22, 2.26, and 2.28 give the relation between Eulerian and Lagrangian strain rate:

$$\dot{\epsilon}_N = \frac{\dot{\epsilon}}{1+\epsilon} \tag{2.29}$$

$$\dot{\epsilon} = \dot{\epsilon}_N \; e^{\epsilon_N} \tag{2.30}$$

Consequently, the difference between the Eulerian and the Lagrangian strain measures increases with strain. The (somewhat misleading) use of the terms *Lagrangian* and *Eulerian* strain and strain rate, reflects that the first often is most convenient in a Lagrangian reference frame which follows the motion of the material points, while the latter often is used in an Eulerian reference frame, in which the motion is evaluated at fixed locations in space.

Strain in three dimensions

Due to the approximately ellipsoidal shape of the left ventricle, it is often more convenient to describe the deformation using local coordinates instead of a global Cartesian coordinate system. The local coordinates are defined by a radial, transmural axis ($\vec{k}_r$), a circumferential axis ($\vec{k}_\theta$), and a longitudinal axis ($\vec{k}_\phi$). The axis forms ideally a rectangular coordinate frame locally, with $\vec{k}_r$ perpendicular to the wall, $\vec{k}_\theta$ in parallel to the wall in the anti-clockwise direction viewed from the base, and $\vec{k}_\phi$ parallel to the wall in the base-to-apex direction (Fig. 2.15). For a symmetric ellipsoidal left ventricle these local coordinate systems would coincide with the axes of a global prolate spheroidal coordinate system.

Assuming a small volume element within the wall, the deformation of this element may be described by a strain matrix containing 9 elements; 3 normal strains ϵ_i and 6 shear strains γ_{ij}:

$$\epsilon_{ij} = \begin{bmatrix} \epsilon_{11} & \epsilon_{12} & \epsilon_{13} \\ \epsilon_{21} & \epsilon_{22} & \epsilon_{23} \\ \epsilon_{31} & \epsilon_{32} & \epsilon_{33} \end{bmatrix} = \begin{bmatrix} \epsilon_1 & \frac{1}{2}\gamma_{12} & \frac{1}{2}\gamma_{13} \\ \frac{1}{2}\gamma_{21} & \epsilon_2 & \frac{1}{2}\gamma_{23} \\ \frac{1}{2}\gamma_{31} & \frac{1}{2}\gamma_{32} & \epsilon_3 \end{bmatrix} \tag{2.31}$$

where 1,2, and 3 denotes the first, second, and third coordinate in the given coordinate system. The elements in eqn 2.31 could be determined by calculating the finite strain tensor with respect to the given coordinates. The finite strain tensor is given by:

$$\epsilon_{ij} = \frac{1}{2}\left(\frac{\delta u_i}{\delta x_j} + \frac{\delta u_j}{\delta x_i} - \frac{\delta u_k}{\delta x_i}\frac{\delta u_k}{\delta x_j}\right) \tag{2.32}$$

where $\mathbf{u}(\mathbf{x}, t)$ is the displacement field. For small deformations, the non-linear or second-order terms of the finite strain tensor can be neglected resulting in the simpler

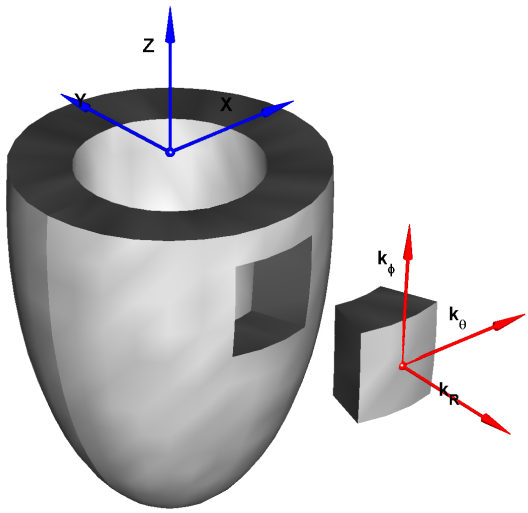

Figure 2.15: Left ventricular coordinate systems. (Based on an illustration in D'hooge et al. (2000).)

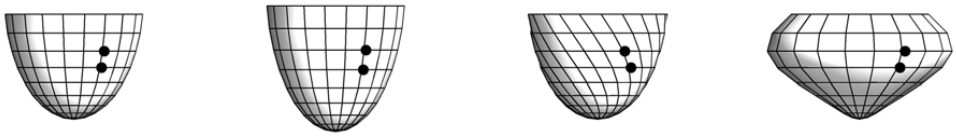

Figure 2.16: Longitudinal strain. Assuming the initial LV configuration in the leftmost illustration, the total longitudinal strain could be affected by LV lengthening, twist and shape changes.

infinitesimal strain tensor:

$$\epsilon_{ij} \approx \frac{1}{2}\left(\frac{\delta u_i}{\delta x_j} + \frac{\delta u_j}{\delta x_i}\right) = \frac{1}{2}\left(\nabla_j u_i + \nabla_i u_j\right) \tag{2.33}$$

The assumption of small deformation also implicates that there is little difference between the Eulerian and Lagrangian description. However, the LV undergoes large deformations during the cardiac cycle, so that the assumption of infinitesimal strains is generally inaccurate. In the local LV coordinates, ϵ_1 $(= \epsilon_r)$ would describe transmural strain (i.e. wall-thickening), ϵ_2 $(= \epsilon_\theta)$ circumferential strain, and ϵ_3 $(= \epsilon_\phi)$ longitudinal strain. The shear angle γ_{32} $(= \gamma_{\theta\phi})$ would be related to the LV torsion. (Assuming a cylindrical shape, $\gamma_{3,2}$ $(= \gamma_{\theta z})$ would be given by eqn 2.21.) The quantification of 3D strain in this thesis is based on a quadrilateral mesh of ROIs that initially are

(approximately) aligned in the circumferential and longitudinal directions. Thus, the initial mesh coincides locally with the $\vec{k}_\theta$ and the $\vec{k}_\phi$ directions. The mesh follows the material motion of the ROIs during the cardiac cycle, and circumferential strain ($\tilde{\epsilon}_\theta$) and longitudinal strain ($\tilde{\epsilon}_\phi$) are measured from the distances between neighboring ROIs using the definition of strain in eqn 2.22. In the case of no shear, the resulting strains would be the same as ϵ_θ and ϵ_ϕ, respectively. In the case of shear, the strain values derived from the mesh would additionally be dependent on the segment lengthening due to the shear, as illustrated (for longitudinal strain) in Fig. 2.16.

As the shear elements in the strain matrix do not alter the volume of the volume element, the change in volume is only dependent on the normal strains ϵ_1, ϵ_2, and ϵ_3. Considering an initially cubic volume element with edge length a, the change in volume

$$\Delta V = V - V_0 = a^3(1+\epsilon_1)(1+\epsilon_2)(1+\epsilon_3) - a^3 \tag{2.34}$$

If the volume is conserved during deformation (i.e. incompressibility of the medium) $\Delta V = 0$, which — using eqn 2.34 — gives a relation between the normal strains:

$$(1+\epsilon_1)(1+\epsilon_2)(1+\epsilon_3) = 1 \tag{2.35}$$

If we again assume small deformation, the second and third order terms may be neglected and eqn 2.35 could be simplified to:

$$\epsilon_1 + \epsilon_2 + \epsilon_3 \approx 0 \tag{2.36}$$

In either case the third normal strain element could be calculated from the two others. Unfortunately, calculation of the radial strain ($\tilde{\epsilon}_r$) based on the mesh-derived strain measures ($\tilde{\epsilon}_\phi$ and $\tilde{\epsilon}_\theta$) would not be exact due to the dependence on the shear strains.

2.5 Reference methods

In this section, information is given about the reference methods used in the papers. An absolute *"ground truth"* reference is seldom obtainable when it comes to methods for measuring structures and tissue motion inside living bodies. Most available reference methods suffer from limitations in accuracy or application.

2.5.1 Magnetic resonance imaging (MRI)

Magnetic Resonance Imaging (MRI) is an imaging technique that exploits the quantum mechanical properties of certain nuclei when exposed to a strong external magnetic field. These properties are related to the magnetic moment in these nuclei, due to their intrinsic nuclear spin. Hydrogen is such a nucleus, and is — due to the abundance of water molecules in human tissues — the most commonly utilized nucleus in medical MRI.

In a simplified view, these nuclei can be thought of as small magnets spinning around their own axes. In a magnetic field, the nuclei will become orientated parallel

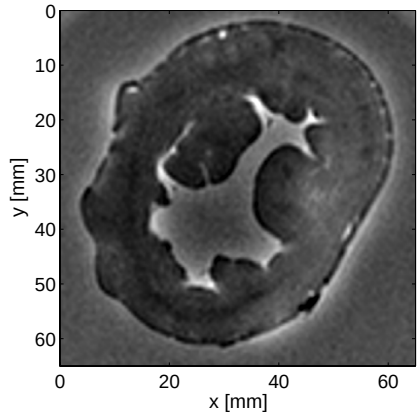

Figure 2.17: Magnetic resonance image (Achieva 3T, Philips Medical System, Best, Netherlands) of an excised porcine left ventricle embedded in poly vinyl alcohol cryogel (PVA-C).

or anti-parallel to the field. The parallel orientation is the lower energy state of the nuclei, and therefore marginally more of the nuclei are oriented this way. However, the axes of the spinning nuclei would themselves rotate around the direction of the magnetic field — a motion known as precession. The precession frequency is called the Larmor frequency, and is proportional to the strength of the magnetic field. The constant of proportionality is unique for each type of nucleus. The small net magnetic moment due to the overweight of nuclei with the parallel orientation is static and indistinguishable from the external magnetic field.

By transmitting electromagnetic pulses that oscillates at the Larmor frequency (which lies within the radio frequency range) perpendicular to the main field, energy is transferred to the spinning nuclei and the net angle of precession is changed and the precession is forced to be in phase. This net change in the magnetic moment results in an oscillating signal that could be picked up by a receiver coil. When the electromagnetic field is switched off, the magnetic momentum would return to its former state by a gradual change in the precession angle and a gradual de-phasing. The rate of these (nearly) independent effects could be measured as the T_1 and the T_2 relaxation times and would be different for different tissues. The values of T_1 and T_2 constitute the contrast information in the image.

In order to create an image, spatial resolution is needed. If the strength of the main field is modified by applying an additional magnetic gradient field, the Larmor frequency would become unique for each plane perpendicular to the field direction. In this way, it becomes possible to trigger nuclei close to a specified imaging plane by transmitting electromagnetic pulses with the Larmor frequency that corresponds to the field strength for the plane. A similar approach could be used in the two other directions to achieve spatial resolution within the imaging plane. However, in order to limit acquisition time, a static gradient field is only used in two directions, while

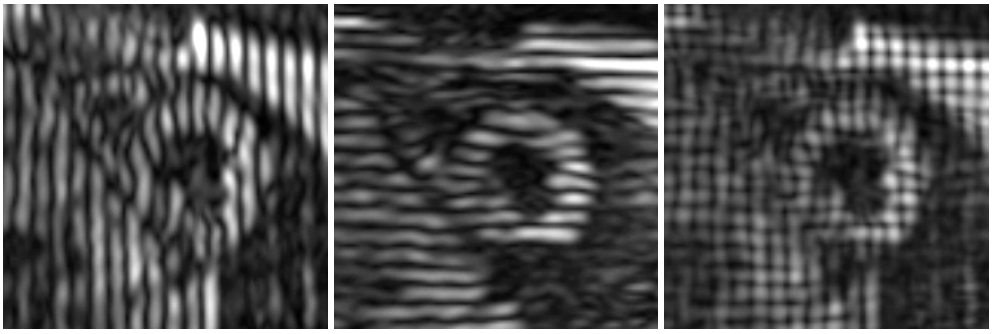

Figure 2.18: MRI tagging of a human heart (Intera 3T, Philips Medical System, Best, Netherlands). The two leftmost panels show MRI recordings with vertical and horizontal tag lines, respectively. The rightmost panel shows the tracking grid obtained by combining the vertical and horizontal tag lines.

the third field is switched on for a brief period of time inducing a phase gradient of the nuclei in this direction. Each point in the object could thereby be identified by its unique frequency/phase-combination. To generate a typical image of 256×256 pixels, 256 signals must be obtained using different phase-encoding pulses. Each phase-encoding pulse corresponds to a row in the *k-space* presentation of the image, analogous to the spatial frequency description of the ultrasound image in Fig. 2.7(b). The MRI k-space would have data in all regions of k-space, in contrast to the characteristic low-pass and band-pass filtering in ultrasound imaging. The spatial image is obtained by inverse Fourier transform. Figure 2.17 shows a magnetic resonance image of a porcine heart.

The in-plane resolution in MRI is dependent of the field of view (FOV) and the k-space matrix size (i.e. the number of phase encoding steps). Increasing the number of phase encoding steps would improve spatial resolution, but would result in increased acquisition time and poorer signal-to-noise ratio (SNR). Analogously, a reduction in slice thickness would also lead to poorer SNR, due to the reduction in the number of nuclei contributing to the signal. In order to achieve a sufficient temporal resolution for cardiac imaging, the magnetic resonance imaging usually is performed using gated acquisition over several heart beats during breath holds.

MRI tagging

MRI tagging is a method for manipulating the magnetization of the nuclei to obtain markers in the image that makes it possible to track the deformation of the cardiac wall. The methodology was first introduced by Zerhouni et al. (1988). A refined tagging methodology — spatial modulation of magnetization (SPAMM)— was suggested by Axel and Dougherty (1989). In SPAMM, a special pulse sequence is set up before the conventional imaging sequence. The pulse sequence is usually performed in the first milliseconds after end-diastole and consists of two electromagnetic pulses and

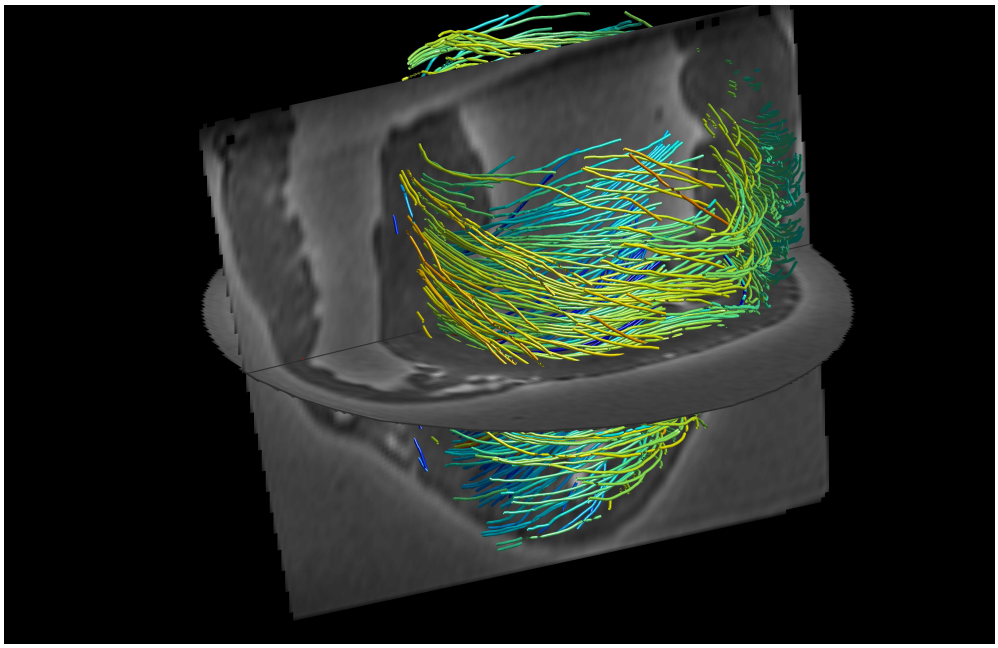

Figure 2.19: Cardiac fiber-tracking by Diffusion Tensor MRI. MRI data from an excised porcine left ventricle embedded in poly vinyl alcohol cryogel (PVA-C) were obtained using an Achieva 3T scanner (Philips Medical System, Best,Netherlands). Fiber pathways were estimated using DTI Studio (Jiang et al., 2006) and visualized in Matlab (The MathWorks, Inc. Natick, MA).

a gradient field: The first pulse produces a net magnetic moment perpendicular to the field. The gradient field is switched on to create a spatial phase gradient before the second pulse flips some of the magnetic moment back in the direction of the beam. This leads to a sinusoidal line pattern in the direction of the phase gradient in the magnetic resonance images — shown to the left in Fig. 2.18 — that follows the material motion of the myocardium. By combining this line pattern with a second acquisition where the gradient is set perpendicular to the first, a grid pattern that accommodates two-dimensional tracking is obtained (Fig. 2.18). The original method suffered from fading of the tags during the cardiac cycle. The fading is reduced by using complementary SPAMM (CSPAMM) technique (Fischer et al., 1993) and high field strength (e.g. 3 $Tesla$), which make it possible to create tagging patterns that persist the entire cardiac cycle. The CSPAMM methodology has recently been extended to three dimensions, imposing a 3D-tagging grid (Ryf et al., 2002; Rutz et al., 2008). Many variants of MRI tagging have been suggested. A survey of advantages and disadvantages of the most common techniques is given in Axel et al. (2005).

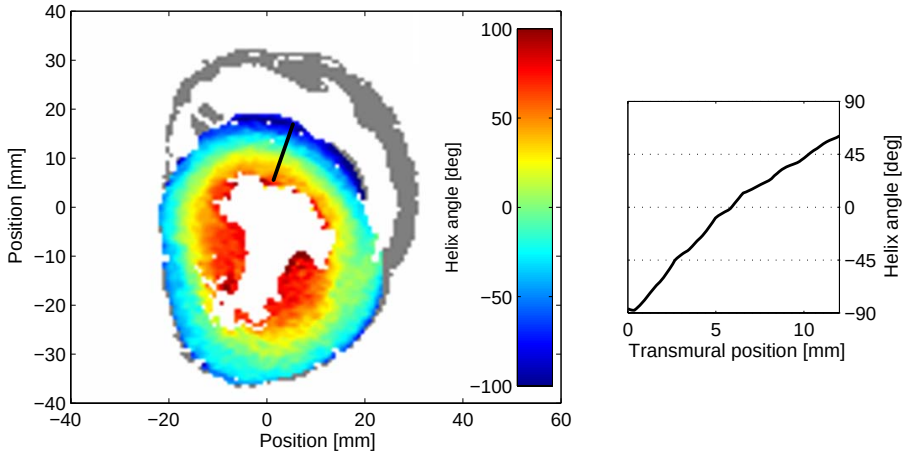

Figure 2.20: Helix angles in a short axis image based on DT-MRI. The plot of helix angles in the right panel is based on the septal transmural segment indicated by a thick black line in the short-axis view. (The helix angles were calculated as the angle between the first eigenvector from DT-MRI and the circumferential direction.)

Diffusion tensor MRI

Diffusion Tensor MRI (DT-MRI) is a method for measuring the directivity of water diffusion in anisotropic tissues. The local water diffusion might be more restricted in some directions than others due to the structural anisotropy in some tissues. Diffusion imaging measures the net temporal dephasing of the nuclear spins due to the diffusion of water molecules between voxels with different precession frequency encoding. In order to obtain the directional dependence of diffusion, the diffusion scan is repeated using frequency gradients in three or more different directions.

The foundations of DT-MRI were laid in the mid-eighties (Taylor and Bushell, 1985). The methodology has been an important tool in studies of anisotropic tissues, and have been extensively used in studies of white-matter connectivity of the brain. The three-dimensional structure of the neural tracts can be reconstructed based on the diffusion tensors obtained from DT-MRI; a procedure known as *tractography*.

The methodology can also be used to estimate the myocardial fiber organization (Tseng et al., 2003). Generally, a long acquisition time is necessary to obtain diffusion tensor images of high quality, and the methodology is therefore best suited for stationary tissues. Nevertheless, DT-MRI has also been used in *in vivo* hearts (Edelman et al., 1994).

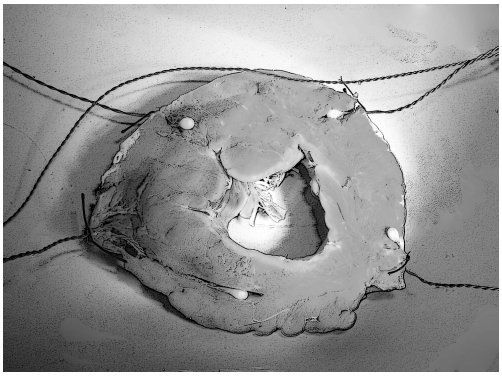

(a) *Ex vivo* slice of canine left ventricle showing the placement of the sonomicrometric crystals.

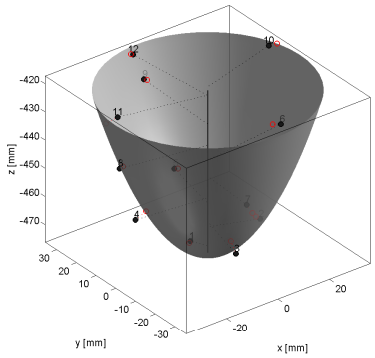

(b) Reconstructed crystal positions and fitted ellipsoidal surface.

Figure 2.21: Sonomicrometry.

Figure 2.19 shows myocardial fiber pathways and Fig. 2.20 shows estimated helix angles based on DT-MRI of an *ex vivo* porcine heart. (These figures are based on the same DT-MRI data that was used in Paper D).

2.5.2 Sonomicrometry

Sonomicrometry is a distance-measurement technology based on the transmit time of sound between a set of small piezo-electric transducers, often referred to as *crystals*. Assuming that the sound velocity in the intervening medium is known, any inter-crystal distance can be calculated from the time interval from a sound pulse is emitted by one of the crystals till it is detected by another. The spatial resolution of the displacement estimate is governed by the time resolution of the propagation time

counter and the speed of sound in the propagation medium. A standard setup (Sonometrics Corporation, London, Canada) with a 64 MHz crystal oscillator thus gives a resolution of 24 μm in soft tissue. In addition, there is an offset error in the measurement of the absolute distance between two crystals due to system delays and crystal geometries. This error is estimated by the manufacturer to be less than 1.5 mm (Sonometrics, 2008). In the system documentation, the manufacturer also mentions variations of the speed of sound and the detection of the signal at the receiver. The failure to trigger at the same peak within each emitted ultrasound pulse, can be detected as an instantaneous level-shift in the observed distance measure. The temporal resolution of the distance measures depends on the number of crystals and the maximal distance between the crystals. In addition the data acquisition hardware and software sets an upper limitation of the sampling rate. With a setup with 11 crystals (as in Paper A included in this thesis) sampling rates of 200 Hz is achievable. Cardiac sonomicrometry is usually limited to open-chest animal models where the crystals are implanted into or attached to the myocardium, which might affect the physiology of the heart. In order to derive measures that depends on geometry — as e.g. volumes or rotation — the positions of the crystals must be reconstructed from the distance measurements. The relative positions of the crystals may be found using a triangulation scheme leading to an over-determined system, as implemented in the SonoXYZ software (Sonometrics Corp.) Fig. 2.21(a) shows sonomicrometric crystals implanted in the left ventricle, and Fig. 2.21(b) shows the reconstructed positions of crystals placed inside the myocardium.

Chapter 3

Contributions

This chapter gives a brief summary of the contributions related to my PhD project. The four main papers are included in whole in the second part of this thesis. A complete list of co-authored publications is given on page 57.

3.1 Methods for ultrasound-based quantification of rotation and twist

Although studies by MRI tagging had demonstrated the importance of left ventricular rotation and twist to cardiac function, there was no clinically established method to obtain these parameters by echocardiography. However, speckle tracking methods capable of tracking myocardial motion in ultrasound images had been developed, which potentially could be used to assess rotation. Paper A: *New Noninvasive Method for Assessment of Left Ventricular Rotation: Speckle Tracking Echocardiography* presents and validates an ultrasound method to obtain LV rotation and twist based on speckle tracking in short-axis views of the ventricle. Speckle tracking of a set of myocardial regions of interest (ROIs) was performed on basal, equatorial and apical short axis B-mode images of the left ventricle using custom-made post-processing software. The in-plane rotations was calculated as the angular displacement of each ROI relative to the center of a best-fit circle through all ROIs. The twist angle (in the paper referred to as torsion) was calculated as the difference in rotation between the apical and basal slices.

The STE method was evaluated through an experimental open-chest study on 13 dogs where the hearts were exposed to a range of experimental settings known to alter LV rotation, and a clinical study on 29 healthy volunteers. In the experimental study, sonomicrometry was selected as a reference method due to its high accuracy and temporal resolution, and due to the possibility to record data close in time with the ultrasound acquisitions. In the clinical study, MRI tagging was used as a reference method as being the only available clinical method for assessment of LV rotation.

Rotation and twist by STE showed good correlation and agreement when compared with sonomicrometry, with absolute bias and standard deviation less than 0.3° and 1.3°, respectively. When compared with MRI, absolute bias and standard deviation for peak rotation were less than 0.6° and 1.6°, respectively. Intraobserver agreement was $0.4 \pm 1.6^\circ$ for peak rotation.

Dr. Thomas Helle-Valle was the main author of this paper. My task in this project was to accommodate the speckle tracking algorithm to be able to measure rotation,

as well as develop an algorithm that was able to estimate left ventricular rotation and twist from a sparse set of sonometric crystals.

The growing interest in the importance of the rapid untwisting rate associated with isovolumic relaxation made it desirable to acquire rotation velocity traces at high temporal resolution. The temporal resolution of the velocity estimates by Tissue Doppler Imaging (TDI) is usually much higher than what is achievable by tracking in conventional B-mode images. Additionally, the Doppler approach provides the velocity field in each frame. Angular velocities could therefore be calculated directly, without performing noise amplifying derivation. However, in contrast to speckle tracking, TDI only provides velocity components in the direction of the beams. Determination of rotational myocardial motion is therefore in general impossible. However, the degrees of freedom of the cardiac motion could be reduced by assuming that the left ventricular wall remains approximately circular in the short axis view. This assumption implies that the radial contraction velocity of the left ventricle, relative to a common center point, would be the same around the whole myocardial circumference. Furthermore, the tangential velocities contributing to LV rotation would be perpendicular to these contraction velocity vectors. The local tangential velocities could thereby be estimated based on an initial circular geometry and the TDI velocity field — at least for the case where there is no lateral motion of the center point. The method is presented Paper B: *A new Tissue Doppler Method for Examination of Left Ventricular Rotation.* Parallel to the work with the TDI rotation method, another TDI-based method for LV rotation was suggested independently by Notomi et al. (2005). The method in our paper can be regarded as a generalization or extension of the study by Notomi et al. that utilizes more of the velocity information from TDI, and makes it theoretically possible to acquire regional differences in rotation.

In Paper B, LV twist and twist velocity (twisting rate) from the new TDI method was compared with results from MRI tagging, a commercial STE method, and our own implementation of the TDI method proposed by Notomi et al. on 21 healthy subjects. Although the general shape of the twist and twist velocities traces from the different methods were comparable — and consistent with previous studies — the results showed an systematic underestimation of absolute rotation by the TDI methods when compared with MRI and STE. Additionally, the inter- and intra-observer variability in all methods were surprisingly high in all methods considering the high level of automatization. This might indicate that the results are sensitive to small deviations in the user initialization. No consistent regional circumferential differences were found, which was explained by the high dependence on the estimated center of rotation: Small deviations in the center estimate could induce significant regional variation in the circumferential rotation values.

The TDI method presented in Paper B relies on user input to account for the lateral motion of the ventricular center point. As the beams in a sector image intersect the myocardium at different insonification angles, we hypothesized that global LV displacement and rotation could be formulated as a minimization problem. A search algorithm was applied to find the change in global geometric parameters that minimized the deviations between the observed TDI velocities and the velocities

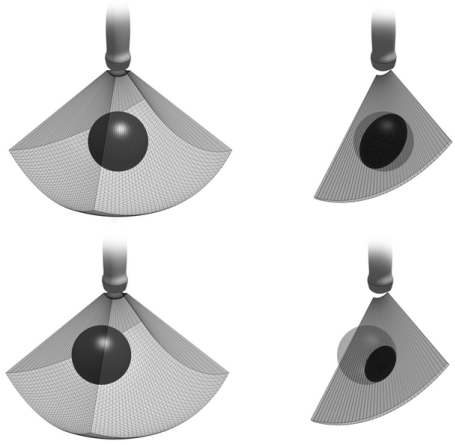

Figure 3.1: 3D imaging versus 2D imaging.

predicted by the circular model. This methodology was presented in a proceedings paper (Crosby et al., 2005) but the preliminary results indicated that some of the angular rotation was misinterpreted as lateral displacement of the center point, which resulted in an underestimation of the true global rotation.

3.2 Quantification of deformation and rotation in 3D ultrasound data

In recent years, several of the main manufacturers of cardiac ultrasound systems have been developing cardiac matrix array probes that can provide real-time volume ultrasound data. Our department has been working with speckle tracking in conventional 2D B-mode images in order to estimate in-plane strain and strain rate (Ingul et al., 2005; Amundsen et al., 2006), and the framework could potentially be extended to track tissue deformation in full-volume ultrasound data. The main motivation for tracking in volume data is the possibility to reveal the spatial motion of actual material points inside the myocardium during the cardiac cycle. In 2D views, it is only possible to track the apparent in-plane displacements, where the corresponding myocardial points can change from frame to frame due to out-of-plane displacements as in Fig. 3.1. However, as mentioned in the previous chapter, the number of beams needed to acquire a full volume image of the LV limits the achievable spatial and temporal resolution. This increases the chance of erroneous tracking, which necessitates regularization of the tracking estimates.

in Paper C: *3D Speckle Tracking for Assessment of Regional Left Ventricular Function*, we present a method for tracking a mesh of material myocardial points in full-volume acquisitions of the LV, and we utilize the tracked mesh to calculate

LV rotation and strains. The paper also outlines the main challenges in assessment of regional function based on full-volume ultrasound data. In Paper C, the tracking method was applied on simulated ultrasound data from a finite element model of the LV with an infarcted region. The results from the tracking showed good agreement with the *ground truth* values from the underlying model, but failed to capture the very rapid longitudinal elongation in one of the infarcted segments. The feasibility of the method was also demonstrated on real ultrasound data in three subjects: One young healthy volunteer, and two patients with respectively anterior and inferior myocardial infarction. For the patients, the results from the 3D speckle tracking were compared with Bulls-eye plots with wall motion scoring based on standard 2D B-mode images. Although both methods showed reduced contraction in the infarcted areas, there were some discrepancies in the individual segments.

3.3 Improving simulated ultrasound images

In the process of developing tracking motion in 3D data sets, it became clear that simulated ultrasound data would be highly desirable in the development of methods operating on volume data. In conventional 2D echocardiography, the automatized displacement estimates can be readily evaluated by eye-balling or manual measurements by an experienced user. In 3D tracking, the motion is no longer restricted to a plane, and combined with the vast amount of data it becomes difficult to visually evaluate the estimated displacements. Likewise, direct comparison with alternative methods is often — as seen in the three other papers — problematic.

Propelled by advances in computer hardware, the use of computer simulated ultrasound data has become a standard tool in ultrasound research. The *Field II* Simulation Program (Jensen, 2004) — developed and maintained by Prof. Jørgen Arendt Jensen at the Technical University of Denmark — has provided researchers and developers in the field of ultrasonics with a flexible tool for simulating ultrasound transducer fields and images based on linear acoustics. Such simulations have been extensively used in the study of probe design and beam forming. In order to make it possible to create dynamic full volume simulated ultrasound images within reasonable time limits, our department has developed a fast simulation method. However, as most ultrasound simulations of the left ventricle, the left ventricle was modeled as a set of uncorrelated scatterers that do not reflect the anisotropic properties of the LV myocardium.

Although several publications have described the considerable effects that cardiac anisotropy have on the backscatter signal — especially within the field of tissue characterization — these effects have so far been neglected in ultrasound simulations used for validation of methods for tracking of cardiac structures.

We therefore wanted a simple way to include the effect of tissue anisotropy that could be incorporated in the existing simulation framework. The anisotropic model should be coupled with dynamical 3D models of the LV — like the finite element model in Paper C — in order to achieve realistic dynamic simulated ultrasound data of the whole cardiac sample. The simulated results could then be used to validate tracking

methods, as was done in the 3D speckle tracking study.

As we expected the acoustic properties of the anisotropic myocardial tissue to be more correlated in the fiber direction than in the other directions, this led us to apply an ellipsoidal smoothing filter on the initially uncorrelated backscatter coefficients of the scatterer points, with the primary axis along the expected local fiber direction. This approach alters the frequency representation of the myocardial model locally, so that the resulting simulated ultrasound image would be dependent on the insonification angle.

In Paper D: *The Effect of Including Myocardial Anisotropy in Simulated Ultrasound Images of the Heart*, the new anisotropic simulation approach is presented and compared with the apparent anisotropy in real ultrasound images of a sample of the interventricular septum from a swine heart. The paper clearly demonstrates that the method is able to reproduce some of the considerable effect of anisotropy seen in real ultrasound images of the myocardium. The paper also introduces a new simple ultrasonic method to estimate the main fiber directions within an ex-vivo transmural sample of the myocardium that was used to define the filtering directions in the scatterer model. The fiber directions found by this model was consistent with reported results in previous studies and showed good agreement with fiber angles determined by DT-MRI in another swine heart of comparable size.

Although only 2D images is simulated in Paper D, the same approach can be used to include anisotropy in 3D ultrasound images, as demonstrated in the preceding proceedings paper by Hergum et al. (2006).

Chapter 4

General discussion and future directions

This chapter gives a general discussion of the methodology and results in the included papers and their implications for ultrasound-based quantification of myocardial deformation and rotation.

General considerations

Exact measurements of deformation and rotation in a beating heart is a difficult task, regardless of imaging modality. As seen in Section 2.1, the myocardium constitutes a complex structure of myocytes, blood vessels, and connective tissue. The non-uniform contraction/relaxation and accompanying thickening/thinning of myocytes within this structure, and its interaction with the blood pool and neighboring tissues, results in a highly non-uniform myocardial velocity field with large local variations in both amplitude and direction. Any LV displacement estimate might therefore be heavily dependent on the exact placement and extent of the ROI, as illustrated in Fig 4.1. It would also depend on the third dimension of the ROI, which in 2D imaging modalities is implicitly determined by the slice thickness.

Two-dimensional imaging techniques would at best capture the in-plane components of the velocity field. However, most tracking techniques cannot measure velocity directly, and the in-plane velocities is derived from the changes in position of specific image characteristics. This means that the imaging system must have a certain out-of-plane sensitivity (i.e. slice thickness, in ultrasound given by the elevational beam profile), large enough to ensure an overlap of the image content after tissue displacement, or that the imaged properties of the material must be correlated out-of plane. In addition, in order to avoid bias in the displacement estimates, the PSF of the imaging system has to be reflection symmetric about the imaging plane. In ultrasound, asymmetry in the PSF could be caused by for example insufficient probe access. Analogously, material properties that is correlated obliquely out-of-plane — for example a blood vessel intersecting the imaging plane — can cause errors in the estimated in-plane velocity components. The effect is illustrated in Fig. 4.2 where the apparent rotation is a result of translation of obliquely correlated structures. For MR tagging, the analog would be that the tag-planes (observed as tag-lines in the image plane) are oriented non-perpendicularly to the imaging plane, so that a through plane translation of the LV would result in apparent in-plane displacements of the tag lines.

Although these difficulties might limit the precision of noninvasive measurements of LV deformation and rotation, and might make absolute agreement between different measurements infeasible, the estimates could still be good enough to provide valuable

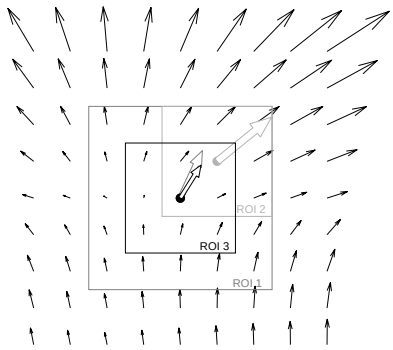

Figure 4.1: Displacement estimates (thick arrows) based on three overlapping regions of interest (ROIs) in a hypothetical myocardial velocity field (thin black arrows).

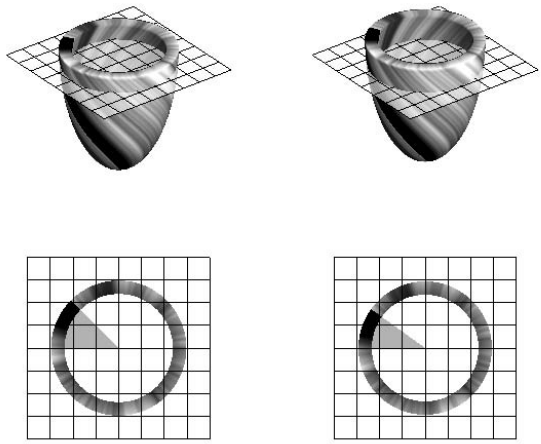

Figure 4.2: False rotation due to through-plane motion of oblique structures.

information about the cardiac function, as indicated by the results in this thesis.

4.1 Methods for ultrasound-based quantification of rotation and twist

The first of the three aims of this PhD project was to establish ultrasound-based alternatives to MRI tagging for examination of rotational motion in the left ventricle, as stated on page 3:

Aim 1: *To develop and investigate methods for quantification of rotation and twist based on short-axis ultrasound images of the left ventricle.*

Two different approaches for estimation of rotation and twist based on short axis echocardiograms have been presented, both with the capability to quantify regional rotation: One, which is based on speckle tracking in B-mode images, and the other based on tissue Doppler. This section reviews some of the difficulties related to measurements of LV rotational motion, and then discuss the advantages and limitations of the two approaches.

Measuring myocardial rotation, twist and torsion

The twisting motion is a characteristic property of the beating heart that is clearly seen in open-chest surgery. The observed rotational pattern is an accumulation of shear strains in the myocardium, caused by the sequential activation of the helically organized cardiac muscle cells (described in Section 2.1). Presence of ischemic myocardium is expected to change shear strain locally by affecting the contraction and the elastic stiffness, and could thereby potentially alter the overall accumulated rotational motion. Despite its complexity, the pattern of rotational motion of a heart seems to be quite similar between healthy subjects, as seen in e.g. Fig. B.5. The additional observation that much of the rapid untwisting appears within the isovolumic relaxation phase has given rise to expectations of a preload independent index of LV relaxation (Burns et al., 2008). The clinical use of rotation and rotation-derived measures rest on that it exists systematical differences in the rotational motion between pathological and healthy hearts, and that it exists reliable methods for measuring these differences with sufficient precision.

However, in order to quantify rotation, an axis or point of rotation is needed. Unlike a spinning wheel or an orbiting planet, the left ventricle has no unambiguous axis of rotation. The problem with the axis definition becomes especially apparent in the case of sonomicrometry in Paper A, where very limited anatomical information was available. In this paper a center point was defined by fitting a circle to the three or four crystals that constituted each level. A more general approach where the center axis was defined as the axis of symmetry of a best-fit ellipsoid (Fig. 2.21(b)) was also tested but was not utilized in the study. To my knowledge, there are no authoritative recommendations for the definition of the LV rotational axis. Most methods based on short-axis views seem to be using a dynamic center point that is positioned in

mid-lumen at the geometrical center of the myocardial wall or in the center-of-mass of a set of ROIs within the wall. The position of the center point could therefore vary dependent on whether endo- or epicardium is used to define the LV wall (or, analogously for the center of mass, on the transmural position of the ROIs involved). In three-dimensional data sets it is most convenient to use a straight axis of rotation, although rotation might also be quantified with respect to a curved center line in order to compensate for differing LV geometries. The center axis can be estimated from the LV walls, analogous to the 2D case, or could be defined by anatomical landmarks as e.g. the apex or the mitral apparatus. As shown in Paper B, local circumferential differences in rotation are very dependent on this estimated rotational center point or axis. A slight translation of the center axis relative to the myocardium, or vice versa, might induce a significant variation in the local rotation estimates. The average rotation for a given short-axis intersection, on the other hand, is less sensitive to the exact position of the center axis. These observation limit the value of local rotation as a clinical parameter and they also indicate that the rotation estimates should be based on several ROIs.

The transmural gradient in rotation from endo- to epicardium might be an important source of the variation seen in the rotation, as the estimates become very dependent on both the transmural position and the size of the ROIs. The dependence on ROI position is likely to contribute to the high inter- and intra-observer variability associated with all methods in Paper B. The differences in position and size between the ROIs in the different methods could also have affected the agreement. Consequently, improved agreement might be expected if the ROIs in the different methods were identical, but in practice this would be difficult due to the different image modalities involved, and as some of the methods are commercial packages with limited control over the ROIs. Neither would the results from such an approach reflect the agreement achievable in a clinical setting. Additionally, the magnitude of rotation and twist angle would be dependent on the longitudinal placement of the short-axis levels. As the longitudinal gradient of rotation has been observed to be fairly linear in most of the LV, torsion is expected to be less dependent on the placement of the short-axis levels. Unfortunately, the exact distance between the short-axis levels is seldom known in 2D echocardiography..

Rotation and twist by 2D speckle tracking

Two different methods for 2D speckle tracking have been used in the thesis work: The study in Paper A is based on a modified 2D speckle tracking method developed by the Department of Circulation and Medical Imaging (Björk-Ingul and Aase, 2007) while the method used in Paper B was part of the commercial EchoPAC analysis software developed by GE Vingmed. The 2D block matching in these methods gives the displacement in each frame, and the angular displacement relative to an estimated center point is therefore easy to calculate. Rotation rates may be calculated by numerical differentiation of the rotation traces but as differentiation is noise amplifying by nature, the rotation traces usually have to be smoothed prior to differentiation.

Block matching in ultrasound images. The block-matching approach relies on the assumption that the apparent motion in the ultrasound image reflects the true motion of the object. However, the exactness of local quantitative estimates of displacements may be limited by properties of the ultrasound imaging process and of the estimation methodology. In the discussion above it has already been mentioned that oblique structures may cause artificial motion in the image, which consequently might give false minima in the agreement function of the block matching. Decorrelation of the ultrasound image between frames prevents exact agreement between the source kernel and the target kernel. Sources of image decorrelation include:

- **Out-of-plane motion.** In 2D acquisitions, the motion of scatters out of the image plane causes decorrelation. (In fact, the amount of decorrelation has been utilized in sensorless freehand 3D ultrasound to estimate the elevational displacement from 2D images (Gee et al., 2006).)
- **Deformation and rotation.** Due to the interference of the ultrasonic scatterers, the speckle pattern changes dramatically with large tissue deformation or rotation (see Fig. 2.10 in Section 2.3). Analogously, translational motion parallel to the aperture of the probe in a sector scan results in a change in insonification angle that would cause decorrelation.
- **Electronic/Thermal noise.** Non-stationary random noise decreases the correlation between frames but do not induce any systematic bias in the block matching.
- **Acoustic noise.** Reverberation (multiples reflections) and side lobes causes a position ambiguity so that signal contributions from elsewhere in the object are mixed into the sample volumes.
- **Inter-frame changes in wave propagation.** Changes in geometry might affect the beam forming, e.g cause changes in attenuation level, abberation, or geometric bending. This would change the backscattering signal from deeper structures.

The block-matching approach used in Papers A, B and C neglects any local deformation or rotation of the tissue within the ROIs. These methods would therefore observe a decorrelation when the kernel is rotated or deformed even if there is no speckle decorrelation in the image, due to the misalignment of the source kernel and target kernel. Some block-matching methods applied on optical images have allowed deformable and rotatable kernels in order to improve matching results. In ultrasound data, the inherent speckle decorrelation associated with rotation and deformation would limit the gain of such an approach.

The tracking errors due to out-of-plane motion, rotation, and deformation could be reduced by increasing frame rate so that the inter-frame changes becomes small. The amount of speckle decorrelation in the RF-data due to deformation has also been shown — in simulations — to be less for small point spread functions (PSF) (i.e. for low beam widths and short pulse lengths) and low receive frequencies (Meunier, 1998). Lower frequency leads to less phase shift when the distances between scatterer points change, and thereby less degradation of the interference pattern. Acoustic noise and inter-frame changes in wave propagation would cause errors regardless of frame rate, but might be improved by changing acquisition parameters as for example transmit

frequency.

The search area size and the kernel/ROI size are also important for the displacement estimates and are discussed in Paper C. Furthermore, the efficiency of the block-matching could be improved by restricting the search regions to a smaller region around a predicted starting search point. This starting point might be based on e.g. the displacements of the ROIs in the preceding frames, or on the motion of other ROIs in the current frame. The latter approach was used in the 3D speckle tracking method, where the search regions were displaced according to the motion of the atrioventricular plane. Nevertheless, such methods must be used with caution to avoid constraints on the motion that could lead to insufficient tracking in anomalous hearts.

Tracking quality and regularization. Due to the possibility of erroneous block-matching displacements, the tracking algorithms should include some way of handling such errors. In Paper A, the tracking quality was evaluated visually and ROIs with insufficient tracking were excluded from analysis. The proprietary STE method used in Paper B automatically suggested exclusion of segments based on an internal quality measure. However, exclusion of segments based on these suggestions did not improve agreement for rotation and twist angle and the automatic exclusion was therefore overruled in the study. Automatic assessment of the reliability of the displacement estimates is difficult due to the many different sources of error. A measure of the inter-frame decorrelation of the ROI, as for example the normalized cross correlation coefficient, is a natural choice of quality measure but unfortunately it has some inconvenient limitations: Random matches in dropout or saturated regions might be rated as reliable displacement estimates, while unambiguous displacements with a single clear correlation peak at the estimated displacement could be regarded as unreliable due to generally high decorrelation due to for example deformation. A future improvement could therefore be to find a measure of tracking quality that takes the local shape of the matching function into consideration, and not only the peak value. Insufficient tracking quality could also be detected by physical considerations, as for example by disallowing crossing of ROIs or unphysiological strains or strain rates. Analogous to constraining search regions, rejection based on such constraints should be applied carefully to account for anomalous hearts. As alternative to rejecting displacement estimates *after* block matching, the ROIs could initially be placed in regions with good premises for good matching based on ROIs statistics, for example ROI intensity and variance.

In all tracking methods in this thesis, some sort of spatial smoothing was performed. As the structural forces in the wall imply tight spatial coupling of tissue displacements, spatial smoothing is expected to reduce the noise in the displacement estimates. In the case of global rotation, the averaging over several ROIs reduces the impact of a few erroneous ROIs.

In subjects with steady sinus rhythm, the total drift during the cardiac cycle could be used as an indicator for over-all tracking quality. The drift in each frame could then be compensated for by weighted subtraction of the total drift. A more advanced approach is to remove drift by combining the results of forward and backward tracking,

as in the method in Paper A.

Papers A and B show that rotation and twist by STE are very comparable with results from MRI tagging in respect to magnitude, shape of rotation traces, and interobserver and intraobserver variabilities. In addition, the B-mode images has better temporal resolution than MRI tagging, and can provide rotations traces for entire cardiac cycles without gated capture over several heartbeats. On the other hand, the block-matching approach makes STE quite dependent on the image quality of the B-mode image.

Rotation and twist by tissue Doppler

The tissue Doppler method presented in Paper B represents a different approach for estimation of LV rotation in echocardiography. Tissue Doppler imaging (TDI) calculates axial velocities based on packets of repetitive beams within a few milliseconds, and the decorrelation due to out-of-plane motion, deformation, and rotation is therefore minimal. Furthermore, the tissue Doppler images generally contains fewer beams than B-mode images, resulting in higher temporal resolution. This could potentially allow examination of rapid changes in twist, for example the rapid untwisting in the isovolumic relaxation phase.

Despite the systematical underestimation of absolute end-systolic twist by the TDI methods when compared with STE and MRI tagging, the general shape of the traces of twist and rotation were quite similar in all methods in Paper B. The underestimation could mainly be attributed to the low absolute apical rotations in systole, and a less distal placement of the apical short-axis level might therefore improve the agreement with STE and MRI. The reproducibility of the TDI methods were comparable with STE and MRI tagging. The TDI methods are vulnerable to spatial ambiguities due to reverberations or side lobes in the Doppler beamforming, and assessment of tracking quality is in general quite difficult. However, if a sample volume — due to spatial ambiguity — contains signal contributions from a different region with a different tissue velocity, this could in theory be detected as an increase in the bandwidth estimate. In any case, the visualization of the motion of the myocardial points allows for visual assessment of the tracking equivalent to the STE methods.

As a consequence of the geometric assumptions needed to calculate rotation from the observed velocity components, the TDI methods have less flexibility than STE methods. A hybrid solution that uses both speckle tracking and Doppler rotation could therefore be potentially beneficial, analogous to the combined TDI and STE method used for longitudinal strain and strain rate in Ingul et al. (2005). Such a solution would eliminate the need for the user to indicate the lateral displacement of the LV center, and might increase the robustness of the method.

4.2 Quantification of deformation and rotation in 3D ultrasound data

The second aim of this thesis was to develop a method for myocardial tracking in 3D ultrasound data:

Aim 2: *To extend the speckle tracking method to be able to measure deformation and rotation in full-volume ultrasound data of the left ventricle.*

The 3D speckle algorithm was presented and demonstrated in Paper C. The main gain is the possibility to track material points, and the related elimination of decorrelation due to out-of-plane motion. Another important benefit, is the amount of image data available without the need of changing the position of the probe. In conventional 2D imaging, geometrical assumptions of the relative position and orientation of the different views have to be made, but in the full volume data the information is gathered in a single coordinate system.

The added value of using full-volume data in the assessment of global and regional cardiac function have been questioned by cardiologists. The 3D acquisitions have generally poorer image quality than 2D images from the same patient, and the achievable frame rates are much lower. Most of the diagnostic parameters can readily be obtained from 2D views, based on acquisitions with higher quality in terms of spatial and temporal data resolution. Several studies have nevertheless reported better accuracy and reproducibility for LV volume based on 3D echocardiography than based on 2D views (Pouleur et al., 2008; Lang et al., 2006). The development of new tools for regional analysis of volume data, for example 3D speckle tracking, will make it possible to examine the potential diagnostic value of 3D ultrasound in the assessment of regional function.

Parallel to this PhD work, Toshiba has developed their own software for speckle tracking in 3D data sets that was included in their new Aplio™Artida™ultrasound system introduced spring 2008, and it can also be anticipated that other of the larger ultrasound companies are developing software for 3D tracking. The details of the companies' algorithms are unfortunately seldom available for the public, which makes objective evaluation of the chosen methodology difficult. On the other hand, many of the trade-offs and challenges exemplified by the proposed method in Paper C can be expected to be common to all tracking methods applied on LV full-volume ultrasound data.

Paper C showed promising results of the possibility to measure regional deformation and rotation in full volume data. The simulation results showed, however, an underestimation of absolute strain values that needs to be examined further.

The 3D speckle tracking method makes it possible to derive a wide range of parameters including for example directional strain, strain rate, rotation, rotation rate, twist, torsion, shear, and area strain. The selection and presentation of clinical parameters can therefore become a challenge in itself. The regional parameters might for example be shown as a set of traces (Figs. C.10 and C.11), as bulls eye plots (Fig. C.12), or as color mappings onto the dynamic LV surface obtained by the tracking (Støylen et al., 2003). The traces provides much quantitative information,

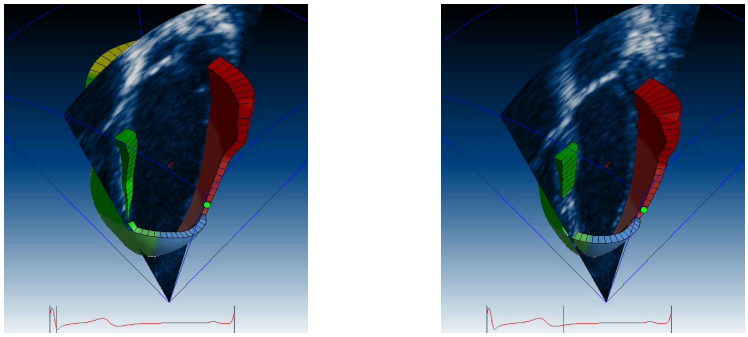

(a) End-diastole (b) End-systole

Figure 4.3: Left ventricular thickening estimated by conservation of volumes.

while the two others might provide easier assessment of regional differences. The latter presentation also include information on the LV geometry. Another practical problem is that the 3D measurements (e.g. longitudinal strain) might differ quantitatively from their 2D counterparts due to out-of-plane motion. This could cause confusion in the clinical interpretations of the measurements.

The presented method tracks only one single transmural layer. In order to measure transmural strain or wall thickening, tracking in several transmural layers could be performed. Unfortunately, the relatively thin wall compared to the size of the ROIs makes robust transmural tracking difficult. However, if the myocardium is assumed to the be incompressible, the thickening can be approximated from the longitudinal and circumferential strain together with geometrical considerations to account for the curvature of the mesh as in Fig. 4.3.

To sum up, the preliminary results of 3D speckle tracking is promising but larger clinical studies have to be performed in order to investigate the diagnostic value of 3D strain and rotation compared to conventional 2D imaging. Furthermore, optimization of the parameters within the algorithm as for example ROI sizes, threshold values for rejection of displacement estimates, and amount of regularization, might improve the overall tracking results. Moreover, for unselected patient data, a good tracking quality index would be crucial in order to detect and reject unreliable displacements estimates. Finally, it should also be noted that real-time 3D ultrasound imaging itself still is in its early stages of development, and improvements in the scanner technology that could lead to better image quality or higher temporal resolution might be expected in the coming years.

4.3 Improving simulated ultrasound images

The final aim has implicitly been discussed already in the papers and in the above sections:

Aim 3: *To investigate and discuss fundamental limitations associated with ultrasound-based assessment of left ventricular deformation and rotation.*

However, in relation to Papers C and D, it might be appropriate to comment on the use of computer simulated ultrasound data in the context of this aim.

The role of simulated ultrasound data in validation of tracking methods. As computer simulations are not able to incorporate all properties of real-life ultrasound acquisitions, testing of tracking methods on synthetic data must be regarded as a supplement, not as an alternative to experimental and clinical validation. Nevertheless, computer simulations provide information that is difficult or impossible to obtain by other means. As already mentioned, it is especially difficult to obtain a ground-truth reference method that can be used to assess the performance of new tracking methods in in vivo hearts. Furthermore, proprietary beamforming and data processing algorithm in ultrasound scanners might make the tracking results very dependent of distinctive features of the scanner. In computer simulations, the reference motion of each individual scatterer is known, which makes it possible to reveal inherent limitations of the tracking methods, as for example the systematical underestimation of strain values in Paper C. In addition, all parameters – as e.g. aperture, pulse shape, and apodization — are known and accessible so that individual parameters can be altered in order to see how this affects the results. In the development of new tracking methods, this knowledge may be used to tune the parameters in the tracking algorithm itself or to identify the scanner configuration that gives the best results for a certain tracking algorithm.

In order to become a powerful tool, the synthetic ultrasound data must be able to reproduce the relevant characteristics of a real-life echocardiogram. Features as ultrasonic speckle pattern and random acoustic noise are often included in simulation studies. In Paper D we demonstrated that the myocardial anisotropy also has a considerable effect on the appearance of the echocardiogram, and suggested an approach to incorporate this effect in simulated ultrasound images. This anisotropy might have a significant impact on LV tracking methods like speckle tracking: Changes in the angles between local fiber directions and beam directions could cause transmural shifts of brightness that do not reflect material motion. On the other hand, if the angles do not change so much that they cause false motion, the bright regions would constitute stable markers that could assist tracking. In either case, the anisotropy should be considered in future simulation studies. Realistic LV geometry, the bright reflection from pericardium, the valve dynamics, coronary vessels, reverberations, lung shadows, and anisotropic attenuation are other echocardiographic features that might affect tracking performance and should also be considered in future simulations. Realistic motion and deformation of the cardiac structures could be obtained by finite element simulations as in Paper C, or could be constructed based on measurements from e.g. MR tagging or 3D ultrasound.

Chapter 5

Conclusions

Two ultrasound-based methods for non-invasive assessment of left ventricular rotation and twist have been developed in this PhD project, as alternatives to MRI tagging. The method based on 2D speckle tracking is a flexible tool for assessing rotational motion and was shown to have good agreement with MRI tagging with comparable reproducibility and better temporal resolution. The method based on tissue Doppler velocities showed a systematic underestimation of rotation and twist but had comparable reproducibility. The use of Doppler velocities gives a more direct estimation of rotation rates and a higher temporal resolution, and might therefore be useful in the study of e.g. the rapid left ventricular untwisting. There might also be a potential benefit of combining these two methods, however, this was not investigated in this thesis.

Furthermore, a method for tracking of left ventricular strain and rotation based on 3D speckle tracking in full volume data sets has also been developed as a part of the thesis work. The testing on simulated ultrasound images and on in vivo patient data have provided promising results for 3D-based analysis of regional cardiac function but the method must be validated in a larger population before any conclusions on its clinical value could be drawn.

In relation to the testing of the tracking methodology, a new approach for incorporation of myocardial anisotropy has been developed and has been used to simulate the angle-dependent backscattering seen in a small rotating sample of the intraventricular septum. The new approach explains the regions of increased backscatter intensities seen within the myocardium in ultrasound images of real hearts, and makes it possible to obtain more realistic simulated data that could be utilized in future testing of tracking methods.

List of publications

Below is a complete list of publications authored or co-authored during the thesis work.

Peer reviewed papers

- Jonas Crosby, Torbjørn Hergum, Espen W. Remme, and Hans Torp (2008). The effect of including myocardial anisotropy in simulated ultrasound images of the heart. *IEEE Trans. Ultrason. Ferroelectr. Freq. Control.* [Article in press.]
- Jonas Crosby, Brage H. Amundsen, Torbjørn Hergum, Espen W. Remme, S. Langeland, and Hans Torp (2008). 3D speckle tracking for assessment of regional left ventricular function. *Ultrasound Med. Biol.* [Article in press.]
- Brage H. Amundsen, Jonas Crosby, Per Arvid Steen, Hans Torp, S.A. Slørdahl, and Asbjørn Støylen (2008). Regional myocardial long-axis strain and strain rate measured by different tissue Doppler and speckle tracking echocardiography methods: a comparison with tagged magnetic resonance imaging. *Eur. J. Echocardiogr.* [Article in press, doi:10.1093/ejechocard/jen201.]
- Jonas Crosby, Brage H. Amundsen, Thomas Helle-Valle, Per Arvid Steen, and Hans Torp (2008). A new tissue Doppler method for examination of left ventricular rotation. *Ultrasound Med. Biol.* [Article in press, doi:10.1016/j.ultrasmedbio.2008.03.022.]
- Brage H. Amundsen, Thomas Helle-Valle, Thor Edvardsen, Hans Torp, Jonas Crosby, Erik Lyseggen, Asbjørn Støylen, Halfdan Ihlen, J.A. Lima, Otto A. Smiseth, and Stig A. Slørdahl (2006). Noninvasive myocardial strain measurement by speckle tracking echocardiography: validation against sonomicrometry and tagged magnetic resonance imaging. *J. Am. Coll. Cardiol.*, vol. 47, pp. 789–793.
- Thomas Helle-Valle, Jonas Crosby, Thor Edvardsen, Erik Lyseggen, Brage H. Amundsen, Hans-Jørgen Smith, Boaz D. Rosen, João A.C. Lima, Hans Torp, Halfdan Ihlen, and Otto A. Smiseth (2005). New noninvasive method for assessment of left ventricular rotation: speckle tracking echocardiography. *Circulation*, vol. 112, pp. 3149–3156.

Conference proceedings papers

- Torbjørn Hergum, Jonas Crosby, Marit Jordet Langhammer, and Hans Torp (2006). The effect of including fiber orientation in simulated 3D ultrasound images of the heart. *Proceedings of the IEEE Ultrasonics Symposium*, pp. 1991–1994. [Poster session presented at: 2006 IEEE Ultrasonics Symposium, Oct 3-6,

Vancouver, Canada.]

- Jonas Crosby, Thomas Helle-Valle, Brage H. Amundsen, and Hans Torp (2005). Tracking of regional left ventricular rotation by tissue Doppler imaging. *Proceedings of the IEEE Ultrasonics Symposium*, pp. 2050–2053. [Poster session presented at: 2005 IEEE Ultrasonics Symposium, Sept 18-21, Rotterdam, The Netherlands.]

Conference poster presentations

- Brage H. Amundsen, Jonas Crosby, Per Arvid Steen, Hans Torp, Asbjørn Støylen, and Stig A. Slørdahl (2007). Regional myocardial strain measured by four different automated echocardiographic methods - a comparison with MRI tagging. Poster session presented at: EuroPrevent 2007, Apr 19-21, Madrid, Spain.
- Jonas Crosby, Thomas Helle-Valle, Brage H. Amundsen, and Hans Torp (2005). Measurement of regional left ventricular rotation by tissue Doppler imaging. Poster session presented at: Euroecho 9, Dec 7-10, Florence, Italy.
- Brage H. Amundsen, Siri Malm, Lene Annette Rustad, Jonas Crosby, Asbjørn Støylen, Hans Torp, and Stig A. Slørdahl (2005). Speckle tracking echocardiography: angle-independent strain measurements with better repeatability than strain from tissue Doppler imaging". Poster session presented at: Euroecho 9, Dec 7-10, Florence, Italy.
- Brage H. Amundsen, Thomas Helle-Valle, Hans Torp, Jonas Crosby, Asbjørn. Støylen, Halfdan Ihlen, Otto A. Smiseth, and Stig A. Slørdahl (2004). Ultrasound speckle tracking reduces angle dependency of myocardial strain estimates- Validation by sonomicrometry . Poster session presented at: Euroecho 8, Dec 1-4, Athens, Greece.

References

Alam, S. and J. Ophir (1997). On the use of envelope and RF signal decorrelation as tissue strain estimators. *Ultrasound Med. Biol. 23*, 1427–1433.

Amundsen, B., T. Helle-Valle, T. Edvardsen, H. Torp, J. Crosby, E. Lyseggen, A. Støylen, H. Ihlen, J. Lima, O. Smiseth, and S. Slørdahl (2006). Noninvasive myocardial strain measurement by speckle tracking echocardiography: validation against sonomicrometry and tagged magnetic resonance imaging. *J. Am. Coll. Cardiol. 47*, 789–793.

Angelini, E. and O. Gerard (2006). Review of myocardial motion estimation methods from optical flow tracking on ultrasound data. *Conf. Proc. IEEE Eng. Med. Biol. Soc. 1*, 1537–1540.

Axel, L. and L. Dougherty (1989). MR imaging of motion with spatial modulation of magnetization. *Radiology 171*, 841–845.

Axel, L., A. Montillo, and D. Kim (2005). Tagged magnetic resonance imaging of the heart: a survey. *Med. Image Anal. 9*, 376–393.

Barron, J. L., D. J. Fleet, and S. S. Beauchemin (1994). Performance of optical flow techniques. *Int. J. Comput. Vision 12*(1), 43–77.

Basarab, A., W. Aoudi, H. Liebgott, D. Vray, and P. Delachartre (2007). Parametric deformable block matching for ultrasound imaging. *Proc. Int. Conf. Image Process.*, 429–432.

Bjålie, J., E. Haug, O. Sand, Ø. Sjaastad, and K. Toverud (2001). *Menneskekroppen.* Oslo, Norway: Gyldendal.

Björk-Ingul, C. and S. Aase (2007). Automated strain and strain rate. In T. Marwik, C.-M. Yu, and P. Sun (Eds.), *Myocardial imaging — Tissue Doppler and speckle tracking*, Chapter 24, pp. 278–87. Blackwell publishing.

Bjåstad, T., S. Aase, and H. Torp (2007). The impact of aberration on high frame rate cardiac B-mode imaging. *IEEE Trans. Ultrason. Ferroelectr. Freq. Control 54*, 32–41.

Bohs, L. and G. Trahey (1991). A novel method for angle independent ultrasonic imaging of blood flow and tissue motion. *IEEE Trans. Biomed. Eng. 38*, 280–286.

Boukerroui, D., J. Noble, and M. Brady (2003). Velocity estimation in ultrasound images: a block matching approach. *Inf. Process. Med. Imaging 18*, 586–598.

Brekke, S., S. Rabben, A. Støylen, A. Haugen, G. Haugen, E. Steen, and H. Torp (2007). Volume stitching in three-dimensional echocardiography: distortion analysis and extension to real time. *Ultrasound. Med. Biol. 33*, 782–796.

Burns, A., I. McDonald, J. Thomas, A. Macisaac, and D. Prior (2008). Doin' the twist: new tools for an old concept of myocardial function. *Heart 94*, 978–983.

Crosby, J., T. Helle-Valle, B. Amundsen, and H. Torp (2005). Tracking of regional left ventricular rotation by tissue Doppler imaging. *Proc. IEEE Ultrason. Symp.*, 2050–2053.

D'hooge, J., A. Heimdal, F. Jamal, T. Kukulski, B. Bijnens, F. Rademakers, L. Hatle, P. Suetens, and G. R. Sutherland (2000). Regional strain and strain rate measurements by cardiac ultrasound: Principles, implementation and limitations. *Eur. J. Echocardiography 1*(3), 154–170.

D'hooge, J., C. Missant, P. Claus, S. Rex, E. Eroglu, F. Rademakers, and P. Wouters (2006). Gradients in radial strain across the cardiac wall studied with epicardial ultrasound. *Proc. IEEE Ultrason. Symp.*, 748–751.

Ding, L., A. A. Goshtasby, and M. Satter (2001). Volume image registration by template matching. *Image Vision Comput. 19*(12), 821–832.

Edelman, R., J. Gaa, V. Wedeen, E. Loh, J. Hare, P. Prasad, and W. Li (1994). In vivo measurement of water diffusion in the human heart. *Magn Reson Med 32*, 423–428.

Elen, A., D. Loeckx, H. F. Choi, H. Gao, P. Claus, F. Maes, P. Suetens, and J. D'hooge (2007). Cardiac strain estimation using spatio-temporal elastic registration: In silico validation. *Proc. IEEE Ultrason. Symp.*, 1945–1948.

Fischer, S. E., G. C. McKinnon, S. E. Maier, and P. Boesiger (1993). Improved myocardial tagging contrast. *Magn. Reson. Med. 30*(2), 191–200.

Frey, G. and R. Chiao (2008, June). 4z1c real-time volume imaging transducer. White paper, Siemens Medical Solutions.

Fung, Y.-C. (1981). *Biomechanics: Mechanical Properties of Living Tissues*. New York, USA: Springer-Verlag.

Gee, A. H., R. J. Housden, P. Hassenpflug, G. M. Treece, and R. W. Prager (2006). Sensorless freehand 3D ultrasound in real tissue: Speckle decorrelation without fully developed speckle. *Med. Image Anal. 10*, 137–149.

Gilbert, S., A. Benson, P. Li, and A. Holden (2007). Regional localisation of left ventricular sheet structure: integration with current models of cardiac fibre, sheet and band structure. *Eur. J. Cardiothorac. Surg. 32*, 231–249.

Goodman, J. W. (1996). Fresnel and Fraunhofer diffraction. In *Introduction To Fourier Optics*, Chapter 4. New York: McGraw-Hill.

Hergum, T., J. Crosby, M. Langhammer, and H. Torp (2006). The effect of including fiber orientation in simulated 3D ultrasound images of the heart. *Proc. IEEE Ultrason. Symp.*, 1991–1994.

Hess, O. and J. Carroll (2008). Clinical assessment of heart failure. In P. Libby, R. Bonow, D. Mann, and D. Zipes (Eds.), *Braunwald's Heart Disease: A Textbook of Cardiovascular Medicine* (8 ed.), Volume 1, Chapter 23, pp. 561–580. Saunders Elsevier.

Ingul, C., H. Torp, S. Aase, S. Berg, A. Støylen, and S. Slørdahl (2005). Automated analysis of strain rate and strain: Feasibility and clinical implications. *J. Am. Soc. Echocardiogr. 18*, 411–418.

Jensen, J. (2004). Simulation of advanced ultrasound systems using Field II. *Proc. IEEE Biomed. Imaging*, 636–639.

Jiang, H., P. van Zijl, J. Kim, G. Pearlson, and S. Mori (2006). DtiStudio: resource program for diffusion tensor computation and fiber bundle tracking. *Comput. Methods Programs Biomed. 81*, 106–116.

Katz, A. M. (1992). *Physiology of the Heart* (2 ed.). New York, USA: Raven Press.

Lang, R., V. Mor-Avi, L. Sugeng, P. Nieman, and D. Sahn (2006). Three-dimensional echocardiography: the benefits of the additional dimension. *J. Am. Coll. Cardiol. 48*, 2053–2069.

Langeland, S., J. D'hooge, H. Torp, B. Bijnens, and P. Suetens (2003). Comparison of time-domain displacement estimators for two-dimensional RF tracking. *Ultrasound Med. Biol. 29*, 1177–1186.

LeGrice, I., B. Smaill, L. Chai, S. Edgar, J. Gavin, and P. Hunter (1995). Laminar structure of the heart: ventricular myocyte arrangement and connective tissue architecture in the dog. *Am. J. Physiol. 269*, H571–582.

LeGrice, I., Y. Takayama, and J. Covell (1995). Transverse shear along myocardial cleavage planes provides a mechanism for normal systolic wall thickening. *Circ. Res. 77*, 182–193.

Lu, Y. and W. Wang (2008). Interaction between the interstitial fluid and the extracellular matrix in confined indentation. *J. Biomech. Eng. 130*, 041011.

Lunkenheimer, P., K. Redmann, N. Kling, X. Jiang, K. Rothaus, C. Cryer, F. Wübbeling, P. Niederer, P. Heitz, S. Ho, and R. Anderson (2006). Three-dimensional architecture of the left ventricular myocardium. *Anat. Rec. A. Discov. Mol. Cell. Evol. Biol. 288*, 565–578.

Maes, F., A. Collignon, D. Vandermeulen, G. Marchal, and P. Suetens (1997). Multimodality image registration by maximization of mutual information. *IEEE Trans. Med. Imaging 16*, 187–198.

Meunier, J. (1998). Tissue motion assessment from 3D echographic speckle tracking. *Phys. Med. Biol. 43*(5), 1241–1254.

Notomi, Y., R. Setser, T. Shiota, M. Martin-Miklovic, J. Weaver, Z. Popovic, H. Yamada, N. Greenberg, R. White, and J. Thomas (2005). Assessment of left ventricular torsional deformation by Doppler tissue imaging: validation study with tagged magnetic resonance imaging. *Circulation 111*, 1141–1147.

Pluim, J., J. Maintz, and M. Viergever (2003). Mutual-information-based registration of medical images: a survey. *IEEE Trans Med Imaging 22*, 986–1004.

Pouleur, A., J. le Polain de Waroux, A. Pasquet, B. Gerber, O. Gérard, P. Allain, and J. Vanoverschelde (2008). Assessment of left ventricular mass and volumes by three-dimensional echocardiography in patients with or without wall motion abnormalities: comparison against cine magnetic resonance imaging. *Heart 94*, 1050–1057.

Robotham, J., M. Takata, M. Berman, and Y. Harasawa (1991). Ejection fraction revisited. *Anesthesiology 74*, 172–183.

Rutz, A., S. Ryf, S. Plein, P. Boesiger, and S. Kozerke (2008). Accelerated whole-heart 3D CSPAMM for myocardial motion quantification. *Magn. Reson. Med. 59*, 755–763.

Ryf, S., M. Spiegel, M. Gerber, and P. Boesiger (2002). Myocardial tagging with 3D-CSPAMM. *J. Magn. Reson. Imaging 16*, 320–325.

Sachse, F. B. (2004). *Cardiac Mechanics*, Chapter 8, pp. 199–155. Springer.

Salgo, I. (2007). Three-dimensional echocardiographic technology. *Cardiol. Clin. 25*, 231–239.

Savord, B. and R. Solomon (2003). Fully sampled matrix transducer for real time 3D ultrasonic imaging. *Proc. IEEE 1*, 945–953.

Shattuck, D., M. Weinshenker, S. Smith, and O. von Ramm (1984). Explososcan: a parallel processing technique for high speed ultrasound imaging with linear phased arrays. *J. Acoust. Soc. Am. 75*, 1273–1282.

Shekhar, R. and V. Zagrodsky (2002). Mutual information-based rigid and nonrigid registration of ultrasound volumes. *IEEE Trans. Med. Imaging 21*, 9–22.

Silcocks, P., J. Munro, R. Steeds, and K. Channer (1997). Prognostic implications of qualitative assessment of left ventricular function compared to simple routine quantitative echocardiography. *Heart 78*, 237–242.

Sonometrics (2008). Digital ultrasonic measurement system, hardware manual – version 6.0. [Available from: *http://www.sonometrics.com*].

Spaan, J. (1985). Coronary diastolic pressure-flow relation and zero flow pressure explained on the basis of intramyocardial compliance. *Circ. Res. 56*, 293–309.

Støylen, A., C. Ingul, and H. Torp (2003). Strain and strain rate parametric imaging. A new method for post processing to 3-/4-dimensional images from three standard apical planes. Preliminary data on feasibility, artefact and regional dyssynergy visualisation. *Cardiovasc. Ultrasound 1*, 11.

Taylor, D. and M. Bushell (1985). The spatial mapping of translational diffusion coefficients by the NMR imaging technique. *Phys. Med. Biol. 30*, 345–349.

Torp, H. (2000). Estimation of the blood velocity from Doppler signals. In B. Angelsen (Ed.), *Ultrasound imaging: waves, signals, and signal processing*, Chapter 11. Trondheim, Norway: Emantec.

Trew, M., B. Caldwell, G. Sands, D. Hooks, D. Tai, T. Austin, I. LeGrice, A. Pullan, and B. Smaill (2006). Cardiac electrophysiology and tissue structure: bridging the scale gap with a joint measurement and modelling paradigm. *Exp. Physiol. 91*, 355–370.

Tseng, W., V. Wedeen, T. Reese, R. Smith, and E. Halpern (2003). Diffusion tensor MRI of myocardial fibers and sheets: correspondence with visible cut-face texture. *J. Magn. Reson. Imaging 17*, 31–42.

Viola, F. and W. F. Walker (2003). A comparison of the performance of time-delay estimators in medical ultrasound. *IEEE Trans. Ultrason. Ferroelectr. Freq. Control 50*(4), 392–401.

WHO (2002). The world health report 2002 - reducing risks, promoting healthy life.

Wilson, L., D. Robinson, and M. Dadd (2000). Elastography–the movement begins. *Phys. Med. Biol. 45*, 1409–1421.

Zerhouni, E., D. Parish, W. Rogers, A. Yang, and E. Shapiro (1988). Human heart: tagging with MR imaging–a method for noninvasive assessment of myocardial motion. *Radiology 169*, 59–63.

Papers

Circulation,112(20):3149-3156, 2005

Paper A

New Noninvasive Method for Assessment of Left Ventricular Rotation: Speckle Tracking Echocardiography.

Thomas Helle-Valle*, Jonas Crosby†, Thor Edvardsen*, Erik Lyseggen*, Brage H.Amundsen†, Hans-Jørgen Smith‡ Boaz D. Rosen ¶, João A. C. Lima ¶, Hans Torp†, Halfdan Ihlen* and Otto Smiseth*

*) Department of Cardiology, Rikshospitalet University Hospital, Oslo, Norway
†) Department of Circulation and Medical Imaging, Norwegian University of Science and Technology, Trondheim, Norway
‡) Department of Radiology, Rikshospitalet University Hospital, Oslo, Norway
¶) Department of Cardiology, Johns Hopkins University, Baltimore, Md.

Background: Left ventricular (LV) torsion is due to oppositely directed apical and basal rotation and has been proposed as a sensitive marker of LV function. In the present study, we introduce and validate speckle tracking echocardiography (STE) as a method for assessment of LV rotation and torsion.

Methods: Apical and basal rotation by STE was measured from short-axis images by automatic frame to frame tracking of gray-scale speckle patterns. Rotation was calculated as the average angular displacement of 9 regions relative to the center of a best fitted circle through the same regions. As reference methods we used sonomicrometry in anesthetized dogs during baseline, dobutamine infusion, and apical ischemia, and magnetic resonance imaging (MRI) tagging in healthy humans.

Results: In dogs, peak apical rotation was $-3.7\pm1.2^\circ$ ($\pm SD$) and $-4.1\pm1.2^\circ$ and basal rotation $1.9\pm1.5^\circ$ and $2.0\pm1.2^\circ$, by sonomicrometry and STE, respectively. Rotations by both methods increased ($P < 0.001$) during dobutamine. Apical rotation by both methods decreased during left anterior descending coronary artery occlusion ($P < 0.007$), whereas basal rotation was unchanged. In healthy humans, apical rotation was $-11.6\pm3.8^\circ$ and $-10.8\pm3.3^\circ$, and basal rotation $4.8\pm1.7^\circ$ and $4.6\pm1.3^\circ$ by MRI tagging and STE, respectively. Torsion by STE showed good correlation and agreement with sonomicrometry ($r = 0.94$, $P < 0.001$) and MRI ($r = 0.85$, $P < 0.001$).

Conclusions: The present study demonstrates that regional LV rotation and torsion can be measured accurately by STE, suggesting a new echocardiographic approach for quantification of LV systolic function.

A.1 Introduction

Left ventricular (LV) torsion (or twist) plays an important role with respect to LV ejection and filling (McDonald, 1970; Rademakers et al., 1992; Gibbons Kroeker et al., 1993; Moon et al., 1994). During the cardiac cycle there is a systolic twist and early diastolic untwist of the LV about its long axis, because of oppositely directed apical and basal rotations. As viewed from the LV apex, systolic apical rotation is

counterclockwise and basal rotation clockwise. The magnitude and characteristics of this torsional deformation have been described in different clinical and experimental studies, and it is well established that LV rotation is sensitive to changes in both regional and global LV function (Hansen et al., 1991; Yun et al., 1991; Maier et al., 1992; Buchalter et al., 1994; DeAnda et al., 1995; Gibbons Kroeker et al., 1995b,a; Knudtson et al., 1997; Stuber et al., 1999; Nagel et al., 2000; Sandstede et al., 2002; Fuchs et al., 2004; Tibayan et al., 2004). Therefore, assessment of LV rotation represents an interesting approach for quantifying LV function. However, so far MRI tagging has been the only clinically available method (Maier et al., 1992; Stuber et al., 1999; Nagel et al., 2000; Sandstede et al., 2002; Fuchs et al., 2004; Buchalter et al., 1990; Fogel et al., 2000; Nagel et al., 2000; Setser et al., 2003), and implementation has therefore been limited by complexity and cost.

In the present study we introduce and evaluate echocardiographic speckle tracking as a new noninvasive method for assessment of LV rotation and torsion. Because of scattering, reflection, and interference of the ultrasound beams in myocardial tissue, speckle formations in gray-scale echocardiographic images represent tissue markers that can be tracked from frame to frame throughout the cardiac cycle. We hypothesized that STE could be an accurate and clinically applicable non-invasive method for estimating the magnitude and dynamics of LV rotation. In this study, torsion was estimated as the difference in apical and basal rotation, and the STE method was validated by comparison with sonomicrometry in a dog model and with MRI tagging in humans.

A.2 Methods

A.2.1 Experimental study

Thirteen mongrel dogs of either sex and with average body weight 23.2 kg were anesthetized with a bolus of thiopental 25 mg/kg, followed by continuous infusion of morphine ($3.5\ mg\,kg^{-1}h^{-1}$) and pentobarbital ($2\ mg\,kg^{-1}h^{-1}$), the latter reduced to half dose after 4 hours of infusion. The animals were artificially ventilated through a cuffed endotracheal tube with room air with 20% to 50% O_2. The ECG was monitored from limb leads. One femoral vein and two jugular arteries were cannulated. After a median sternotomy, the pericardium was split from apex to base and the edges of the pericardial incision were loosely resutured after instrumentation. Inflatable vascular occluders were placed around the proximal third of the left anterior descending coronary artery (LAD). Aortic, left atrial, and LV pressures were measured by micromanometers (MPC-500 Millar Instruments Inc., Houston, Texas). Data were digitized at 200 *Hz*. The dogs were placed in a supine position during recordings. The study was approved by the National Animal Experimentation Board. The laboratory animals were supplied by Center for Comparative Medicine, Rikshospitalet University Hospital, Oslo, Norway.

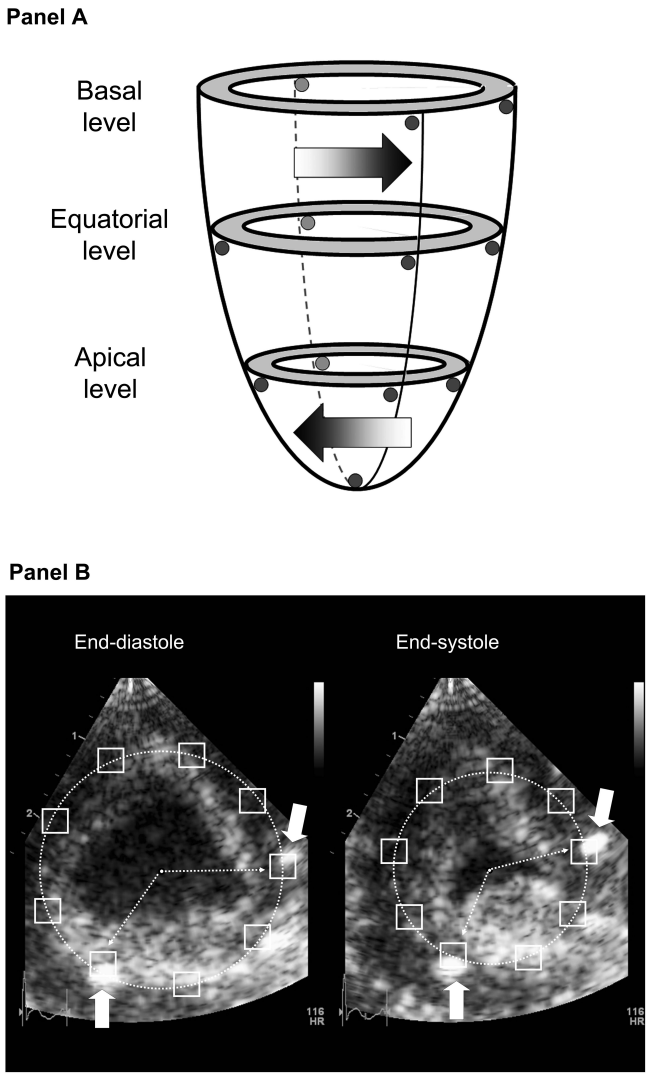

Figure A.1: Panel A: Schematic presentation of the LV with implanted crystals (filled circles) and directions of rotations of the anterior wall indicated (arrows). When viewed from the apex, apical rotation is counterclockwise and basal rotation, clockwise. Panel B: End-diastolic and end-systolic apical, 2D gray-scale echocardiographic images from an animal experiment. The ROIs (white squares) and best-fit circle are indicated. The thin dashed arrows point to ROIs, and the thick solid arrows point to crystals. The change in position of arrows from end-diastole to end-systole, confirmed the counterclockwise rotation

Sonomicrometry

For estimation of LV torsion and apical and basal rotation, 1 sonomicrometric crystal was implanted at the tip of the apex, and 11 crystals were implanted along the LV circumference at basal ($n = 3$), equatorial ($n = 4$) and apical ($n = 4$) short-axis levels (Figure 1, Panel A). Anatomy allowed only 3 crystals at the basal level. To minimize myocardial damage and to achieve reproducible and parallel planes, the crystals at each level were placed subepicardially and at distances approximately 20, 40 and 60 mm from the LV apex.

With signals obtained from the 3D grid of crystals, the coordinates of each crystal was automatically determined in space as a function of time (200 Hz). Parallel apical, equatorial and basal LV planes were constructed by interpolation of the corresponding crystal coordinates, and the in-plane positions were approximated by cubic Hermite interpolation (standard interpolation used in Matlab). The center of rotation for each LV plane was determined as the center of a best-fit circle through the interpolated coordinates. For each plane, the angular movements of the interpolated coordinates were averaged, and LV torsion was estimated as the difference in angular movement between apical and basal planes at isochronal points. Apical and basal rotation was calculated by measuring the difference in angular movement between the equatorial level, where rotation is known to be minimal (Nagel et al., 2000; Sandstede et al., 2002; Fogel et al., 2000; Henson et al., 2000; Lorenz et al., 2000; Moore et al., 2000; Nichols et al., 2002), and the apical and basal levels, respectively.

Echocardiographic recordings and analysis

LV short-axis recordings were obtained by conventional 2D gray-scale echocardiography (Vivid 7 scanner, GE Vingmed, Horten, Norway). Transducer frequencies (1.7 to 2.0 MHz), sampling rates (70 to 110 frames per second) and sector width (as narrow as possible) were adjusted for optimal speckle quality of the recordings. Short-axis echocardiograms were recorded in the same plane as used for sonomicrometry with the anatomic crystals as a reference.

Echocardiographic recordings were done immediately before the sonomicrometric recordings and analyzed with a Matlab-based program that uses the speckle patterns in the gray-scale images. The speckle tracking method with minimum sums of absolute differences of the B-mode pixel data (Bohs and Trahey, 1991), was used to track the position of a kernel region (a selected region of interest [ROI)] with a unique speckle pattern) frame by frame throughout the cardiac cycle. To avoid drift, the tracking algorithm was applied both forward and backward, and the results were averaged. The size of the ROI was 3×5 mm and the limit for maximum displacement velocity was set to 12 cm/s for vertical and 7 cm/s for lateral velocities. Nine ROIs were automatically superimposed on the echocardiographic image at end-diastole and positioned to fit the circle-shaped LV. In our experimental study, this superimposed circle was aligned with the subepicardial LV circumference.

Rarely was > 1 crystal visible in the echocardiographic image. Therefore, it was not a major problem that nonphysiological speckle patterns would falsely improve tracking quality. Figure A.1, Panel B, shows representative recordings. The starting

position of the ROIs could be adjusted manually when the tracking appeared to be poor. ROIs were excluded in regions of insufficient speckle quality because of dropouts of ultrasound data or severe reverberations. ROIs that drifted outside the wall layer being studied were also rejected. In our analyzes, 93% of the ROIs remained within the LV layer of interest.

Rotation was estimated as the average angular displacement of all 9 ROIs relative to the center of a best-fit circle through the same ROIs, frame by frame. Torsion was estimated as the difference between apical and basal rotation at isochronal points.

Experimental protocol

After baseline recordings (approximately 2 to 3 hours after thoracotomy) were obtained, dobutamine was infused at a rate of $5\mu g\, kg^{-1} min^{-1}$, and recordings were repeated. After return of dP/dt to baseline values, the LAD was occluded for 10 minutes and recordings were obtained. Baseline data were obtained from 13 dogs, whereas dobutamine intervention was not performed in the first 4 experiments. In 5 dogs, recordings during ischemia could not be obtained because of sustained ventricular fibrillation shortly after LAD occlusion. In 6 dogs, short-axis recordings from multiple levels were obtained approximately 5 minutes before and 5 minutes after pericardiotomy. This was done to explore the importance of an intact pericardium for LV rotation.

A.2.2 Clinical study

Twenty-nine healthy volunteers (15 men and 14 women, mean age 33 ± 6 years) were included. The study protocol was approved by the National Committee for Medical Research Ethics of Norway. All participants gave written, informed consent.

MRI tagging

Images were obtained using a 1.5 T scanner (Magnetom Vision Plus, Siemens, Erlangen, Germany). To standardize short-axis image planes between individuals, the basal cine image was defined just distal to the fibrous mitral ring, and the apical level, just proximal to the level with luminal closure at end-systole. Striped tags were prescribed separately in two orthogonal orientations (45° and 135°) with spatial modulation of magnetization (SPAMM) in a grid pattern with 8-mm distance between tags and a time resolution of 35 *ms*. Images were acquired during 12- to 18-second breath holds and triggered by ECG. Consistent with STE measurements, rotation by MRI tagging was calculated as the average of measurements obtained in the midendocardial and subendocardial layers. Recordings were analyzed by harmonic phase imaging (HARP version 1.0, Diagnosoft Inc. Palo Alto, CA) (Garot et al., 2000) at an experienced MRI reading center (Johns Hopkins University).

Echocardiographic recordings and analysis

Short-axis echocardiographic recordings were obtained with the volunteers in a supine left lateral position. The same scanner and acquisition settings were used as for the experimental recordings. Short-axis recordings at the basal level were obtained from a standard parasternal probe position, and recordings at the apical level, from a more distal anterior or anterolateral position. Short-axis images were acquired at approximately the same levels as the MRI cine images. Echocardiographic recordings were taken within 5 to 10 minutes before or after MRI examinations during breath holds, and an effort was made to make the LV cross section as circular as possible. The quality of the speckles improved progressively from the epicardium to the endocardium, and in many cases the subepicardial speckle quality was suboptimal. Therefore, we limited the study to assessment of rotation of the midendocardial and subendocardial layers. Criteria for adjustments or rejections of ROIs were the same as for the experimental study.

A.2.3 Reproducibility of the STE method

All echocardiographic analyzes were done without knowledge of the results from the reference methods. To assess interobserver variability, 6 experimental and 6 clinical echocardiographic recordings were randomly selected and then independently analyzed by two different observers (including selection of the cardiac cycle, placement of the ROIs and deriving the results).

A.2.4 Statistical analysis

Data are presented as $mean \pm SD$ unless otherwise stated. The rotation and torsion measurements obtained by STE and reference methods were compared by a least-squares linear-regression method and by the Bland-Altman method (Bland and Altman, 1986). In the experimental study, we used 1-way repeated-measures ANOVA followed by the Bonferroni correction for predefined comparisons of baseline versus dobutamine and baseline versus ischemia (SPSS version 12, Chicago, Illinois). Statistical differences were considered significant at $P < 0.05$. Interobserver variability was assessed by the intraclass correlation coefficient and by the Bland-Altman method.

A.3 Results

A.3.1 LV rotation and torsion by STE versus sonomicrometry: Experimental study

Figure A.2 shows representative traces of LV apical and basal rotation and torsion by STE and sonomicrometry at baseline, during dobutamine infusion, and during acute LAD occlusion (apical ischemia; Table A.1). By convention, the direction of rotation was referenced to apical views as clockwise (positive values) or counterclockwise (negative values). By both methods, an early systolic clockwise followed by

Table A.1: Results from experimental study.

	Baseline ($n = 13$)		Dobutamine ($n = 9$)		Ischemia ($n = 8$)	
	Early systole	Late systole	Early systole	Late systole	Early systole	Late systole
Heart rate, bpm	95 ± 6		91 ± 4		109 ± 3	
LV peak systolic pressure, mm Hg	97 ± 3		$118 \pm 3^*$		93 ± 5	
LV dP/dtmax, mm Hg/s	1515 ± 102		$2818 \pm 265^*$		1406 ± 129	
Apical rotation (°) by						
Sonomicrometry	0.8±0.6	3.7±1.2	1.5±1.1	−6.2±0.9*	0.4±0.6	−2.0±1.9
Echocardiography	0.7±0.4	4.1±1.2	1.2±0.7	−6.7±0.9*	0.4±0.5	−1.8±1.3*
Time to peak apical rotation (ms)						
Sonomicrometry	58±34	273±78	33±16	242±31	26±27	264±57
Echocardiography	45±22	262±52	45±8	231±52	34±39	257±74
Basal rotation (°) by						
Sonomicrometry	−1.5±1.3	1.9±1.5	−2.0±1.3	4.8±2.0*	−0.8±1.0	1.8±0.9
Echocardiography	−1.1±0.9	2.0±1.2	−1.3±0.8*	4.5±1.2	−0.4±0.3	2.3±0.8
Time to peak basal rotation (ms)						
Sonomicrometry	56±31	280±60	36±17	255±40	36±25	255±31
Echocardiography	79±33	291±64	58±21	280±41	30±21	259±35
Torsion (°) by						
Sonomicrometry	2.3±1.6	−5.5±1.9	3.4±2.2	−9.8±1.8*	1.0±1.7	−3.5±1.6
Echocardiography	1.7±1.2	−6.0±1.5	2.4±1.2	−9.5±1.3*	0.7±0.7	−3.9±1.5
Time to peak torsion (ms)						
Sonomicrometry	57±33	275±70	34±13	248±35	31±17	255±40
Echocardiography	55±30	270±65	50±17	255±30	33±27	255±40

Values are $mean \pm SD$. $^*P < 0.05$ vs. baseline (1-way repeated-measures ANOVA, P-value after Bonferroni correction).

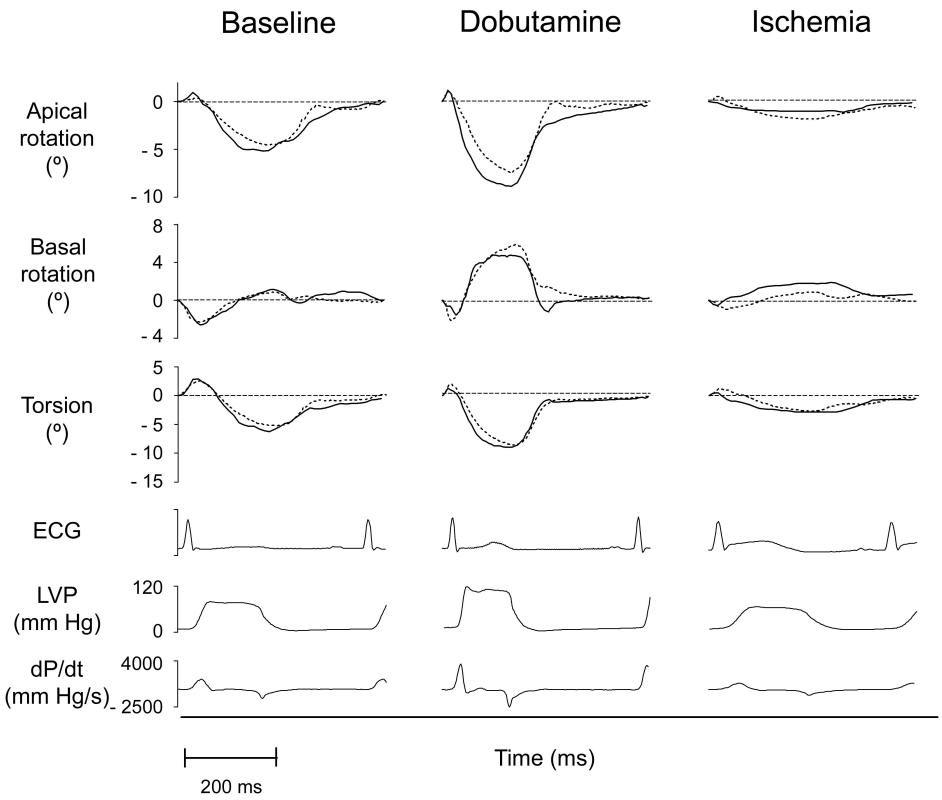

Figure A.2: Experimental study: Representative examples of apical and basal rotation and torsion at baseline, during dobutamine infusion and after 10 minutes of ischemia, as measured by sonomicrometry and STE. Clockwise rotation is represented by positive numbers. Dashed and solid lines indicate rotation as measured by sonomicrometry and echocardiography, respectively.

a counterclockwise rotation during ejection was seen at the apical level, with corresponding counterclockwise-clockwise rotations at the basal level. At baseline, peak apical rotation increased with dobutamine from $-4.1 \pm 1.2°$ to $-6.7 \pm 0.9°$ ($P < 0.001$) and from $-3.7 \pm 1.2°$ to $-6.2 \pm 0.9°$ ($P = 0.001$) measured by STE and sonomicrometry, respectively. Peak basal rotation increased from $2.0 \pm 1.2°$ to $4.5 \pm 1.2°$ ($P < 0.001$) and from $1.9 \pm 1.5°$ to $4.8 \pm 2.0°$ ($P < 0.001$). Apical rotation decreased during LAD occlusion, to $-1.8 \pm 1.3°$ ($P < 0.001$) and $-2.0 \pm 1.9°$ ($P = 0.007$) by STE and sonomicrometry, respectively, whereas basal rotation was unchanged with either method. Correspondingly, LV torsion increased during dobutamine infusion ($P < 0.001$) and decreased during LAD occlusion ($P = 0.003$ by STE and $P = 0.055$ by sonomicrometry).

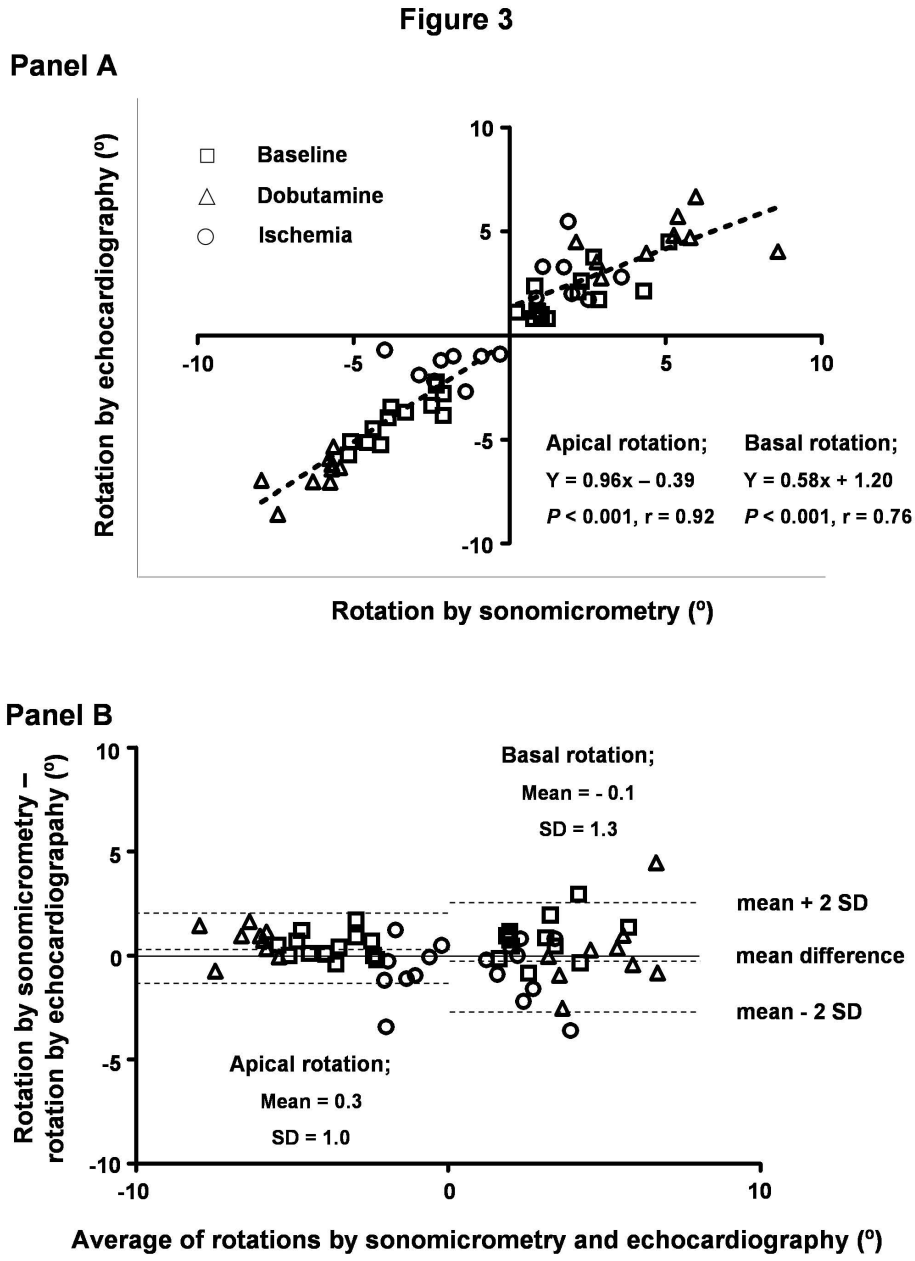

Figure A.3: Experimental data: rotation. Panel A: Correlation between rotation measured by sonomicrometry and STE. Panel B: Agreement between rotation measured by sonomicrometry and STE. The mean difference between methods and $\pm 2SD$ are indicated.

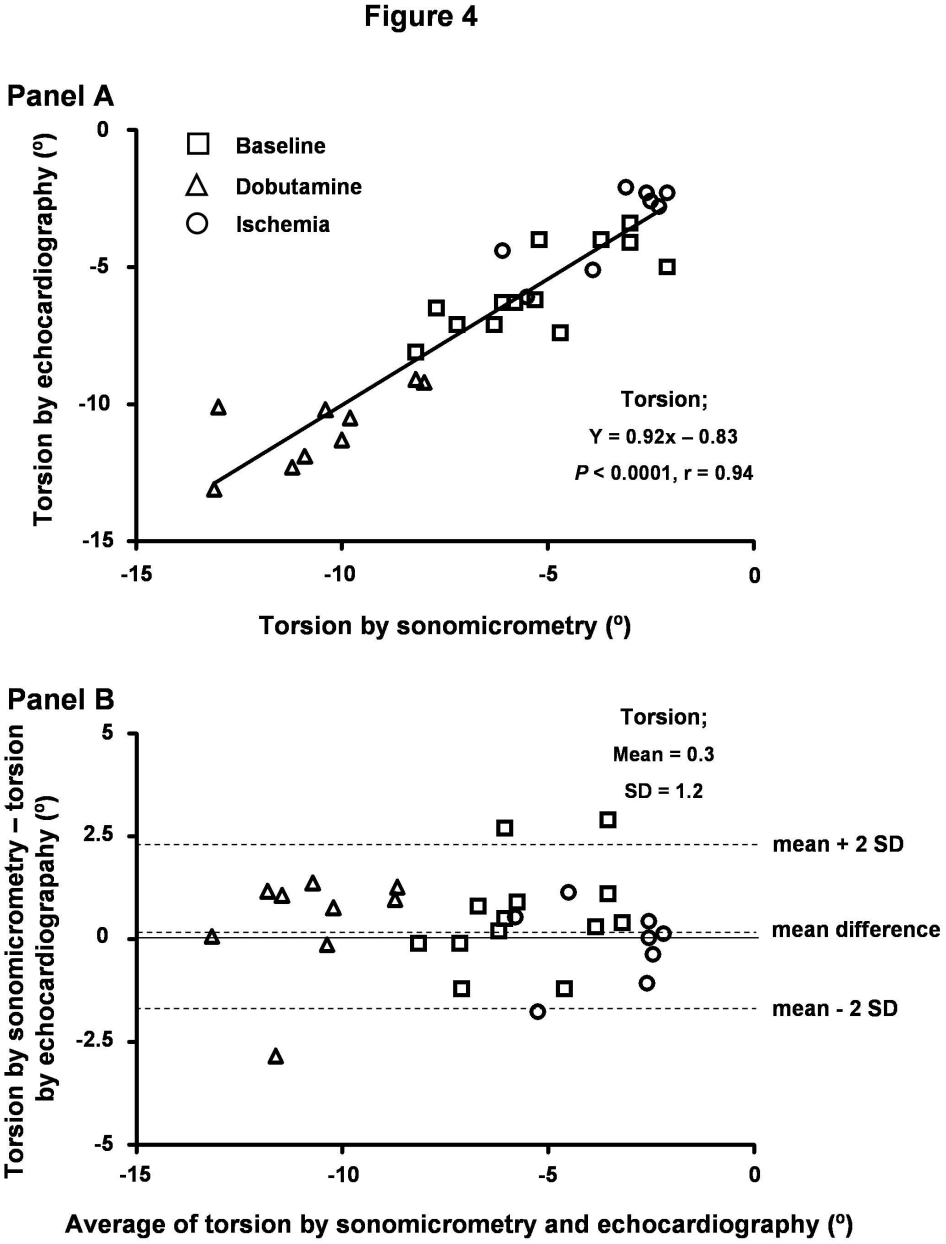

Figure A.4: Experimental data: torsion. Panel A: Correlation between torsion measured by sonomicrometry and STE. Panel B: Agreement between torsion measured by sonomicrometry and STE. The mean difference between methods and $\pm 2SD$ are indicated.

Figures A.3 and A.4 are scatter plots, with correlation and agreement data, for peak rotation and torsion by STE and sonomicrometry. Separate regression analyzes of pooled data for apical and basal rotation by STE and sonomicrometry demonstrated good correlation ($r = 0.92$, $P < 0.001$, and $r = 0.76$, $P < 0.001$, respectively), and as shown by Bland-Altman analyzes, there were no systematic differences between the methods. There was also good correlation and agreement between STE and sonomicrometry for the time to peak rotation at the apex ($y = 0.79x + 46$, $r = 0.58$, $P = 0.006$, and mean difference -10 ± 49 ms) and at the base ($y = 0.96x + 23$, $r = 0.9$, $P < 0.001$, and mean difference -13 ± 23 ms). For LV torsion the results were equally good for magnitude and timing ($y = 0.92x - 0.83$, $r = 0.94$, $P < 0.0001$ and mean difference $0.3 \pm 1.2°$, and $y = 0.90x + 23$, $r = 0.90$, $P < 0.0001$ and 2 ± 52 ms, respectively).

There was no significant change in heart rate or time to peak rotation from baseline to interventions. However, there was a tendency towards increased heart rate during both ischemia and dobutamine infusion, and a reduced time to peak rotation during dobutamine infusion. Short-axis recordings from the time of crystal implantation confirmed minimal rotation at the equatorial level ($-0.2 \pm 0.3°$).

A.3.2 LV rotation and torsion by STE versus MRI tagging: Healthy humans

Figure A.5 shows representative examples of rotation and torsion by STE and MRI tagging in healthy subjects, and Table A.2 summarizes the findings. Consistent with the experimental study, LV apical rotation during ejection was counterclockwise by STE and MRI, and basal rotation was clockwise. Early systolic basal rotation was counterclockwise by both methods, whereas early systolic apical clockwise rotation was confirmed only by STE.

Figure A.6 displays correlation and Bland-Altman plots for STE and sonomicrometry data. The correlation and agreement between the two methods were good for both peak apical rotation ($r = 0.91$, $P < 0.001$) and peak basal rotation ($r = 0.67$, $P < 0.001$). There were also good correlations and agreements for the time to peak apical rotation ($y = 0.62x + 132$, $r = 0.47$, $P < 0.012$, and mean difference 14 ± 46 ms) and for the time to peak basal rotation ($y = 0.82x + 62$, $r = 0.61$, $P < 0.001$, and mean difference 0 ± 633 ms). For magnitude of peak torsion and time to peak torsion, correlation and agreement were also good ($y = 0.85x - 1.6$, $r = 0.85$, $P < 0.001$, and mean difference $-1.4 \pm 2.0°$, and $y = 0.56x + 154$, $r = 0.49$, $P < 0.008$, and mean difference 10 ± 30 ms, respectively).

In our clinical study, ROIs were rejected in only 10% of the recordings (one ROI in 6%, and two ROIs in 4% of the recordings). In the experimental study ROIs were rejected in 18% of the recordings (one ROI in 10% and two ROIs in 8% of the recordings).

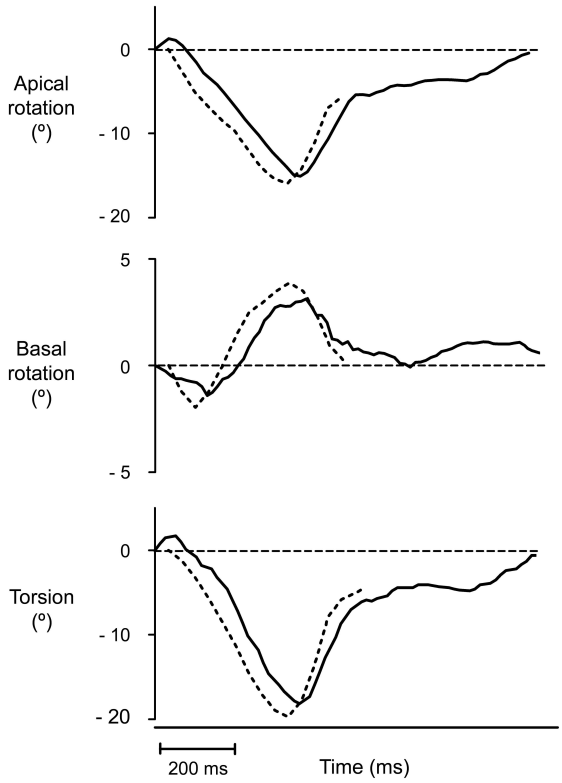

Figure A.5: Clinical study: Representative examples of apical and basal rotation and torsion, measured by MRI tagging and speckle tracking echocardiography. Rotation by MRI was not feasible for a complete heart cycle due to fading of tags. Dashed and solid lines indicate rotation by MRI and echocardiography, respectively.

A.3.3 Effect of pericardiotomy on LV rotation and torsion

Pericardiotomy caused no change in LV apical or basal rotation ($-5.7 \pm 0.5°$ and $-5.5 \pm 0.4°$ [$P = NS$], and $3.1 \pm 0.6°$ and $3.0 \pm 1.2°$ [$P = NS$], respectively). During the 2- to 3-hour period before the baseline recording, however, apical and basal rotation decreased (to $-4.2 \pm 0.6°$, $P < 0.05$ and $1.8 \pm 0.7°$, $P = NS$, respectively). Furthermore, $LV\ dP/dt_{max}$ and LV pressure, which were unaffected by pericardiotomy (2138 ± 485 and $2134 \pm 453\ mmHg/s$, $P = NS$, and 120 ± 7 and $120 \pm 6\ mmHg$, $P = NS$, respectively), decreased to 1644 ± 319, ($P = NS$) and 104 ± 5 ($P = 0.040$), respectively, at the time of baseline recordings. Similarly, torsion was unaffected by pericardiotomy (-8.7 ± 1.8 before versus $-8.6 \pm 2.0°$ after), and was reduced at the time of baseline recordings ($6.0 \pm 1.8°$, $P < 0.002$).

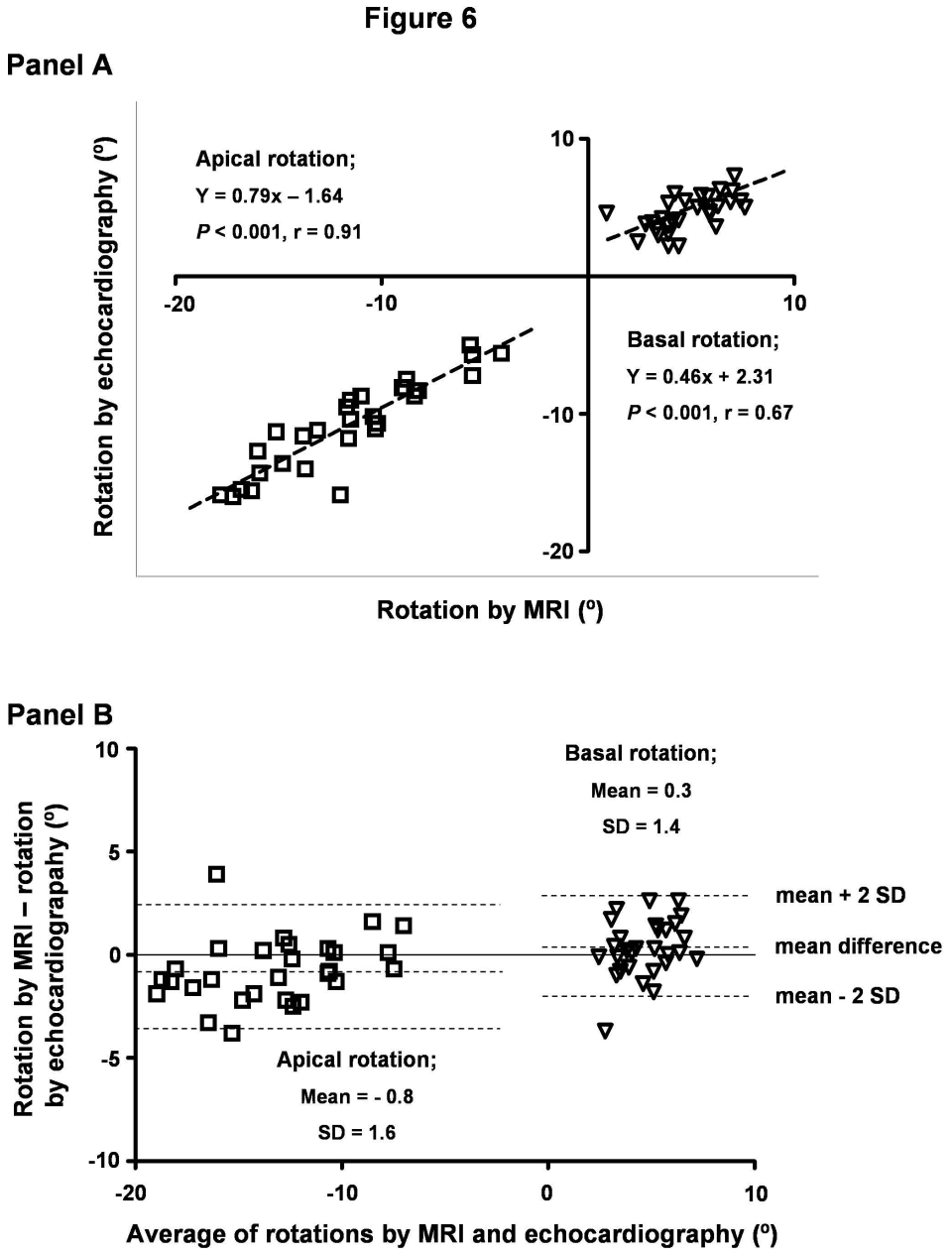

Figure A.6: Clinical data: rotation. Panel A: Correlation between rotation measured by MRI and STE. Panel B: Agreement between rotations measured by MRI and STE. The mean difference between methods and $\pm 2SD$ are indicated.

Table A.2: Results from clinical study.

	Healthy subjects ($n = 29$)	
	Early systolic	Late systolic
Apical rotation (°) by		
MRI tagging	−2.6±1.0	−11.6±3.8
Echocardiography	1.3±0.6	−10.9±3.3
Time to peak apical rotation (s)		
MRI tagging	48±17	319±32
Echocardiography	49±15	333±44
Basal rotation (°) by		
MRI tagging	−2.3±0.9	4.8±1.7
Echocardiography	−1.9±0.8	4.6±1.3
Time to peak basal rotation (ms) by		
MRI tagging	98±34	343±30
Echocardiography	112±26	342±41
Torsion (°) by		
MRI tagging	−0.3±1.0	−15.9±3.5
Echocardiography	1.2±0.5	−14.5±3.2
Time to peak torsion (ms) by		
MRI tagging	73±18	328±27
Echocardiography	80±13	338±31

Values are $mean \pm SD$.

A.3.4 Interobserver variability

Measurements by STE of peak rotation by two independent observers showed a mean difference between the two analyzes of $0.4 \pm 1.6°$. The intraclass correlation coefficient between the two observers was 0.99. The typical time spent for data analysis was < 1 minute.

A.4 Discussion

Echocardiography is one of the cornerstones in diagnosis and monitoring of cardiac diseases. However, angle independent assessment of LV deformation and rotation has only been possible by MRI tagging. The present study demonstrates that STE can measure LV torsional deformation noninvasively, by automated tracking of speckles from apical and basal short-axis recordings. The validity of our approach was tested with sonomicrometry as a reference method in an animal model and MRI tagging in humans. With sonomicrometry, the implanted myocardial crystals served as anatomic landmarks that ensured that the LV cross-sectional planes studied by the two methods were the same, and measurements could be performed only a few seconds

apart. Furthermore, in the animal model, comparison between the methods could be completed under a wide range of experimental settings known to alter LV rotation. The STE method showed dynamics, magnitudes, and timing of peak basal and apical rotation and torsion that were closely related to measurements by sonomicrometry. The same relation was found when STE was compared with MRI in healthy volunteers.

A.4.1 Apical rotation

In the present study, counterclockwise rotation during LV ejection was demonstrated at the apical level in healthy individuals and was found in the dog model. During dobutamine infusion, there was an increase in apical rotation, and a tendency towards a decrease in time to peak rotation, whereas during LAD occlusion apical rotation was reduced. These changes in apical rotation by dobutamine and apical ischemia are concordant with the findings from previous studies that have used other methods (Rademakers et al., 1992; Buchalter et al., 1994; Gibbons Kroeker et al., 1995b,a; Dong et al., 1999).

Although systolic apical rotation was predominantly counterclockwise, there was a small, clockwise rotation during isovolumic contraction. The oppositely directed rotation was demonstrated by both sonomicrometry and STE but not by MRI (see Figs. A.5 and A.5). This phenomenon has been described previously and might be attributed to earlier activation of subendocardial fibers (right-handed helix) than subepicardial fibers (McDonald, 1970; Yun et al., 1991; Durrer et al., 1970; Azhari et al., 1992). The reason why this motion was not recognized by MRI tagging is probably the relatively low temporal resolution of the method (35 ms).

A.4.2 Basal rotation

Consistent with previous studies (Nagel et al., 2000; Sandstede et al., 2002; Fuchs et al., 2004; Fogel et al., 2000; Nagel et al., 2000; Setser et al., 2003; Lorenz et al., 2000; Moore et al., 2000; Nichols et al., 2002). LV rotation at the base was predominantly clockwise. During early systole, however, there was a counterclockwise rotation that gradually changed into a more substantial clockwise rotation during ejection. Dobutamine infusion caused a significant increase in basal clockwise rotation, with no change in time to peak rotation. To our knowledge, no previous studies exist of basal rotation during dobutamine infusion. Apical ischemia caused no significant change in basal rotation (Nagel et al., 2000), reflecting the fact that there was no impairment of LV function between equator and base.

Some studies have indicated that basal LV rotation is minimal (Gibbons Kroeker et al., 1993; Knudtson et al., 1997). However, in patients with aortic stenosis, a reduced magnitude of basal rotation compared with normals has been observed (Nagel et al., 2000). Furthermore, in patients with chronic heart failure, 6 months of treatment was associated with an increase in basal rotation, whereas apical rotation was unchanged (Fuchs et al., 2004), indicating that measurement of basal rotation may be clinically relevant. However, compared with the reference methods, assessment of rotation by STE was less accurate for the basal level than for the apical level. Therefore, deviations

in basal rotation could be difficult to assess by STE, and larger clinical studies will need to be performed to answer this question.

A.4.3 Comparison with previous studies

The magnitudes of LV apical and basal rotation and torsion, as reported in previous experimental and clinical studies, differ substantially (Rademakers et al., 1992; Gibbons Kroeker et al., 1993; Moon et al., 1994; Hansen et al., 1991; Yun et al., 1991; Buchalter et al., 1994; DeAnda et al., 1995; Knudtson et al., 1997; Stuber et al., 1999; Nagel et al., 2000; Sandstede et al., 2002; Fuchs et al., 2004; Tibayan et al., 2004; Buchalter et al., 1990; Nagel et al., 2000; Henson et al., 2000; Lorenz et al., 2000; Moore et al., 2000; Nichols et al., 2002; Dong et al., 1999; Mirro et al., 1979; Hansen et al., 1988; MacGowan et al., 1996; Rothfeld et al., 1998; Stuber et al., 1998; Bell et al., 2000; Tibayan et al., 2002; Sorger et al., 2003), and a number of factors may explain this variance.

As demonstrated by Henson et al. (2000), apparent differences in torsion between mice and humans are due to the different sizes of their ventricles. When systolic torsion angle was normalized for LV length, torsion was essentially similar in the two species. Furthermore, because torsion angle is a nonlinear function of ventricular length, its magnitude depends critically on measurement level relative to the LV base or other reference point. The relatively high values of apical rotation measured by Gibbons Kroeker et al. (1993) are most likely explained by their measurement technique, which recorded rotation at the distal part of the LV apex.

Another factor that may explain some of the variance in torsion magnitude in different studies is the existence of a marked transmural gradient, with subendocardial values almost twice the subepicardial (Buchalter et al., 1990). In the dog model, we measured subepicardial rotation, and during baseline conditions, torsion was approximately 6°. These values are in the same range as reported by Buchalter et al. (1994), who measured both subepicardial and subendocardial torsion in anesthetized dogs by MRI tagging. Furthermore, the hemodynamic and contractile status of the heart in different animal models may vary and give rise to differences in torsion. A significant reduction in rotation at the apical level and a trend toward a reduction at the base was found at the time of baseline recordings. This was associated with reductions in LV pressure and $LV\ dP/dt_{max}$, indicating that there was some reduction in LV systolic function. Most likely the decrease in rotation reflects impairment of LV function due to the extensive surgical instrumentation.

A.4.4 Limitations

Several important factors may influence the accuracy of STE. The quality of the recordings must be high to achieve correct tracking, and it requires proper adjustment of frame rate, probe frequency, and focus. In the present study, tracking quality was evaluated visually, and ROIs of poor tracking quality were either manually moved to areas of better speckle quality or deleted. Because rotational displacement is relatively homogenously distributed around the LV circumference in healthy myocardium,

deletion of one or a maximum of two ROIs will have minimal effect on the average rotation (Buchalter et al., 1994, 1990; Hansen et al., 1988).

A fundamental problem with STE in LV short-axis images is that longitudinal motion of the LV causes the myocardium to move in and out of the image plane. As a consequence, speckles generated from the ultrasound beam (2 to 3 *mm* of thickness) will represent the myocardium from different cross-sectional levels during the cardiac cycle. This problem is most pronounced at the LV base, where the longitudinal displacement according to our results, was approximately 4 *mm* from end-diastole to end-systole, whereas the LV apex was essentially stationary. In our study, the relation between STE and the reference methods was best at the apical level, probably because of the aforementioned phenomenon.

A limitation in the clinical study was that speckle quality in some cases was suboptimal in the subepicardial layer of the LV. Therefore, for validation against MRI, we compared measurements from the middle and inner wall layers. Hopefully, technical developments in ultrasound technology will resolve this problem. In the dog study, we had direct access to the heart via sternotomy, and by using ultrasound gel as a standoff, we obtained satisfactory tracking quality in all layers of the LV wall. One limitation of clinical routine use of STE is the selection of reproducible anatomic landmarks for measuring apical rotation. One approach was to move the cross-sectional image plane as far distally as possible. Another approach could be to measure at the most distal level that does not have luminal closure during systole. At the basal level, reproducible image planes were easier to obtain with the fibrous mitral ring for orientation. Selection of imaging plane is a challenge, and clinical testing of STE in patients is needed to determine whether reproducible measures can be obtained from ventricles that may change in size and geometry over time.

In contrast to STE, which provides a measure relative to a stationary reference point outside the heart (the echocardiographic transducer), sonomicrometry provides no direct measure of rotation. Because apical and basal rotations are in opposite directions, somewhere between them there exists a level where rotation changes from one direction to the other. A number of studies on dogs, mice and humans have confirmed that the short-axis level approximately one third from base to apex (LV equator) shows minimal rotation (Nagel et al., 2000; Sandstede et al., 2002; Fogel et al., 2000; Henson et al., 2000; Lorenz et al., 2000; Moore et al., 2000; Nichols et al., 2002). In our study, we measured rotation at the equatorial level by the time of crystal implantation, and the results confirmed minimal rotation ($-0.2 \pm 2.3^{\circ}$). Taking into account the good relationship between STE and sonomicrometry, this finding indicates that our methodological approach was adequate. Furthermore, for strict methodological comparison of STE with sonomicrometry, assessment of LV torsion was sufficient, and the correlation and agreement between torsion by the two methods were very good.

A.5 Conclusions

This study demonstrates that the magnitude, timing and dynamics of regional LV rotation and torsion can be measured accurately by STE. When MRI and sonomicrometry were used as reference methods, STE showed good correlation and agreement, suggesting that STE has the potential to become a fast and accurate noninvasive clinical tool.

A.6 Acknowledgements

Thomas Helle-Valle and Erik Lyseggen were recipients of clinical research fellowships from the Norwegian Council of Cardiovascular Diseases. Jonas Crosby and Brage H. Amundsen received clinical research fellowships from the Norwegian Research Council. We thank Drs Trond Vartdal, Eirik Pettersen and Anders Opdahl for beneficial collaboration in the laboratory, and MSc Eldrid Winther-Larssen and engineer Roger Odegaard for technical assistance.

References

Azhari, H., M. Buchalter, S. Sideman, E. Shapiro, and R. Beyar (1992). A conical model to describe the nonuniformity of the left ventricular twisting motion. *Ann. Biomed. Eng. 20*, 149–165.

Bell, S., L. Nyland, M. Tischler, M. McNabb, H. Granzier, and M. LeWinter (2000). Alterations in the determinants of diastolic suction during pacing tachycardia. *Circ. Res. 87*, 235–240.

Bland, J. and D. Altman (1986). Statistical methods for assessing agreement between two methods of clinical measurement. *Lancet 1*, 307–310.

Bohs, L. and G. Trahey (1991). A novel method for angle independent ultrasonic imaging of blood flow and tissue motion. *IEEE Trans. Biomed. Eng. 38*, 280–286.

Buchalter, M., F. Rademakers, J. Weiss, W. Rogers, M. Weisfeldt, and E. Shapiro (1994). Rotational deformation of the canine left ventricle measured by magnetic resonance tagging: effects of catecholamines, ischaemia, and pacing. *Cardiovasc. Res. 28*, 629–635.

Buchalter, M. B., J. L. Weiss, W. J. Rogers, E. A. Zerhouni, M. L. Weisfeldt, R. Beyar, and E. P. Shapiro (1990). Noninvasive quantification of left ventricular rotational deformation in normal humans using magnetic resonance imaging myocardial tagging. *Circulation 81*, 1236–1244.

DeAnda, A., M. Komeda, S. Nikolic, G. Daughters, N. Ingels, and D. Miller (1995). Left ventricular function, twist, and recoil after mitral valve replacement. *Circulation 92*, 458–466.

Dong, S., P. Hees, W. Huang, S. Buffer, J. Weiss, and E. Shapiro (1999). Independent effects of preload, afterload, and contractility on left ventricular torsion. *Am. J. Physiol. Heart Circ. Physiol. 277*, H1053–H1060.

Durrer, D., R. van Dam, G. Freud, M. Janse, F. Meijler, and R. Arzbaecher (1970). Total excitation of the isolated human heart. *Circulation 41*, 899–912.

Fogel, M., P. Weinberg, A. Hubbard, and J. Haselgrove (2000). Diastolic biomechanics in normal infants utilizing MRI tissue tagging. *Circulation 102*, 218–224.

Fuchs, E., M. Müller, H. Oswald, H. Thöny, P. Mohacsi, and O. Hess (2004). Cardiac rotation and relaxation in patients with chronic heart failure. *Eur. J. Heart Fail. 6*, 715–722.

Garot, J., D. Bluemke, N. Osman, C. Rochitte, E. McVeigh, E. Zerhouni, J. Prince, and J. Lima (2000). Fast determination of regional myocardial strain fields from tagged cardiac images using harmonic phase MRI. *Circulation 101*, 981–988.

Gibbons Kroeker, C., H. T. Keurs, M. Knudtson, J. Tyberg, and R. Beyar (1993). An optical device to measure the dynamics of apex rotation of the left ventricle. *Am. J. Physiol. Heart Circ. Physiol. 265*, H1444–H1449.

Gibbons Kroeker, C., J. Tyberg, and R. Beyar (1995a). Effects of ischemia on left ventricular apex rotation : An experimental study in anesthetized dogs. *Circulation 92*, 3539–3548.

Gibbons Kroeker, C., J. Tyberg, and R. Beyar (1995b). Effects of load manipulations, heart rate, and contractility on left ventricular apical rotation. an experimental study in anesthetized dogs. *Circulation 92*, 130–141.

Hansen, D., G. Daughters, E. Alderman, N. Ingels, and D. Miller (1988). Torsional deformation of the left ventricular midwall in human hearts with intramyocardial markers: regional heterogeneity and sensitivity to the inotropic effects of abrupt rate changes. *Circ. Res. 62*, 941–952.

Hansen, D., G. Daughters, E. Alderman, N. Ingels, E. Stinson, and D. Miller (1991). Effect of volume loading, pressure loading, and inotropic stimulation on left ventricular torsion in humans. *Circulation 83*, 1315–1326.

Henson, R., S. Song, J. Pastorek, J. Ackerman, and C. Lorenz (2000). Left ventricular torsion is equal in mice and humans. *Am. J. Physiol. Heart Circ. Physiol. 278*, H1117–H1123.

Knudtson, M., P. Galbraith, K. Hildebrand, J. Tyberg, and R. Beyar (1997). Dynamics of left ventricular apex rotation during angioplasty : A sensitive index of ischemic dysfunction. *Circulation 96*, 801–808.

Lorenz, C., J. Pastorek, and J. Bundy (2000). Delineation of normal human left ventricular twist throughout systole by tagged cine magnetic resonance imaging. *J. Cardiovasc. Magn. Reson. 2*, 97–108.

MacGowan, G., D. Burkhoff, W. Rogers, D. Salvador, H. Azhari, P. Hees, J. Zweier, H. Halperin, C. Siu, J. Lima, J. Weiss, and E. Shapiro (1996). Effects of afterload on regional left ventricular torsion. *Cardiovasc. Res. 31*, 917–925.

Maier, S. E., S. E. Fischer, G. C. McKinnon, O. M. Hess, H. P. Krayenbuehl, and P. Boesiger (1992). Evaluation of left ventricular segmental wall motion in hypertrophic cardiomyopathy with myocardial tagging. *Circulation 86*(6), 1919–1928.

McDonald, I. (1970). The shape and movements of the human left ventricle during systole. A study by cineangiography and by cineradiography of epicardial markers. *Am. J. Cardiol. 26*, 221–230.

Mirro, M., E. Rogers, A. Weyman, and H. Feigenbaum (1979). Angular displacement of the papillary-muscles during the cardiac cycle. *Circulation 60*, 327–333.

Moon, M., N. Ingels, G. Daughters, E. Stinson, D. Hansen, and D. Miller (1994). Alterations in left ventricular twist mechanics with inotropic stimulation and volume loading in human subjects. *Circulation 89*, 142–150.

Moore, C., C. Lugo-Olivieri, E. McVeigh, and E. Zerhouni (2000). Three-dimensional systolic strain patterns in the normal human left ventricle: Characterization with tagged MR imaging. *Radiology 214*, 453–466.

Nagel, E., M. Stuber, B. Burkhard, S. Fischer, M. Scheidegger, P. Boesiger, and O. Hess (2000). Cardiac rotation and relaxation in patients with aortic valve stenosis. *Eur. Heart J. 21*, 582–589.

Nagel, E., M. Stuber, M. Lakatos, M. Scheidegger, P. Boesiger, and O. Hess (2000). Cardiac rotation and relaxation after anterolateral myocardial infarction. *Coronary Art. Dis. 11*, 261–267.

Nichols, K., M. Kamran, C. Cooke, T. Faber, E. Garcia, S. Bergmann, and E. Depuey (2002). Feasibility of detecting cardiac torsion in myocardial perfusion gated SPECT data. *J. Nucl. Cardiol. 9*, 500–507.

Rademakers, F., M. Buchalter, W. Rogers, E. Zerhouni, M. Weisfeldt, J. Weiss, and E. Shapiro (1992). Dissociation between left ventricular untwisting and filling. accentuation by catecholamines. *Circulation 85*, 1572–1581.

Rothfeld, J., M. LeWinter, and M. Tischler (1998). Left ventricular systolic torsion and early diastolic filling by echocardiography in normal humans. *Am. J. Cardiol. 81*, 1465–1469.

Sandstede, J., T. Johnson, K. Harre, M. Beer, S. Hofmann, T. Pabst, W. Kenn, W. Voelker, S. Neubauer, and D. Hahn (2002). Cardiac systolic rotation and contraction before and after valve replacement for aortic stenosis: a myocardial tagging study using MR imaging. *Am. J. Roentgenol. 178*, 953–958.

Setser, R., J. Kasper, M. Lieber, R. Starling, P. McCarthy, and R. White (2003). Persistent abnormal left ventricular systolic torsion in dilated cardiomyopathy after partial left ventriculectomy. *J. Thorac. Cardiovasc. Surg. 126*, 48–55.

Sorger, J., B. Wyman, O. Faris, W. Hunter, and E. McVeigh (2003). Torsion of the left ventricle during pacing with MRI tagging. *J. Cardiovasc. Magn. Reson. 5*, 521–530.

Stuber, M., M. S. Y. S. Fischer, E. Nagel, F. Steinemann, O. Hess, and P. Boesiger (1999). Alterations in the local myocardial motion pattern in patients suffering from pressure overload due to aortic stenosis. *Circulation 100*, 361–368.

Stuber, M., E. Nagel, S. Fischer, M. Spiegel, M. Scheidegger, and P. Boesiger (1998). Quantification of the local heartwall motion by magnetic resonance myocardial tagging. *Comput. Med. Imaging Graph. 22*, 217–228.

Tibayan, F., K. Yun, J. Fann, D. Lai, T. Timek, G. Daughters, N. Ingels, and D. Miller (2002). Torsion dynamics in the evolution from acute to chronic mitral regurgitation. *J. Heart Valve Dis. 11*, 39–46.

Tibayan, F. A., F. Rodriguez, F. Langer, M. K. Zasio, L. Bailey, D. Liang, G. T. Daughters, N. B. J. Ingels, and D. C. Miller (2004). Alterations in left ventricular torsion and diastolic recoil after myocardial infarction with and without chronic ischemic mitral regurgitation. *Circulation 110*(11 Suppl 1), 109–114.

Yun, K., M. Niczyporuk, G. Daughters, N. Ingels, E. Stinson, E. Alderman, D. Hansen, and D. Miller (1991). Alterations in left ventricular diastolic twist mechanics during acute human cardiac allograft rejection. *Circulation 83*, 962–973.

Ultrasound Med. Biol., 2008 [available online]

Paper B

A new Tissue Doppler Method for Examination of Left Ventricular Rotation

Jonas Crosby*, Brage H. Amundsen*, Thomas Helle-Valle† and Per Arvid Steen‡ Hans Torp*
*) Department of Circulation and Medical Imaging, Faculty of Medicine, Norwegian University of Science and Technology, Trondheim, Norway
†) Institute for Surgical Research, Department of Cardiology, Rikshospitalet University Hospital, Oslo, Norway
‡) St. Olavs Hospital, Trondheim University Hospital, Trondheim, Norway

This paper introduces a new semi-automatic method for assessing regional left ventricular (LV) rotation that utilizes the velocity field provided by tissue Doppler imaging (TDI). LV end-systolic angle of twist estimated by the new method has been compared with rotation by magnetic resonance imaging (MRI) tagging, by 2D speckle tracking echocardiography (STE) and by a TDI method using the velocity difference between the tangential points on the LV circumference in 21 human subjects. The new TDI method gave lower absolute values for end-systolic twist angle than MRI and STE (agreement $-4.1 \pm 2.1^\circ$ and $-2.5 \pm 4.0^\circ$, respectively). The reproducibility of the new method was as good as for MRI and STE, but worse than the use of TDI velocities in tangential points. The present study has shown that TDI methods constitute useful alternatives to speckle tracking and MRI, and should be considered in future studies of LV twist and rotation.

The video clips cited in this article can be found online at http://www.umbjournal.org (doi:10.1016/j.ultrasmedbio.2008.03.022).

B.1 Introduction

During the cardiac cycle, the left ventricular (LV) myocardium rotates around its long axis. The rotation varies along the long axis, resulting in an angle of twist of the apex relative to the base. The pattern of rotation is observed to be stable over time in healthy subjects, but is sensitive to changes in both regional and global LV function (Hansen et al., 1991; Maier et al., 1992; Gibbons Kroeker et al., 1995; Tibayan et al., 2004; Helle-Valle et al., 2005; Takeuchi et al., 2007). Therefore, assessment of LV rotation has been suggested as an approach for quantifying LV function. Magnetic resonance imaging (MRI) tagging has predominantly been the method of choice to examine LV rotation and twist. Speckle tracking echocardiography (STE) on short axis (SAX) views has recently been introduced as an ultrasound-based method for assessing LV rotation (Notomi et al., 2005; Helle-Valle et al., 2005). Garot et al. (2002) suggested a method based on tissue Doppler imaging (TDI), where the rotation was found from the circumferential displacement of a region of the LV wall where the observed Doppler shift was zero. However, the physical foundation of this methodology has been questioned (D'hooge et al., 2002). A later paper by Notomi et al. (2005) presented a different TDI method in which the rotation was estimated using the velocities from the points of tangency between the LV wall and the ultrasound beams.

This paper presents a new complementary method for estimation of regional and global rotation from the velocity field provided by tissue Doppler imaging (TDI). The method is related to the method suggested by Notomi et al. (2005), but differs by making use of the velocity information in all visible parts of the LV wall, thereby allowing calculation of regional rotation and circumferential strain. LV rotation and twist angle measured by the new method (hereinafter referred to as TDI_1) are compared with results from the TDI-method suggested by Notomi et al., speckle tracking in B-mode images, and MRI tagging (referred to as the TDI_0, STE and MRI methods, respectively). We chose to study the methods in a mixed population of healthy subjects and patients with myocardial infarction.

B.2 LV rotation by TDI

B.2.1 Rotation from two tangential velocities (TDI_0)

LV rotation can be estimated by using four regions-of-interest (ROIs) in the TDI short-axis view: A lateral and a septal region, placed where the ultrasound beam is tangential to the LV circumference; and an anterior and posterior region, placed where the ultrasound beam is perpendicular to the LV circumference (Notomi et al., 2005). If the ROIs are adjusted to stay at their correct positions through the cardiac cycle, the LV rotation $\Theta(t)$ can be calculated by:

$$\Theta(t) = \int_0^t \frac{V_{Lat}(t) - V_{Sep}(t)}{2r(t)} dt \tag{B.1}$$

where V_{Lat}, V_{Sep} are myocardial velocities at lateral and septal regions, and $r(t)$ is the LV radius estimated by:

$$r(t) = r_0 + \int_0^t V_n(t) dt \tag{B.2}$$

where r_0 is the end-diastolic radius, and V_n is the contraction velocity found from the velocities V_{Pos} and V_{Ant} in the posterior and anterior regions:

$$V_n(t) = \left(V_{Pos}(t) - V_{Ant}(t)\right)/2 \tag{B.3}$$

B.2.2 The extended TDI method (TDI_1)

The main assumption in our algorithm is that the LV wall in short axis images is approximately circular, and remains circular through the cardiac cycle. Thereby, the local in-plane motion can be decomposed into a tangential motion (i.e. rotation) and a radial motion (i.e contraction or expansion), in addition to a global translation. The user input to the method is the LV center position in end-diastole, end-systole and mid-diastole, and the LV radius in end-diastole. To perform regional analysis, the orientation of the LV has to be indicated by the user. The lateral component of the translation of the LV center is found by interpolation between the user-drawn center, whereas the radial (i.e. in the beam direction) translation is estimated as the mean

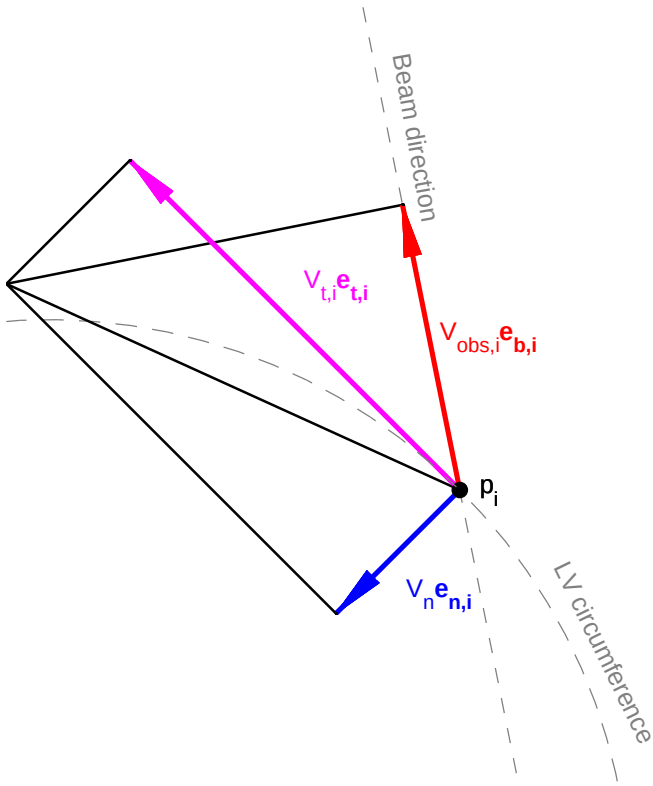

Figure B.1: Illustration of the velocity vectors involved in eqn B.4. For simplicity, the velocity $\vec{v_c}$ of the center point is omitted from the illustration.

of velocities V_{Pos} and V_{Ant} from posterior and anterior ROIs. The LV contraction velocity V_n is estimated from eqn B.3. The ROIs are adjusted automatically through the cardiac cycle, using the estimates of the center displacement and the contraction velocity. A set of points (sample volumes) are distributed on the resulting dynamic LV circumference. In each point, the local beam direction $\vec{e}_b$, normal direction $\vec{e}_n$ and tangential direction $\vec{e}_t$ are calculated. The tangential velocity $V_{t,i}$ is calculated from the observed Doppler velocity $V_{obs,i}$ in each point i as:

$$V_{t,i} = \frac{V_{obs,i} - (V_n \vec{e}_{n,i} + \vec{v}_c) \cdot \vec{e}_{b,i}}{\vec{e}_{t,i} \cdot \vec{e}_{b,i}} \tag{B.4}$$

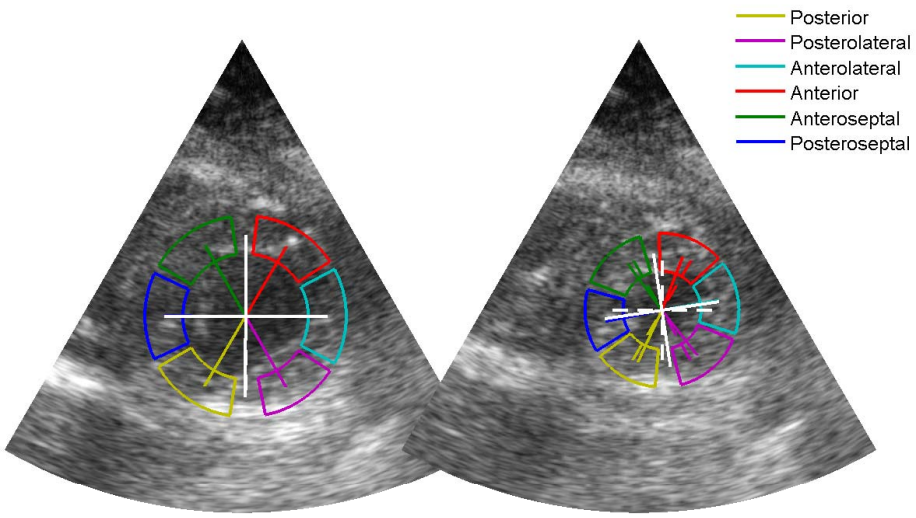

Figure B.2: Regional apical rotation in end-diastole (left) and end-systole (right), as estimated by the new TDI_1 method. The white cross indicates the average rotation of all segments.

where $\vec{v}_c$ is the center velocity vector. Rotation Θ_i is calculated as:

$$\Theta_i(t) = \int_0^t V_{t,i}(t)/r(t)dt \tag{B.5}$$

where $r(t) = r_0 + \int_0^t V_n(t)dt$ (Fig. B.1). If we assume $V_{Lat} = -V_{Sep}$ and no displacement of the LV center, eqn B.5 and B.4 equals eqn B.1 in the lateral and septal regions where the ultrasound beam is tangential to the circumference ($\vec{e_{b,i}} = \vec{e_{t,i}}$). Equation B.4 has a singularity when $\vec{e_{t,i}}$ is perpendicular to $\vec{e_{b,i}}$, and points on the LV circumference where $\vec{e_{n,i}}$ makes an angle with the beam direction less than a small threshold angle are therefore excluded from the analysis. The rotation traces are linearly drift-corrected in order to return to zero at the end of the cardiac cycle. Segmental rotation is calculated as the mean rotation from all circumferential points in each segment. The method was implemented in Matlab (The Mathworks, Massachusetts, version 7.0). Figure B.2 shows the method applied on a short-axis TDI recording.

B.3 Methods

B.3.1 Study sample

Twenty-one subjects, 10 with previous myocardial infarction (1 female, 9 male; age range 62±7 y) and 11 healthy volunteers (6 female, 5 male; age range 24±4 y), were included in the study after having given written informed consent. The study protocol was approved by the National Committee for Medical Research Ethics in Norway. The patient group consisted of seven subjects with inferior infarction, two with anterior infarction and one with multiple infarctions. The time between the infarction and the study examination was > 3 weeks. The time interval between MRI acquisition and echocardiography was less than 3 h in all but two subjects (< 24 h). The mixed population was chosen in order to examine the agreement of the algorithms in subjects with variable twist pattern and image quality, and no matching between the patients and the healthy subjects in terms of age, gender or BMI was performed.

B.3.2 Definitions

Two short-axis levels were defined: (ii) basal level: just distal to the left atrioventricular plane in end-systole; (ii) apical level: just proximal to the level with luminal closure at end-systole. Clockwise rotation, when viewed from the apex, is represented by positive numbers. Angle of twist is defined as the difference in rotation between the apical level and the basal level. Twist velocities were computed by numerical differentiation of the angle of twist traces, using a window size of 50 ms.

B.3.3 Echocardiography

TDI images (frame rate $135 \pm 39 s^{-1}$) and B-mode images (frame rate $96 \pm 22\ s^{-1}$) from the two short-axis levels were acquired with the subjects in the left lateral position using a Vivid 7 scanner with a 2.5-MHz transducer (GE Vingmed Ultrasound, Horten, Norway). Efforts were made to orient the short-axis views perpendicular to the long axis, by counteracting elliptical distortion of the LV. Images were stored digitally and analyzed off-line. End-systole was defined as the time of aortic valve closure. The timing of aortic valve closure in each subject was computed as the onset of the sharp velocity spike at end ejection in separate pulsed Doppler recordings from the LV outflow tract. Assessment of rotation from TDI images were performed using the extended TDI algorithm described in the previous section (TDI_1), as well as our own implementation of the method described by Notomi et al. (2005) (TDI_0). Both methods used an 8 mm circular ROI at the anterior and posterior regions. In the TDI_0 method, a 4×8 mm elliptical ROI was used for the lateral and septal regions. Different to the study of Notomi et al., no averaging over consecutive beats was performed. In the TDI_1 method, regional rotation was measured in 400 circumferential points, but the results were not used when the angle between $\vec{e}_{n,i}$ and the beam direction was less than 5°. Rotation analysis of the corresponding B-mode images (STE) was performed using the 2D strain tool for EchoPac (version 6.0.0, GE Healthcare), keeping the default values for temporal and spatial averaging. To compare the rotation values

from echocardiography with MRI, the reference time of zero rotation was adjusted to correspond to the second tagged MRI image after end-diastole, because in many cases the first MRI was corrupted by noise.

B.3.4 MRI tagging

Tagged short-axis MRI images from the two levels were recorded during breath holds with a 3-T whole-body magnet (Intera, Philips Medical Systems) and a six-channel SENSE cardiac coil, using a C-SPAMM tagging technique (Fischer et al., 1993). The following acquisition settings were applied: Tag spacing 8 mm, repetition time 24 ms, flip angle 20°, base resolution, 256 × 256 pixels. To reduce the effect of out-of-plane motion, the slice thickness was set to be higher at the base (20 mm) than at the apex (10 mm). Assessment of in-plane rotation was done by peak-combination HARP analysis (Ryf et al., 2004), provided by the tagging analysis software for the Philips PRIDE environment (TagTrack, version 1.5.4, GyroTools and Philips Medical Systems). Based on a manually drawn contour inside the LV myocardium, TagTrack interpolated a set of equally spaced points. The motion of these points was then automatically tracked by the software by using the phase information in the tagged MRI scan. Rotation was calculated from the angular displacement of the points relative to the center of mass.

B.3.5 Statistics

Agreement was evaluated by Bland-Altman statistics (Bland and Altman, 1999). End-systolic angle of twist values were compared by paired t-tests, and 95% limits of agreements were approximated as $mean \pm 2SD$ of the difference between the methods. A p-value less than 0.05 was considered statistically significant. Values are reported as $mean \pm SD$. Reproducibility analysis were performed based on the ten last examined subjects (four patients, six healthy), in which repeated MRI tagging recordings were performed. Reproducibility was reported as intraobserver (same cycle) and interobserver (different cycles, two separate acquisitions were made by MRI tagging) repeatability coefficients (Bland and Altman, 1999). Analyzes were performed using the Statistics Toolbox in Matlab.

B.4 Results

The summary of the main results is found in Table B.1. Video clips showing examples of tracking of rotational motion using the new TDI_1 method can be found in the online supplement. Figure B.3 and B.4 show examples of rotation and rotation velocity traces from the different methods for the basal, mid-ventricular and apical levels. Figure B.5 summarizes the development of the twist angle and twist velocity during the cardiac cycle in the healthy subjects. The timing of the traces is normalized in systole and diastole, separately.

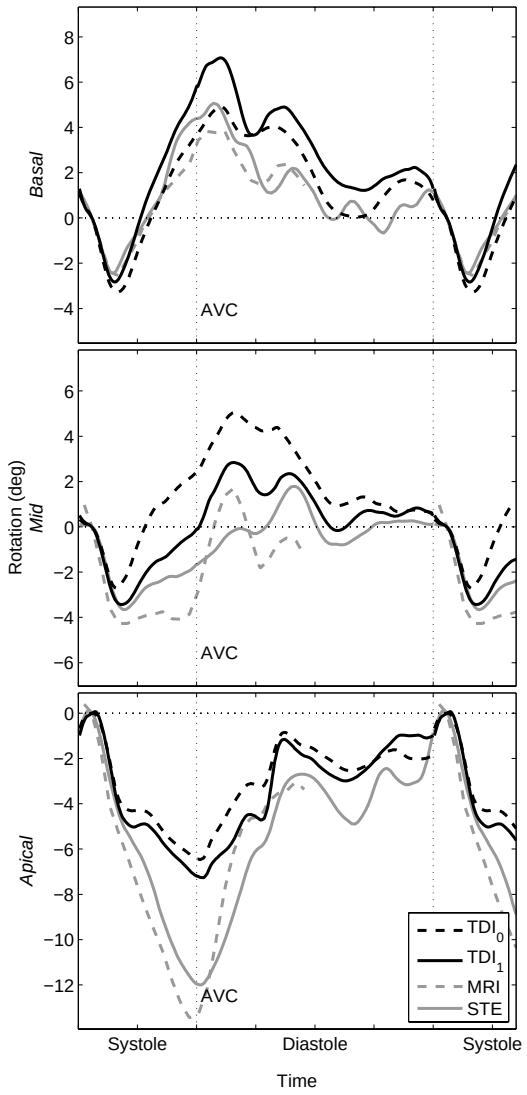

Figure B.3: Example of rotation traces from a healthy subject using the TDI methods (TDI_0 and TDI_1), B-mode speckle tracking (STE) and MRI HARP analysis (MRI) at basal, mid-ventricular and apical levels. Aortic valve closure (AVC) was estimated from Doppler flow profile.

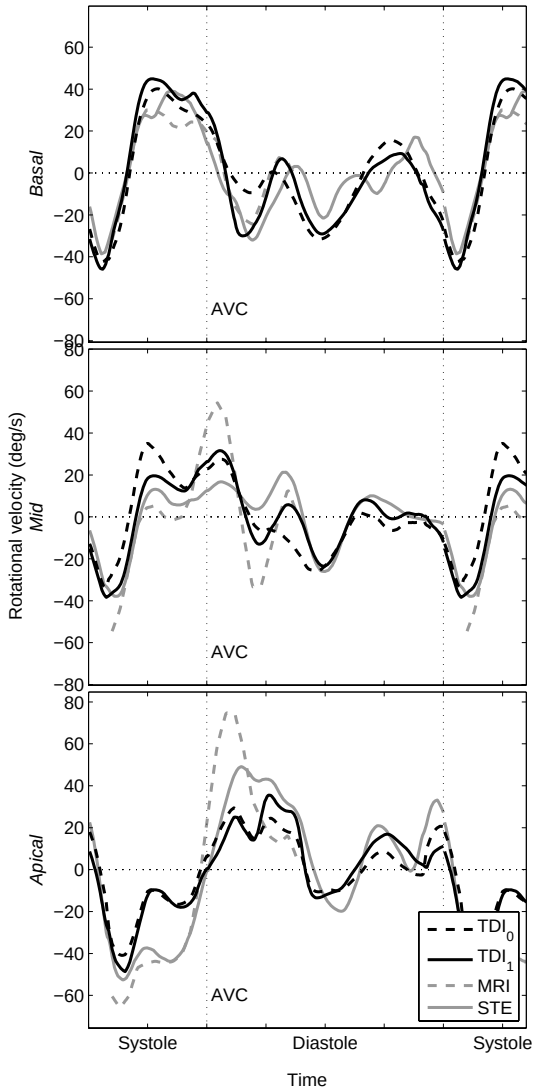

Figure B.4: Example of rotation velocity traces from a healthy subject using the TDI methods (TDI_0 and TDI_1), B-mode speckle tracking (STE) and MRI HARP analysis (MRI) at basal, mid-ventricular and apical levels. Aortic valve closure (AVC) was estimated from Doppler flow profile.

Table B.1: Summarization of methods for assessment of LV rotational motion.

Method:	MRI	TDI_0	TDI_1	STE
Regional rotation	Yes	No	Yes	Yes
Frame rate, (s^{-1})	42	135 ± 39	135 ± 39	96 ± 22
End-systolic twist, $(^\circ)$	-14.5 ± 3.4	-9.0 ± 3.8	-10.8 ± 4.6	-13.5 ± 5.3
- Agreement w/TDI_0	-5.2 ± 3.2	N/A	-1.8 ± 4.5	-4.3 ± 3.2
- Agreement w/TDI_1	-4.1 ± 2.1	1.8 ± 4.5	N/A	-2.5 ± 4.0
- Rep. coeff. —Intraobs	3.7	3.0	4.0	5.8
- Rep. coeff. —Interobs	5.6	3.4	3.9	5.6

N/A = Not applicable; Rep. coeff = repeatability coefficient; Intraobs = intraobserver; Interobs = interobserver.

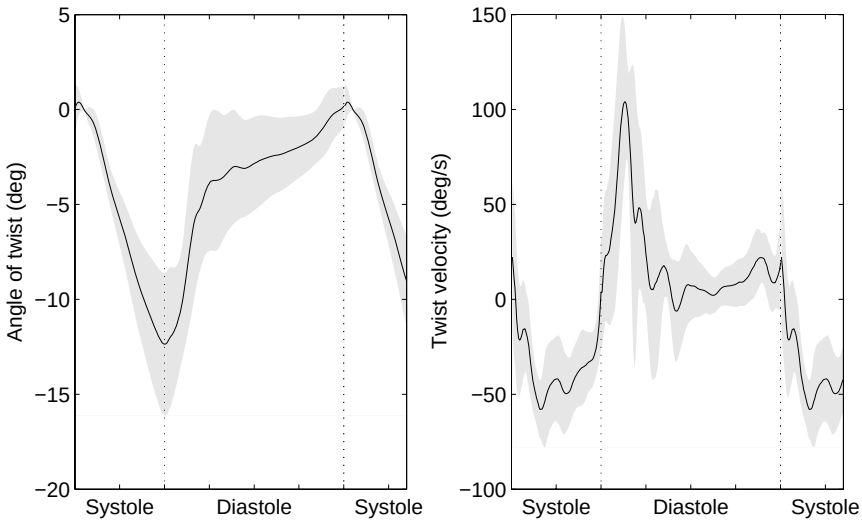

Figure B.5: Left ventricular twist angle and twist velocity using the TDI_1 method, averaged over 11 healthy subjects. The shaded areas indicate $\pm 1SD$.

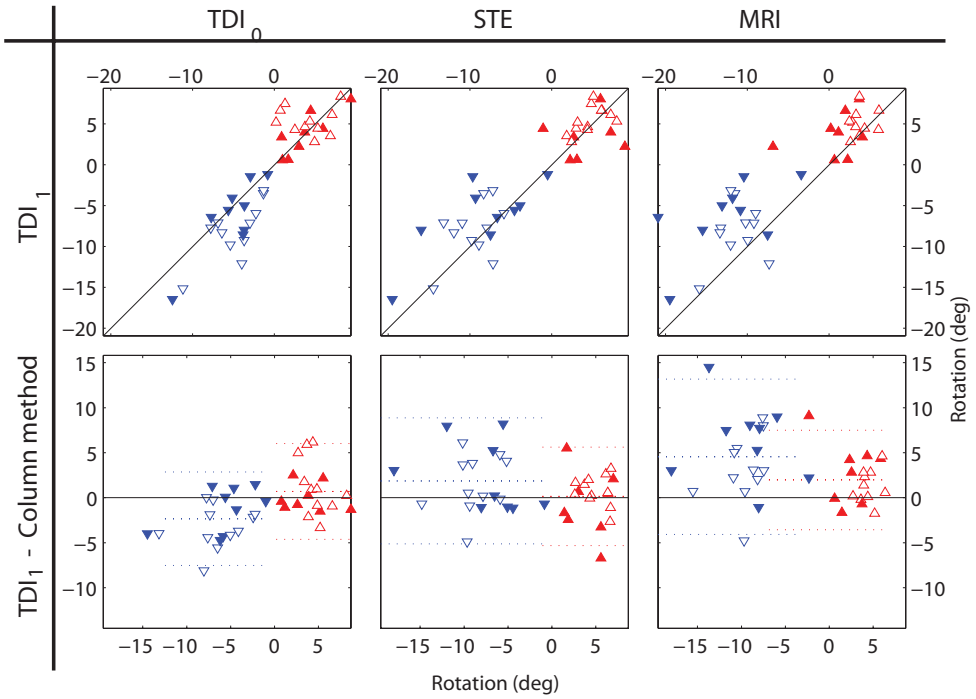

Figure B.6: Agreement between the methods for assessment of end-systolic left ventricular rotation at basal (△) and apical (▽) levels. Solid symbols indicate patients and open symbols indicate normal subjects. Upper row: Scatter plots with lines of identity. The column method is on the ordinate axis and the TDI_1 method is on the abscissa. Lower row: Agreement shown as Bland-Altman plots, with the $bias \pm 2SD$ for each level indicated as dashed lines. The difference on the ordinate axis is calculated as TDI_1 *method - column method*. The abscissa shows the mean of TDI_1 and column method.

B.4.1 Agreement

One patient was excluded because the B-mode image quality was too low to define the borders of the myocardial wall with the ultrasound methods. In the TDI methods, one additional basal level was excluded because of large translation of the left ventricle during the cardiac cycle. One basal level from MRI was accidentally lost during exportation of data from the MRI scanner. Figure B.6 shows the agreement of basal and apical rotation between TDI_1 and the other methods. The figure shows that the new TDI_1 method reports significant higher absolute end-systolic rotation than the TDI_0 method for the apical level, but still significantly lower absolute values than found by speckle tracking and MRI. For the basal level, there is no significant bias except when compared with MRI.

Figure B.7 shows the agreement between methods in assessment of the twist angle

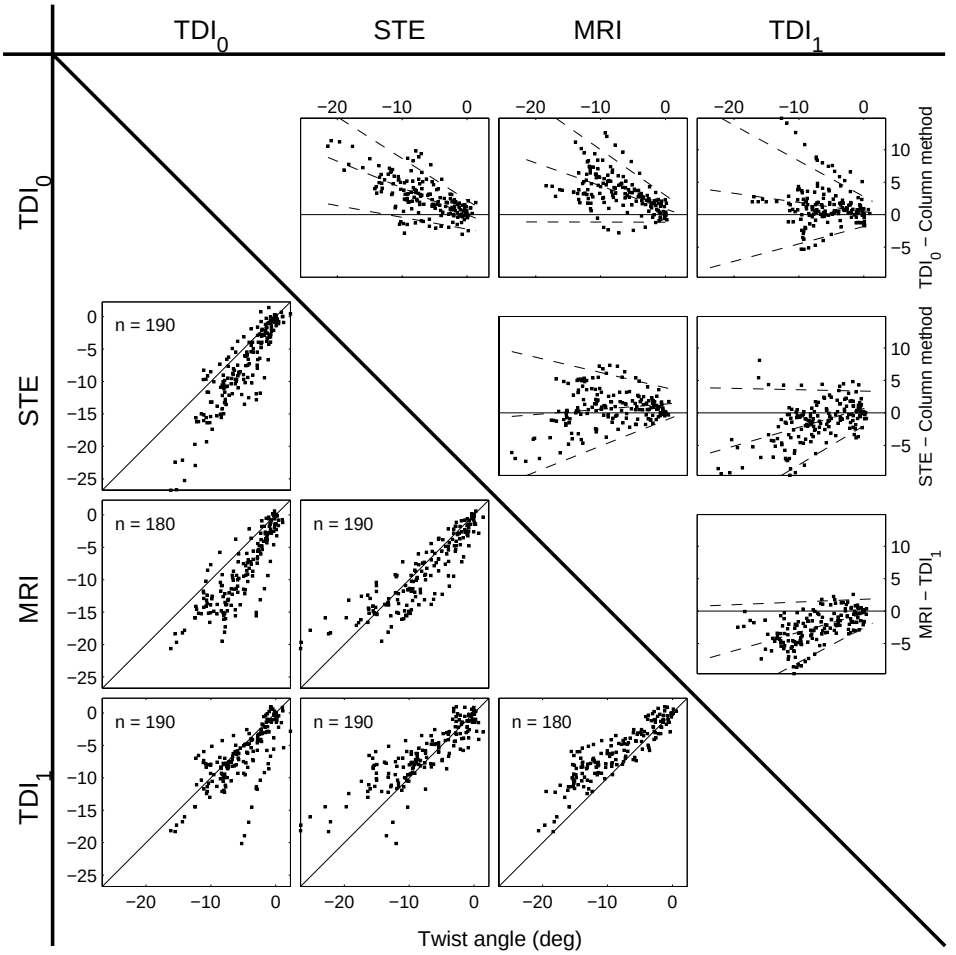

Figure B.7: Agreement between the methods for assessment of left ventricular angle of twist in ten normalized time points in systole. Upper right triangle: Agreement shown as Bland-Altman plots, with bias and 95% limits of agreement indicated as dashed lines. The difference on the ordinate axis is calculated as *row method - column method*. The abscissa shows the mean of the row and column method. Lower left triangle: Scatter plots with lines of identity. The column method is on the abscissa and the row method is on the ordinate axis.

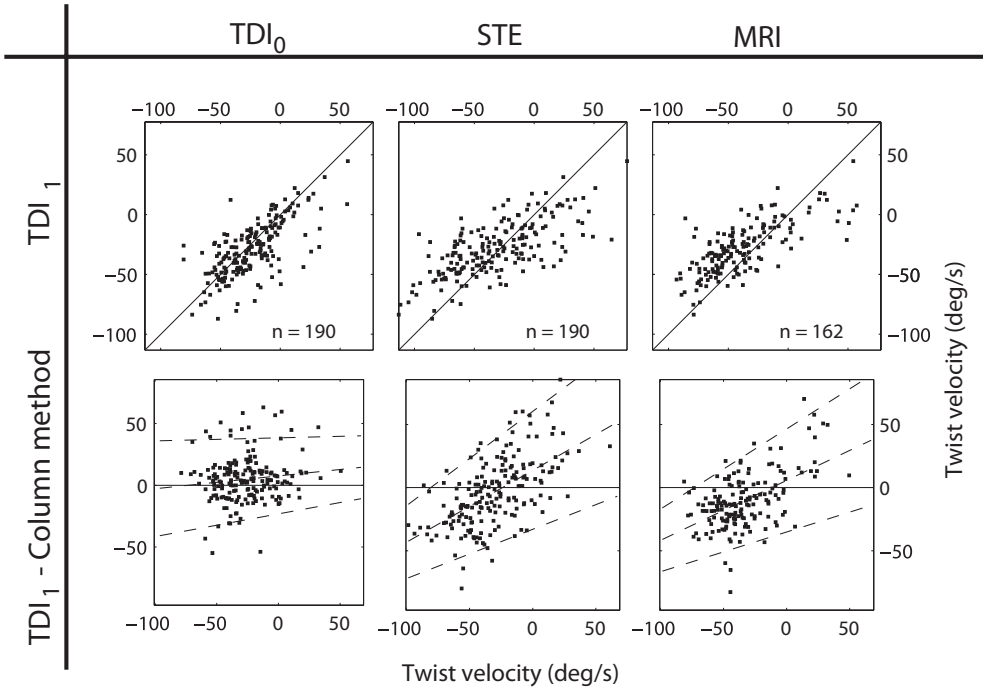

Figure B.8: Agreement between the methods for assessment of left ventricular twist velocity in ten normalized time points in systole. Upper row: Scatter plots with lines of identity. The column method is on the ordinate axis and the TDI_1 method is on the abscissa. Lower row: Agreement shown as Bland-Altman plots, with bias and 95% limits of agreement indicated as dashed lines. The difference on the ordinate axis is calculated as TDI_1 *method - column method*. The abscissa shows the mean of the TDI_1 and column method.

in ten normalized time points in systole for the mixed population of patients and healthy subjects. The Bland-Altman plots demonstrate clear relationships between the differences and the mean, as well as between the standard deviations and the mean. The limits of agreement are therefore estimated using the regression approach suggested by Bland and Altman (1999). Analysis of the end-systolic values showed a significant underestimation of the absolute twist values in both TDI methods compared with MRI (agreement $5.2 \pm 3.2°$ for TDI_0; $4.1 \pm 2.1°$ for TDI_1) and speckle tracking ($4.3 \pm 3.2°$ for TDI_0; $2.5 \pm 4.0°$ for TDI_1). The agreement in estimated end-systolic twist between TDI_0 and TDI_1 was $1.8 \pm 4.5°$.

Figure B.8 shows the agreement between methods in assessment of the twist velocity in the same normalized time points in systole, estimated using a 50-ms window.

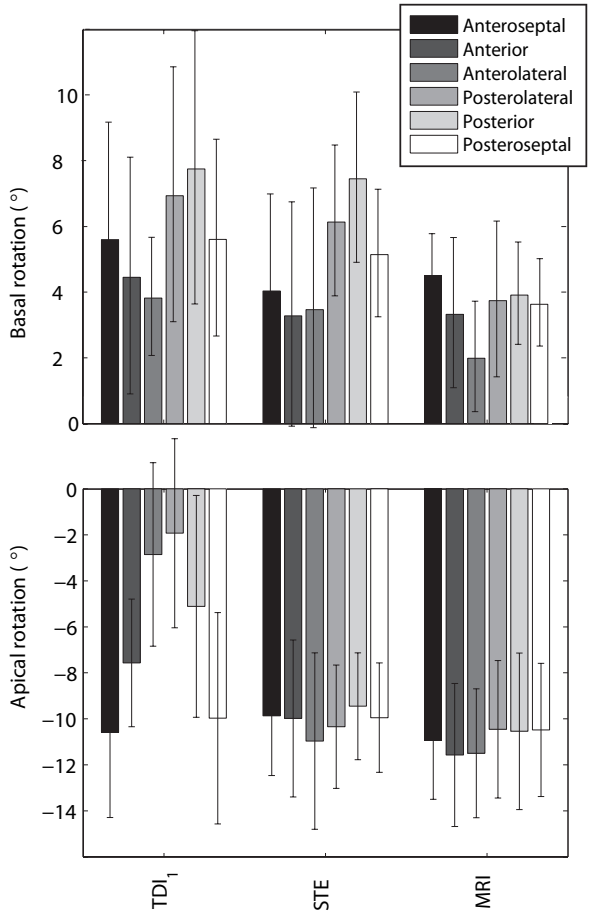

Figure B.9: Basal and apical end-systolic rotation in six circumferential segments; average of 11 healthy subjects. Error bars indicate the standard deviation. TDI_0 is not included in the figure as it does not permit calculations of regional rotation values.

B.4.2 Regional rotation

The investigation of circumferential variations in rotation revealed a near sinusoidal-shaped segmental variation of average basal end-systolic rotation in healthy subjects (Fig. B.9), as well as in patients (not shown). The highest values were found near the anterolateral wall. A similar sinusoidal distribution of rotation could also be seen at the apical level, but with a larger variation between the methods.

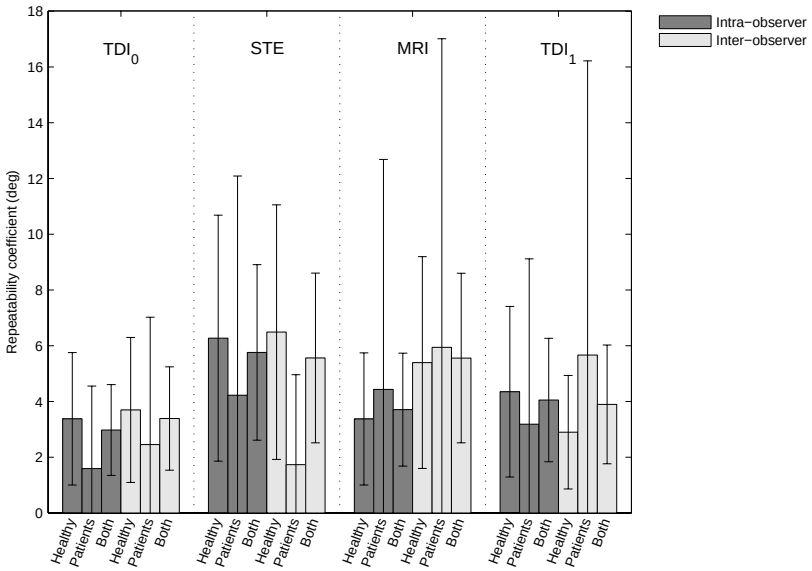

Figure B.10: Repeatability coefficients for end-systolic twist angle for the four methods for patients and healthy subjects. The error bars show the 95% confidence intervals of the repeatability coefficient estimate.

B.4.3 Reproducibility

Three (two patients, one healthy) of the ten included subjects were excluded from the reproducibility analysis because of incomplete data in some of the imaging modalities. Repeatability coefficients for end-systolic twist angle are shown in Figure B.10. The lowest repeatability coefficients were associated with the TDI_0 method, but the differences between the methods were not found to be statistically significant. Reproducibility for basal and apical end-systolic rotation (separate values not shown) was better than for end-systolic twist angle, especially the basal level where the intraobserver repeatability coefficients were 1.5°, 1.2°, 2.2° and 3.4° for MRI, TDI_0, TDI_1 and STE, respectively. Separate analysis of patients and normal subjects revealed no significant differences in the reproducibility of end-systolic twist between the two groups.

B.5 Discussion

B.5.1 Agreement

The rotation and twist patterns for healthy subjects by the new TDI method presented in this study (see Figs. B.3 and B.5) are similar to what has been reported earlier: the counterclockwise rotation in early systole at the basal level is followed by a larger clockwise rotation. At the apical level, the counterclockwise rotation continues through the whole systole, and is not inverted until the beginning of diastole. This results in a monotonically decreasing twist angle in the systole, which is followed by a rapid untwist in early systole. As illustrated in Fig. B.5, the twist pattern was quite homogeneous in our group of healthy volunteers.

Figure B.7 indicates a linear relationship between the twist estimates from the different methods, but that the factor of proportionality varies between the subjects. Overall, the TDI methods measured lower absolute twist angles than MRI and STE. The same trend was reported for peak systolic twist by Notomi et al. (2005) for TDI_0 versus MRI, but with a much lower bias (0.35°). The disagreement is because of lower measured absolute rotation at the apical level, as is evident in Fig. B.6. The lower panel in Fig. B.3 shows how the TDI methods typically cut down on the negative peak measured by the two other methods. A reason for this disagreement might be the discrepancies in the ROIs, caused by (i) differences in the initial contours, due to poor wall definition; (ii) misalignment of the imaging planes; (iii) differences in ROI size between the methods; and (iv) drifting caused by the tracking. Because the rotation in the LV is known to vary both longitudinally and transmurally, these discrepancies in ROIs might cause errors in the rotation estimate. A previous study by Buchalter et al. (1990) reported a twist angle of the endocardium that was about twice that of the epicardium. In the longitudinal direction, values from Buchalter et al. (1990) and Kim et al. (2007) indicate an average torsion of $3.0°/cm$ and $3.4°/cm$, respectively.

The wide limits of agreement seen in Fig. B.6 are consistent with the high repeatability coefficients associated with the methods. At both basal and apical levels the differences between the TDI_1 method and the three other methods are very large in some subjects compared with the range of rotation values. On average, the rotation values from the new TDI_1 method lie between the results from the TDI_1 method and speckle tracking method. The agreement with MRI was worse than with the two echo methods, possible because of misalignment of the imaging planes and the time lapse between the data acquisitions.

In the comparison with STE and MRI, the patients are overrepresented among the subjects with the highest underestimation for the TDI_1 method. This was probably caused by lower image quality in the patients than in the young healthy volunteers. This trend is not seen in the comparison with the TDI_0, where the distribution of the difference is quite similar for the two groups. The high basal bias seen in the comparison with MRI is highly affected by the difference in one subject, which might be considered as an outlier. As expected, the average absolute apical rotation in the patient group was lower than in the normal group, although Fig B.6 reveals that some patients had high apical rotation. The patients included in this study had infarctions of

different localizations and extents, which is reflected in a much wider range of values for end-systolic rotation than for the healthy subjects. In the interpretation of the differences between patients and healthy subjects in this study it should be kept in mind that differences in demographic variables, such as for example age (Takeuchi et al., 2006), would affect the rotation in addition to the myocardial infarction. Separation of these factors falls beyond the scope of this method comparison study. The differences in Fig B.6 show a similar dependence on the mean for the patients and the healthy subjects.

The Harp analysis in MRI, the speckle tracking of B-mode images and the Doppler methods are affected by out-of-plane motion caused by the shortening of the LV. This effect is most pronounced at the base, where the out-of-plane-motion often exceeds 10 millimeters in healthy subjects. The large MRI slice thickness (1 to 2 cm) that was used to handle this motion results in a longitudinal averaging of the rotation measurements that could affect the rotation values, especially when the rotation is known to increase non-linearly from the base to the apex (Young et al., 1994). The difference in slice thickness between MRI and ultrasound could be minimized by defocusing the ultrasound beam, but this would lead to more decorrelation and reduce the sensitivity of the ultrasound methods. The fundamental differences in image acquisition are also preventing absolute coincidence between the motion measured by tagged MRI and the motion measured by 2D echocardiography: The tag lines tracked by the MRI method is actually the intersections between a set of deformed out-of-plane tag planes and the imaging plane, whereas the ultrasound methods have no similar reference to the out-of-plane configuration of the LV in the first frame. Direct comparison between rotation values measured by MRI and echocardiography would be possible, however, when the displacements of material points are found by 3D speckle tracking in ultrasound volume data and by 3D tagging (Ryf et al., 2002). Unfortunately, an analogous extension of the TDI method is not possible.

The effect of errors in the calculation of the tangential velocity estimate $V_{t,i}$ in eqn B.4 is highly dependent on the angle $\theta_{tb,i}$ between the ultrasound beam direction $\vec{e_{b,i}}$ and the tangent to the LV circumference $\vec{e_{t,i}}$. An error $\Delta V_{b,i}$ in the Doppler velocity and an error ΔV_n in the contraction velocity will affect the estimated $V_{t,i}$ according to the following equation:

$$\Delta V_{t,i} = \Delta V_n tan(\theta_{tb,i}) + \Delta V_{b,i} sec(\theta_{tb,i}) \tag{B.6}$$

An error in V_n is the most likely because it is not measured locally. Errors in the assumption of a circular LV will cause V_n to vary along the LV circumference, giving an error $V_{n,i}$ that is amplified in the parts of the LV where the angle between the beam and the LV circumference is large. An inherent weakness in the TDI methods is the inability to use the velocity data to estimate the lateral component of the translation of the LV center. In this study this translation is found by interpolation between user-drawn points, which could induce errors both in the placement of the ROIs and in the center velocity V_c in eqn B.4.

It could be argued that the agreement in this study could have been improved by a stricter selection of levels used for analysis. In a recent study, Kim et al. (2007) found only 35% of 160 healthy volunteers feasible for estimation of torsion by STE

by using a few rules of thumb regarding how the rotation traces should look like but, because there was no reference method, it is not known whether this approach really would improve the agreement. The degree of drift of the tracked points during one cardiac cycle is often used as a threshold value for feasibility. However, the drift error often arises after the rapid changes in end-systole and does not necessarily reflect the tracking error in systole. For the STE method, visual evaluation of the quality of the B-mode images and the apparent accuracy of the tracking of myocardial points could give an indication of the feasibility for assessment of rotation. Conversely, for the TDI methods, the evaluation of feasibility of rotation estimates based on image quality and tracking quality is more difficult.

B.5.2 Regional rotation

The measured regional rotation angles are highly dependent on the estimate of the center point (Young et al., 1994). A displacement Δx of the center point would induce a maximal segmental variation of rotation $\Delta\Theta$:

$$\Delta\Theta = \pm tan^{-1}\left(\frac{\Delta x}{r}\right) \tag{B.7}$$

For instance, a deviation of the center position equal to a twentieth part of the radius would in theory cause a maximal regional difference of 5.7° between the segments perpendicular to the vector of displacement. This could explain the sinusoidal shape of segmental basal end-systolic rotation seen in Fig. B.9, which would probably disappear if the average center point is moved slightly in the direction of the anteroseptal wall. The global rotation on the other hand, is quite robust for small deviations in the center estimate because of symmetry of the error. This observation, together with the large variability in the methods, limits the value of regional rotation and twist angle as clinical parameters. On the other hand, estimation of global rotation has to be averaged over several segments in order to reduce errors because of deviations in the center estimate.

B.5.3 Reproducibility

There were no significant difference between the intra- and interobserver repeatability coefficients for any of the methods in this study. This can probably be explained by the low number of subjects and the large degree of automation. The lowest repeatability coefficients were associated with the TDI_0 method, but the differences between the methods were not found to be statistically significant. The high repeatability coefficients relative to the mean values are somehow surprising, considering the degree of automation in the methods, and can indicate that the methods are sensitive to small deviations in the user interaction. The reproducibility was much better at the basal level than at the apical. The small LV radius and the complex deformation at the apical level imply that the angular estimates at this level are particularly sensitive to small deviations in the initialization. In addition, the apical echocardiographic images

had overall lower image quality, and the coarse *trabeculae carneae* near the apex often makes it difficult to define a unique center point and radius.

The analysis revealed no difference between normal subjects and patients in terms of reproducibility. It would be expected that the lower image quality from the patients would cause higher variance in the placement of the initial contours, but on the other hand, the lower absolute rotation in the patients are likely to give less variation in rotation values due to the dependence of the mean.

B.5.4 Limitations

The relation between the difference and the mean for the agreement between many of the methods in this study, and the shifted reference time point of rotation and twist, should be taken into consideration when comparing the results with other studies. None of the subjects in this study had severely deformed ventricles, and it is expected that the TDI methods would produce erroneous rotation values in such cases as the assumption of an approximately circular LV would be invalid. The separate repeatability coefficients for patients and healthy subjects were based on very small populations.

B.6 Conclusions

A new method for estimation of LV rotational motion from TDI has been developed. Compared with MRI and STE, the new TDI method gave lower absolute values for end-systolic twist angle (agreement $-4.1 \pm 2.1°$ and $-2.5 \pm 4.20°$, respectively). The lower agreement was found at the apical level. The interobserver repeatability coefficient was 3.9°, not significantly different than for MRI (5.6°), STE (5.6°), or the use of TDI velocities in tangential points (3.4°).

The agreement and reproducibility of the new method were found to be better for basal rotation than for apical rotation and twist. The high temporal resolution and the possibility of detecting regional variations makes the new extended TDI method a useful supplement to speckle tracking and MRI for investigation of the twisting behavior of the LV.

B.7 Acknowledgements

We appreciate the technical assistance of Jørn Kvœrness (Philips Medical Systems) with the MRI tagging measurements.

References

Bland, J. M. and D. G. Altman (1999). Measuring agreement in method comparison studies. *Stat. Methods. Med. Res. 8*(2), 135–160.

Buchalter, M. B., J. L. Weiss, W. J. Rogers, E. A. Zerhouni, M. L. Weisfeldt, R. Beyar, and E. P. Shapiro (1990). Noninvasive quantification of left ventricular rotational deformation in normal humans using magnetic resonance imaging myocardial tagging. *Circulation 81*, 1236–1244.

D'hooge, J., P. Claus, and J. Separovic (2002). Alterations of systolic left ventricular twist after acute myocardial infarction. *Am. J. Physiol. Heart Circ. Physiol. 283*, H2733–H2734.

Fischer, S. E., G. C. McKinnon, S. E. Maier, and P. Boesiger (1993). Improved myocardial tagging contrast. *Magn. Reson. Med. 30*(2), 191–200.

Garot, J., O. Pascal, B. Diebold, G. Derumeaux, B. Gerber, J. Dubois-Rande, J. Lima, and P. Gueret (2002). Alterations of systolic left ventricular twist after acute myocardial infarction. *Am. J. Physiol. Heart Circ. Physiol. 282*, H357–H362.

Gibbons Kroeker, C., J. Tyberg, and R. Beyar (1995). Effects of load manipulations, heart rate, and contractility on left ventricular apical rotation. an experimental study in anesthetized dogs. *Circulation 92*, 130–141.

Hansen, D., G. Daughters, E. Alderman, N. Ingels, E. Stinson, and D. Miller (1991). Effect of volume loading, pressure loading, and inotropic stimulation on left ventricular torsion in humans. *Circulation 83*, 1315–1326.

Helle-Valle, T., J. Crosby, T. Edvardsen, E. Lyseggen, B. Amundsen, H. Smith, B. Rosen, J. Lima, H. Torp, H. Ihlen, and O. Smiseth (2005). New noninvasive method for assessment of left ventricular rotation: speckle tracking echocardiography. *Circulation 112*, 3149–3156.

Kim, H.-K., D.-W. Sohn, S.-E. Lee, S.-Y. Choi, J.-S. Park, Y.-J. Kim, B.-H. Oh, Y.-B. Park, and Y.-S. Choi (2007). Assessment of left ventricular rotation and torsion with two-dimensional speckle tracking echocardiography. *J. Am. Soc. Echocardiogr. 20*(1), 45–53.

Maier, S. E., S. E. Fischer, G. C. McKinnon, O. M. Hess, H. P. Krayenbuehl, and P. Boesiger (1992). Evaluation of left ventricular segmental wall motion in hypertrophic cardiomyopathy with myocardial tagging. *Circulation 86*(6), 1919–1928.

Notomi, Y., P. Lysyansky, R. Setser, T. Shiota, Z. Popovic, M. Martin-Miklovic, J. Weaver, S. Oryszak, N. Greenberg, R. White, and J. Thomas (2005). Measurement of ventricular torsion by two-dimensional ultrasound speckle tracking imaging. *J. Am. Coll. Cardiol. 45*, 2034–2041.

Notomi, Y., R. Setser, T. Shiota, M. Martin-Miklovic, J. Weaver, Z. Popovic, H. Yamada, N. Greenberg, R. White, and J. Thomas (2005). Assessment of left ventricular torsional deformation by Doppler tissue imaging: validation study with tagged magnetic resonance imaging. *Circulation 111*, 1141–1147.

Ryf, S., M. Spiegel, M. Gerber, and P. Boesiger (2002). Myocardial tagging with 3D-CSPAMM. *J. Magn. Reson. Imaging 16*, 320–325.

Ryf, S., J. Tsao, J. Schwitter, A. Stuessi, and P. Boesiger (2004). Peak-combination harp: A method to correct for phase errors in harp. *J. Magn. Reson. Imaging 20*(5), 874–80.

Takeuchi, M., H. Nakai, M. Kokumai, T. Nishikage, S. Otani, and R. Lang (2006). Age-related changes in left ventricular twist assessed by two-dimensional speckle-tracking imaging. *J Am Soc Echocardiogr 19*, 1077–1084.

Takeuchi, M., T. Nishikage, H. Nakai, M. Kokumai, S. Otani, and R. Lang (2007). The assessment of left ventricular twist in anterior wall myocardial infarction using two-dimensional speckle tracking imaging. *J. Am. Soc. Echocardiogr. 20*(1), 36–44.

Tibayan, F. A., F. Rodriguez, F. Langer, M. K. Zasio, L. Bailey, D. Liang, G. T. Daughters, N. B. J. Ingels, and D. C. Miller (2004). Alterations in left ventricular torsion and diastolic recoil after myocardial infarction with and without chronic ischemic mitral regurgitation. *Circulation 110*(11 Suppl 1), 109–114.

Young, A., H. Imai, C. Chang, and L. Axel (1994). Two-dimensional left ventricular deformation during systole using magnetic resonance imaging with spatial modulation of magnetization [published erratum appears in circulation 1994 sep;90(3):1584]. *Circulation 89*, 740–752.

Accepted for publication in Ultrasound Med. Biol., 2008

Paper C

3D Speckle Tracking for Assessment of Regional Left Ventricular Function

Jonas Crosby*, Brage H. Amundsen*, Torbjørn Hergum*, Espen W. Remme†, Stian Langeland‡ and Hans Torp*
*) Department of Circulation and Medical Imaging, Norwegian University of Science and Technology, Trondheim, Norway
†) Institute for Surgical Research, Rikshospitalet University Hospital, Oslo, Norway
‡) GE Vingmed Ultrasound AS, Horten, Norway

Speckle tracking in two-dimensional ultrasound images has become an established tool for assessment of left ventricular function. The recent development of ultrasound systems with capability to acquire real-time full volume data of the left ventricle makes it possible to perform speckle tracking in three dimensions, and thereby track the real motion of the myocardium. This paper presents a method for assessing local strain and rotation from 3D speckle tracking in apical full-volume data sets. The method has been tested on simulated ultrasound data based on a computer model of the left ventricle, and on patients with myocardial infarction. When applied on simulated ultrasound data, the method showed good agreement with strain and rotation traces calculated from the reference motion, and the method was able to capture segmental differences in the deformation pattern although the magnitudes of strains were systematically lower than the reference strains. When applied on patients, the method demonstrated reduced strain in the infarcted areas. Bulls-eye plots of regional strains showed good correspondence with wall motion scoring based on 2D apical images, although the dys- and hypokinetic regions were not apparent in all strain components.

The video clips cited in this article can be found online at http://www.umbjournal.org.

C.1 Introduction

The advent of ultrasound scanners with full volume imaging capabilities has prepared the ground for 3D speckle tracking. However, with the introduction of a new dimension, new challenges arise. The number of beams needed in a full volume acquisition of the left ventricle (LV) limits frame rate. Several techniques have been applied to overcome the frame rate problem, including gated capture over several cardiac cycles (usually 4-6) (Brekke et al., 2005) and multiple line acquisition where multiple image scan lines are obtained for each transmit pulse (von Ramm et al., 1991). Using these techniques, the current commercial systems are able to assess 3D full volume images of the LV at a rate of about 20 frames per second (fps). For 2D speckle tracking of conventional B-mode images, a minimum frame-rate of at least 30 fps is recommended by most studies (Ingul et al., 2005; Suffoletto et al., 2006) due to the frame-to-frame changes (decorrelation) of the speckle pattern caused by factors such as out-of-plane motion and tissue deformation. With 3D speckle tracking on the other

hand, there will be no problems with out-of-plane motion and the temporal correlation is therefore expected to improve. In this study, we have examined the performance of a 3D speckle tracking algorithm when applied to full volume ultrasound recordings of the LV.

Speckle is an inherent characteristic of ultrasound imaging and arises because sub-resolution scatterers cause interference patterns in the image. The observed speckle pattern would therefore not correspond to the underlying structure of the tissue (Anderson and Trahey, 2006). The speckle pattern is deterministic but will gradually change when the structure is deformed, or when the angle between the structure and the local wave-front changes (Meunier, 1998). As long as these changes are small, the local motion of material points between two frames can be estimated by tracking of the speckle patterns in the images. This is often referred to as *speckle tracking* but as the tracking is also affected by the motion of larger structures, the term *feature tracking* is preferred by some authors.

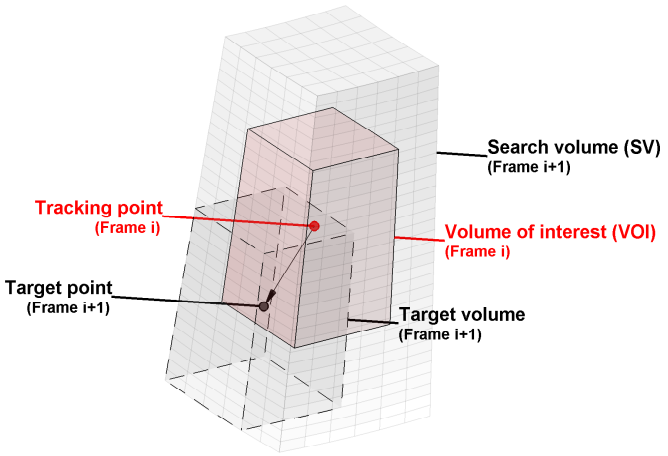

Figure C.1: Speckle tracking in 3D sector scan

Speckle tracking is performed by block matching, where the displacement of a material point is found as the displacement of a region of interest around the point in the source frame that results in the best match with a target frame. The displacement search is usually limited to a search region around the point based on assumptions of the maximal tissue velocities. Figure C.1 illustrates the block matching in volume data.

Different matching criteria can be applied. The most common is to maximize the normalized cross correlation coefficient, or minimize the sum of squared differences (SSD) or the sum of absolute differences (SAD). The speckle pattern is observable in radio frequency data (RF-data) as well as in the envelope-detected and scan-converted data. All of these representations can therefore be used as a basis for speckle tracking. To be able to assess sub-sample resolution of the frame-to-frame

displacement estimates, some kind of interpolation technique has to be applied (Geiman et al., 2000). This is especially important in the two lateral directions (azimuth and elevation) where the resolution usually is lower than in the range direction. One possibility is to interpolate the image data. However, for most applications it is more suitable to interpolate the matching function in order to limit memory requirements and computation time.

Most of the early work on 3D speckle tracking has been limited to simulated data and theoretical studies due to lack of commercially available ultrasound scanners with volume acquisition. Meunier (1998) investigated how 3D speckle motion correlated with 3D tissue translation, rotation and deformation. This was further investigated in a study by Yu et al. (2006), which also examined the feasibility of speckle tracking on RF-data versus envelope-detected data. Chen et al. (2005) showed the benefits of 3D speckle tracking using a correlation-based method applied on simulated ultrasound images of a bar phantom, and Jia et al. (2007) compared 2D and 3D speckle tracking using a pulsative tissue-mimicking LV phantom, which made it possible to record volume data with increased number of frames per cycle. Song et al. (2007) demonstrated 3D speckle tracking in real data sets using motion coherence of a set of septal points, and reported good agreement with manual tracking of the same points.

An alternative approach for assessment of 3D LV deformation by ultrasound has been presented by Elen et al. (2007), where the transformation of the data between frames is estimated using spatio-temporal elastic registration. This approach has however currently much longer processing time than speckle tracking, with reported frame-to-frame registration time between 30-45 minutes.

The aim of this study was to develop a robust and fast 3D speckle tracking method for assessment of regional LV function. The developed algorithm is described in detail, and has been tested on synthetic 3D ultrasound data with known reference motion. The algorithm was also demonstrated on human subjects; one healthy and two patients with different infarct locations.

C.2 Methods

C.2.1 The 3D speckle tracking algorithm

Our algorithm tracks and regularizes the motion of the left ventricular wall, given an initial quadrilateral mesh of tracking points in one initial frame. The block matching is done on envelope-detected beam data using SAD as the matching function. The size of the volume of interest (VOI) that is used as matching kernel is defined in rectangular (Cartesian) coordinates, and thereafter converted to an integer number of beams and samples in beam space according to depth r (i.e. the distance to the probe).

$$VOI_{bs} = \left[\lfloor \frac{\Delta y}{dr} \rfloor, \lfloor \frac{\Delta x}{r d\theta} \rfloor, \lfloor \frac{\Delta z}{r d\phi} \rfloor \right] \tag{C.1}$$

where Δx, Δy, and Δz determine the spatial extent of the VOI, and $d\theta$ and $d\phi$ are the angular differences between neighbor beams. A lower limit is placed on the VOI to

ensure that it contains a minimal number of beams at all depths. The search volume should be large enough to cover all possible myocardial velocities. In order to limit the search volume size, the displacement of the atrioventricular (AV) plane is estimated first by tracking a set of VOIs in the beam direction. This displacement estimate is then used to shift the center of the search volumes along the beam according to their depth in each frame, by assuming that the velocity varies linearly from the probe to the depth of the mitral valve. The search volume is limited by the maximal expected myocardial velocities relative to the shifted center of the search volume. Similar to the VOI, the lateral extent of the search volume is calculated for each depth in order to compensate for the geometry of the sector scan.

When the integer displacement between two frames has been found as the displacement that minimizes the SAD, normalized cross correlation coefficients are calculated from the VOIs around the SAD minimum and around its six neighbor voxels. The sub-resolution displacement component δ is estimated in each direction across the SAD minimum by fitting a Gaussian function to the three directional neighbors of these seven correlation coefficients (Westerweel, 1993):

$$\delta = 0.5 \frac{ln(\rho_{-1}) - ln(\rho_{+1})}{ln(\rho_{-1}) - 2ln(\rho_0) + ln(\rho_{+1})} \tag{C.2}$$

where ρ_{-1}, ρ_0 and ρ_{+1} are the correlation coefficients in one of the directions.

A regularization of the displacement of the LV mesh is performed after each tracking step. Points that fall outside the sector or points with poor tracking quality (i.e. correlation coefficients < 0.1) are automatically excluded. The displacement vectors are converted to true space (Cartesian) coordinates. Each displacement vector is decomposed into three orthogonal components: A transmural component perpendicular to the mesh, a longitudinal, and a circumferential component. Missing values are estimated using a spring metaphor, which minimizes the difference to adjacent points by calculating the least squares solution to a set of linear equations. Each component is smoothed separately, using a two dimensional Gaussian low-pass filter with a standard deviation equal to three mesh points. Finally, the displacements are added to the coordinates of the tracking points in the previous frame.

The tracking is performed both forwards and backwards through the cardiac cycle, and the coordinates of the tracking points from each direction are then weighted linearly in time in order to compensate for drift.

When the orientation of the LV is indicated by the user, the LV mesh is divided into 16 segments (Cerqueira et al., 2002), thereby making segmental analysis possible (Fig. C.2).

C.2.2 Generation of synthetic ultrasound data

A computer simulated ultrasound full-volume data of a simplified dynamic model of LV myocardium was generated in order to compare the 3D speckle tracking with a known reference motion. The LV myocardium was modeled as a set of point scatterers with zero-mean Gaussian distributed backscatter coefficients. Each scatterer was displaced through the cardiac cycle according to the calculated motion of the LV

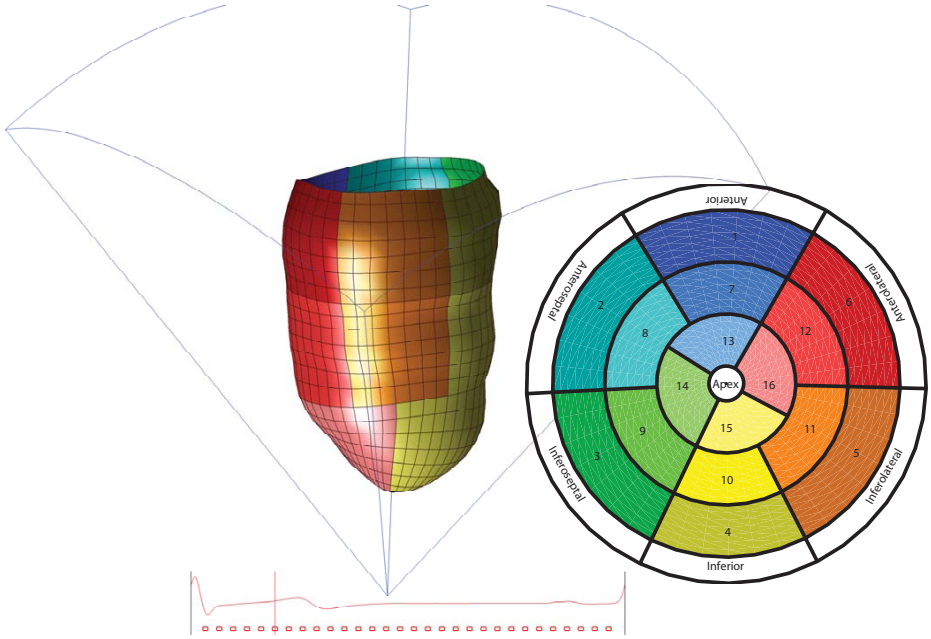

Figure C.2: Left ventricular segments.

wall obtained from a finite element (FE) simulation model of an ellipsoidally shaped LV (Remme and Smiseth, 2007). Simulated ultrasound images were generated from this model by using an in-house ultrasound imaging simulation program, called FUSK (Fast Ultrasound Simulation in K-space) (Hergum et al., 2006). FUSK is a fast 3D ultrasound imaging simulation tool, where a point spread function is convolved with the point scatterers of the model. This convolution is performed in the frequency domain to reduce processing time, and the scatterer positions are transformed to beam-space instead of Cartesian space. Having a spatially invariant ultrasound imaging system in beam-space equals imaging using a constant f-number (i.e. the ratio of depth to aperture), which is a good approximation of using a wide transmit beam, dynamic focus and expanding aperture upon reception. These are quite typical settings for cardiac imaging if parallel beams are used. The point spread function is constructed in the baseband of the spatial frequency domain (K-space) according to the Fraunhofer approximation (Walker and Trahey, 1998). The point scatterers are filtered with a baseband-demodulated antialiasing filter, making sure that the filter has a wider transition band than the point spread function along all dimensions. This enables the simulation to run on a beam-space grid and still handle sub-resolution movement of scatterers between frames, as this is crucial for the time-dependence of the speckle pattern. Together these approximations make the simulation tool run three orders of

Table C.1: Tracking parameters.

VOI kernel size:	$6 \times 6 \times 6$	mm
Search volume size		
- max. lateral velocity:	50	mm/s
- max. axial AV velocity (pretrack):	250	mm/s
- max. axial velocity deviation:	50	mm/s

Table C.2: Study subjects.

Subject	Description	Sex	Age	Heart rate (bpm)	Frame rate (Hz)	Data size
1	Healthy	M	21	54	27.6	396×100×56
2	Anterior MI	M	52	57	29.5	364×100×56
3	Inferior MI	M	70	50	22.4	364×116×64

magnitude faster than impulse-response based simulators like Field II (Jensen, 2004).

Images are made from the resulting complex demodulated data (IQ-data) by detection, logarithmic compression and scan-conversion. Figure C.3 shows an example of a simulated LV. A movie clip showing a complete simulated cardiac cycle can be found in Movie 1 in the online edition.

C.2.3 Testing of the algorithm on synthetic data

A complete cardiac cycle with total duration of one second was created *in silico*, consisting of 21 simulated 3D images constructed from the left ventricular FE-model with an inferoapical myocardial infarction (MI) (see Fig. C.3). The simulation parameters were chosen to be comparable to the specifications of the V3S matrix array probe (GE Vingmed Ultrasound, Horten, Norway). The frequency was 1.7 MHz on transmit and 3.4 MHz on receive (harmonic imaging) and the size of the resulting beam space volume was 343 *samples* × 149 *azimuth beams* × 117 *elevation planes*.

The initial geometry was set to correspond to material mid-wall points from the FE model in end-systole, in order to allow point-wise comparison of the tracked motion. The simulated ultrasound data were tracked using the speckle tracking method with the settings in Table C.1. Longitudinal and circumferential strains ϵ were calculated as:

$$\epsilon(t) = \frac{L(t) - L_0}{L_0} \tag{C.3}$$

where $L(t)$ is the distance between two neighbor points in the ordered mesh at time t, and L_0 is the distance between the same points in end-diastole. The strain values from speckle tracking were compared with strain calculated from the corresponding scatterers from the model. Transmural strain $\epsilon_{trans}(t)$ was approximated (assuming

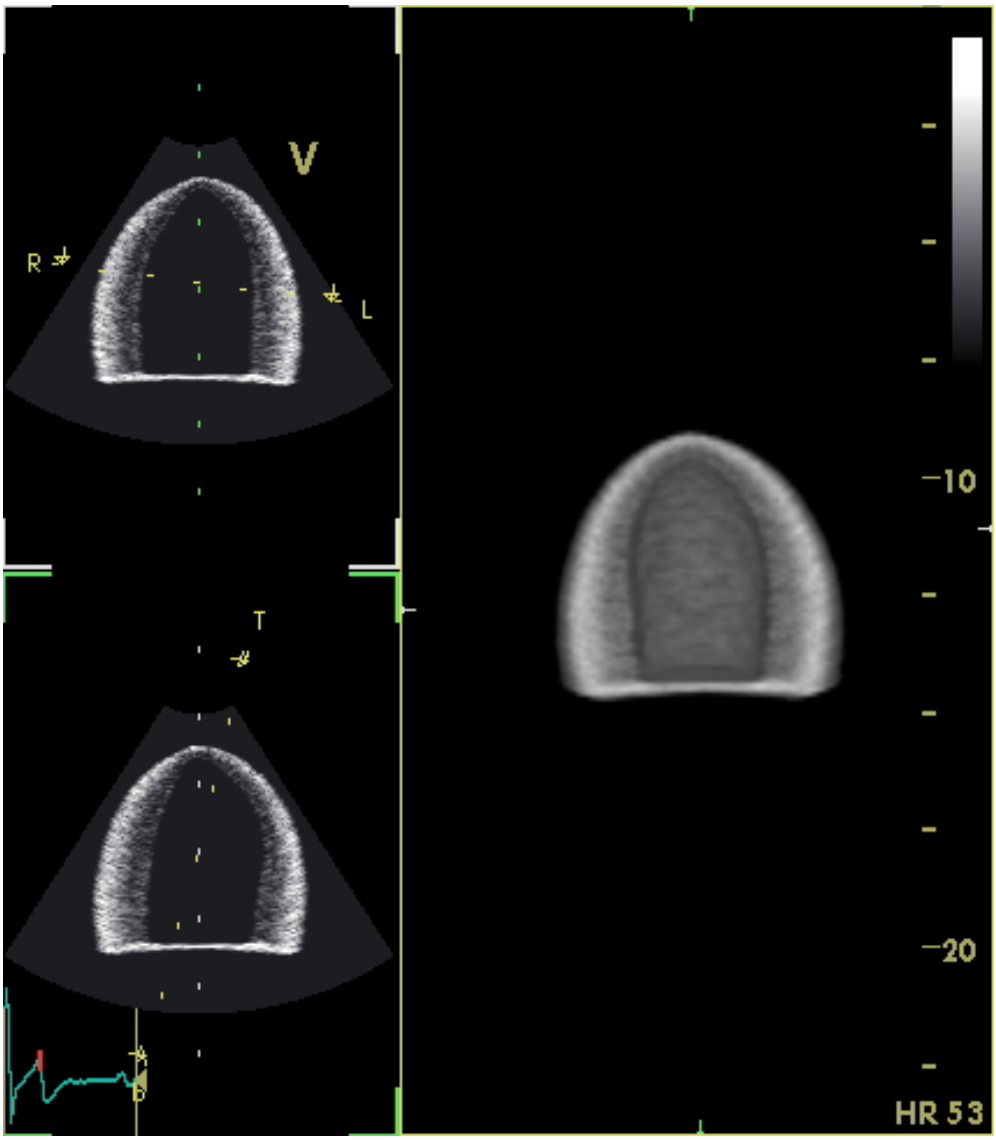

Figure C.3: Simulated ultrasound image of the left ventricle: Cross-sections (left panel) and volume rendering (right panel).

incompressible myocardium and neglecting shear strains) as:

$$\epsilon_{trans}(t) \approx \frac{1}{(1+\epsilon_{long}(t))\,(1+\epsilon_{circ}(t))} - 1 \tag{C.4}$$

Points with average correlation coefficients below 0.1 were omitted from the calculation of segmental strain.

LV rotation was calculated as the angular displacement of the tracked points around the long-axis defined by the apex and the center of the basal points. Positive rotation values correspond to clockwise rotation as seen from the apex.

C.2.4 Testing of the algorithm on human data

Three male subjects, two with previous MI and one healthy volunteer (Table C.2), were included in the study after having given written informed consent. These example subjects were selected from a population in an earlier study (Amundsen et al., 2008) consisting of 21 subjects (11 healthy, 10 patients with MI) on the basis of image quality (absence of imaging artifacts and good LV coverage). The study protocol was approved by the Regional Committee for Medical Research Ethics. Full volume apical images of the LV were obtained using a Vivid 7 ultrasound scanner (GE Vingmed Ultrasound, Horten, Norway) and a V3S matrix array probe. Additionally, in order to be able to perform conventional wall motion scoring, standard 2D apical 4-chamber, 2-chamber and long-axis views were recorded using a phased array probe (M3S, GE Vingmed Ultrasound, Horten, Norway). The frequency was 1.7 MHz on transmit and 3.4 MHz on receive.

The LV geometry was initialized in end-systole by fitting a cropped ellipsoid to a set of user-drawn points, by solving a non-linear least squares problem. Tracking points were distributed in an ordered mesh on the cropped ellipsoid, with a longitudinal spacing of 3 *mm* and a maximal circumferential spacing of 3 *mm*. The ellipsoidal mesh was then automatically deformed locally to make the mesh coincide with the user-drawn points, thereby allowing more irregular geometries.

Three-dimensional speckle tracking was performed on the recorded data, using the same settings as on the synthetic data (see Table C.1). Longitudinal and circumferential strains were compared qualitatively with results from coronary angiography and with wall motion scoring on standard 2D apical views by an experienced cardiologist blinded to other data (Schiller et al., 1989). Strain and rotation were calculated as for the synthetic data. Points outside the sector or with average correlation coefficients below 0.1 were omitted from the calculation of segmental strain.

C.3 Results

C.3.1 Testing of the algorithm on synthetic data

Figure C.4 shows the tracked mesh in end-diastole and end-systole. A corresponding video clip showing the tracking can be found in Movie 2 (online supplement).

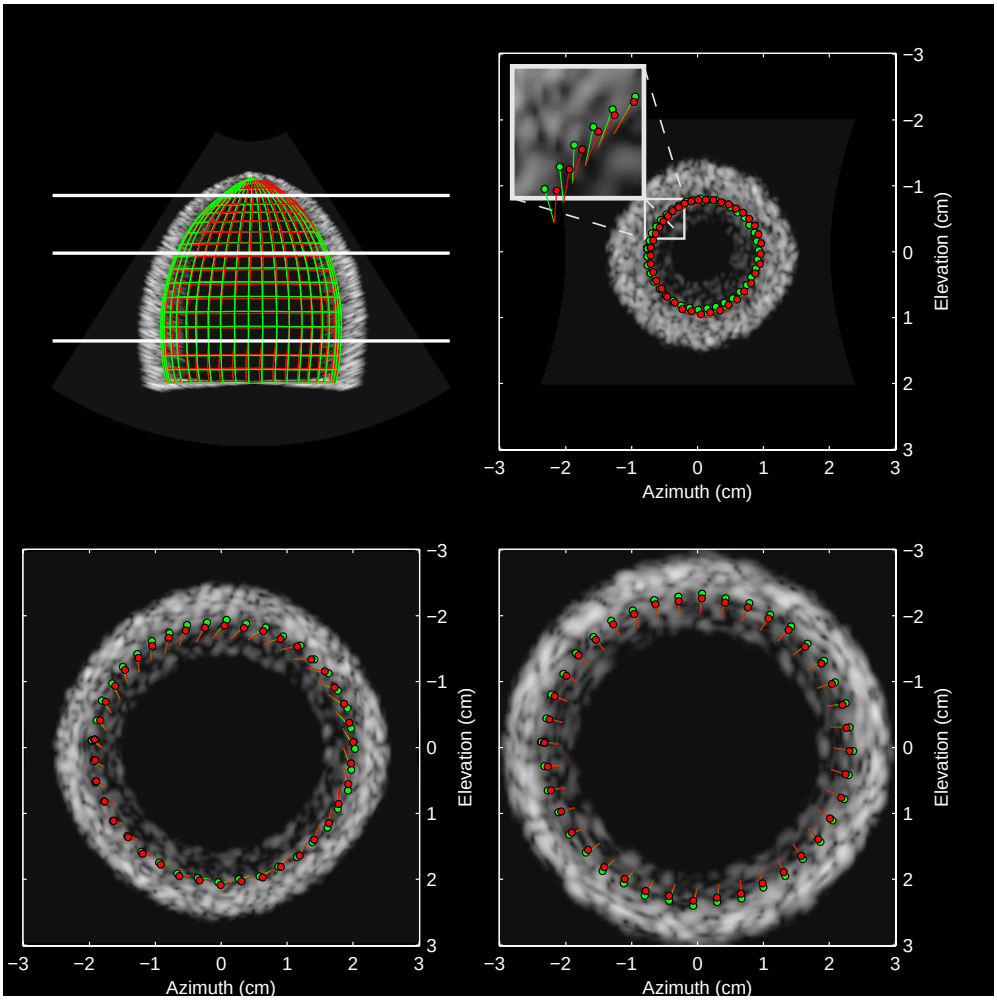

Figure C.4: Three-dimensional speckle tracking in a simulated left ventricle in *end-diastole*. The tracked mesh (red) and the reference mesh (green) are shown in the leftmost panel. The other panels show the intersections of the tracked mesh (red markers) and the reference mesh (green markers) with three short-axis levels, with vectors indicating the displacements relative to the end systolic configuration.

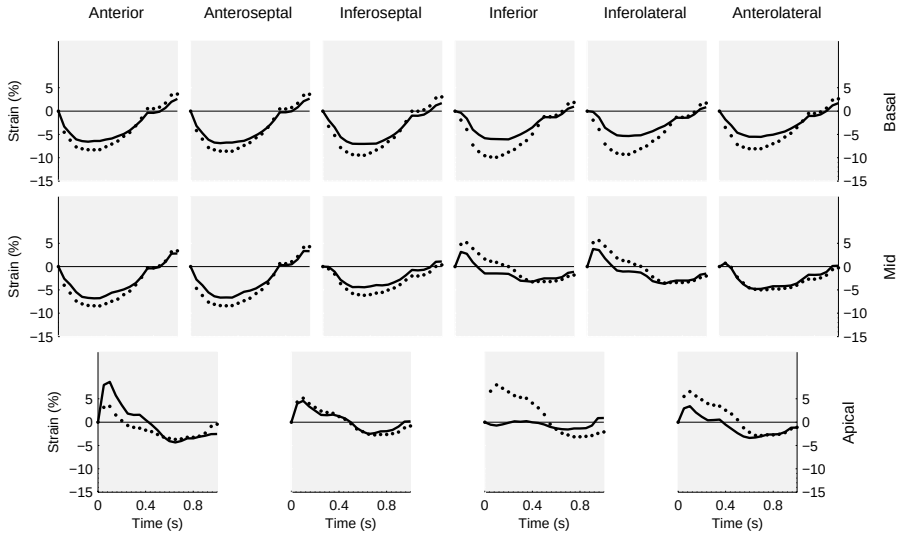

Figure C.5: Longitudinal strain from simulated ultrasound data in 16 left ventricular segments. Solid lines show strain estimated by speckle tracking and dashed lines show strain calculated from the reference model.

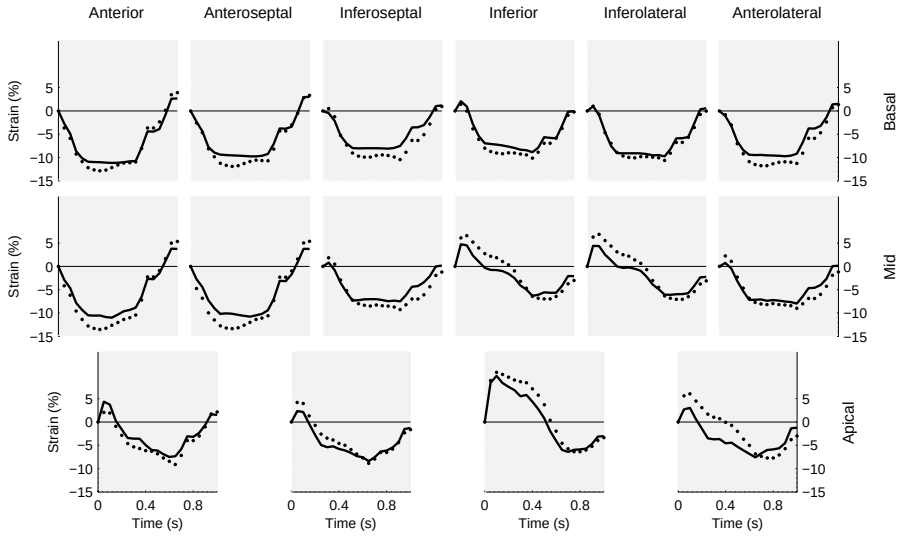

Figure C.6: Circumferential strain from simulated ultrasound data in 16 left ventricular segments. Solid lines show strain estimated by speckle tracking and dashed lines show strain calculated from the reference model.

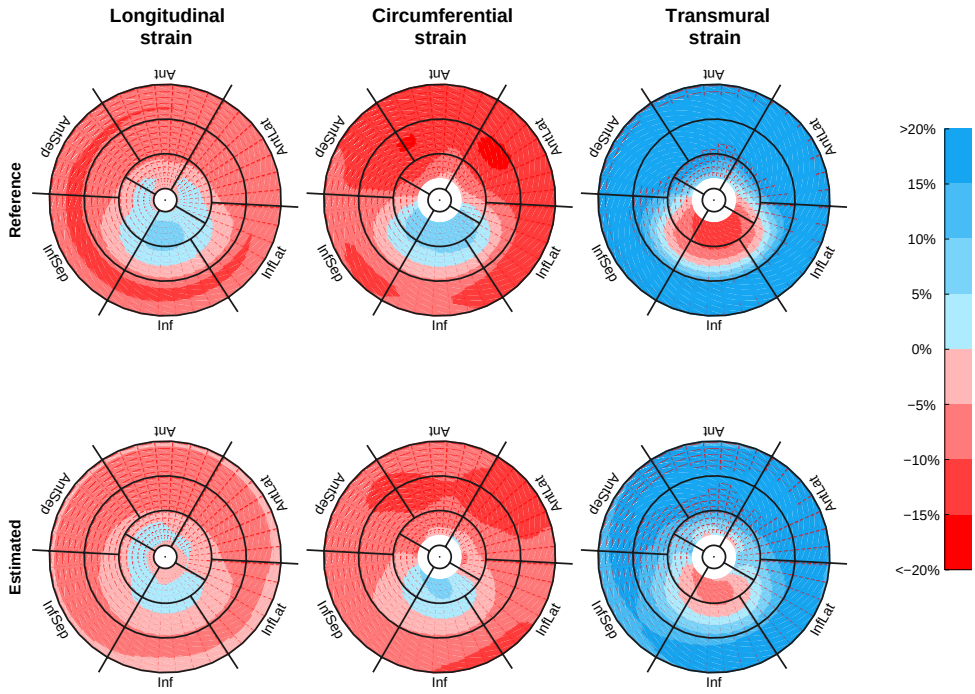

Figure C.7: Bulls-eye plots showing end-systolic longitudinal, circumferential and transmural strain from the reference model (upper row) and as estimated by 3D speckle tracking (lower row).

Figure C.5 shows longitudinal strain from speckle tracking and the corresponding material points from the model, and it can be seen that the method was able to differentiate between healthy segments and pathological apical segments. In the inferoapical segment, the tracking failed to capture the rapid initial systolic stretching. The same ischemic pattern was found for circumferential strain (Fig. C.6); however, in this case the pathological stretching of the inferoapical segment was captured correctly.

Bulls-eye plots of the end-systolic strain (Fig. C.7) show that the extent and location of the apical myocardial infarction was detected by the speckle tracking. In the figure, red colors correspond to contraction and blue colors correspond to elongation or thickening. Analysis of the end-systolic circumferential strain values shows that speckle tracking on average underestimated the circumferential strain by 20% for absolute reference strains above 5%. For end-systolic longitudinal strain, the average underestimation by speckle tracking was 26%.

Figure C.8 shows the change in end-systolic rotation from apex to base from the

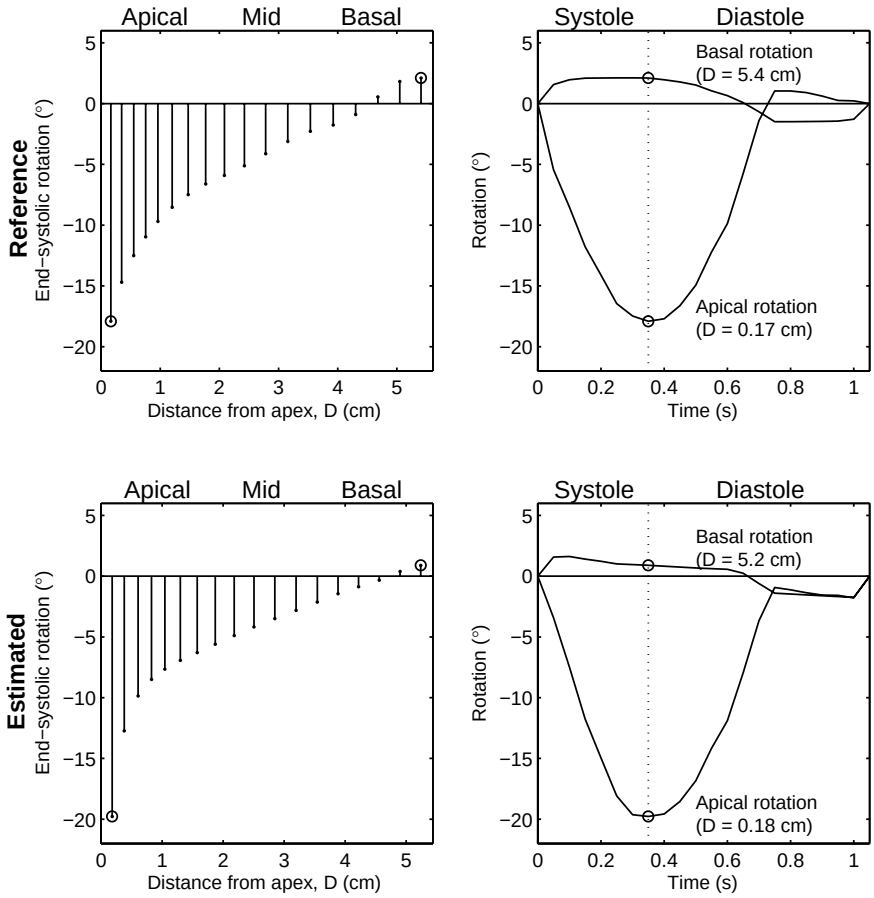

Figure C.8: End-systolic rotation from base to apex (left column) and basal and apical rotation traces (right column) calculated from the reference model (upper row) and as estimated by speckle tracking (lower row).

reference model and estimated by the speckle tracking, and examples of apical and basal rotation traces. The gradual change from counter-clockwise rotation at the apex to clockwise rotation at the base is detected by the speckle tracking.

C.3.2 Testing of the algorithm on human data

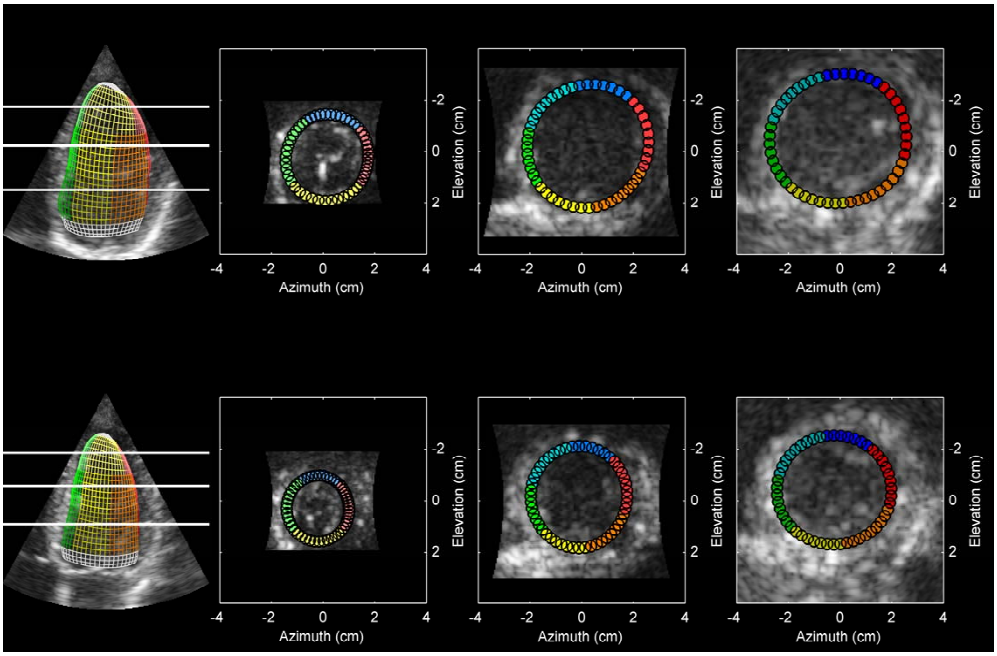

Figure C.9: Three-dimensional speckle tracking in a healthy left ventricle. Upper row: The tracked mesh in *end-diastole* (left column) and its intersections with three short-axis levels. Lower row: The tracked mesh in *end-systole* (left column) and its intersections with three short-axis levels. The color coding corresponds to the division into LV segments.

Figure C.9 shows the tracked mesh for the healthy subject at end-diastole and end-systole. Video clips showing the tracking in all three subjects can be found in Movies 3–5 (online supplement). Figures C.10 and C.11 show longitudinal and circumferential strain in each of the LV segments as estimated by the speckle tracking method. The healthy subject was shown to have a regular strain pattern in all segments. Average longitudinal and circumferential strain was $-15,3\%$ and -22.1%, respectively. The absolute value for peak systolic longitudinal strain increased from base (11.3%) to apex (19.6%), and the absolute peak systolic circumferential strain was reduced in the septal segments.

Coronary angiography identified left anterior descending artery and right coronary artery as culprit arteries in subject 2 and 3, respectively. Bulls-eye plots of the strain

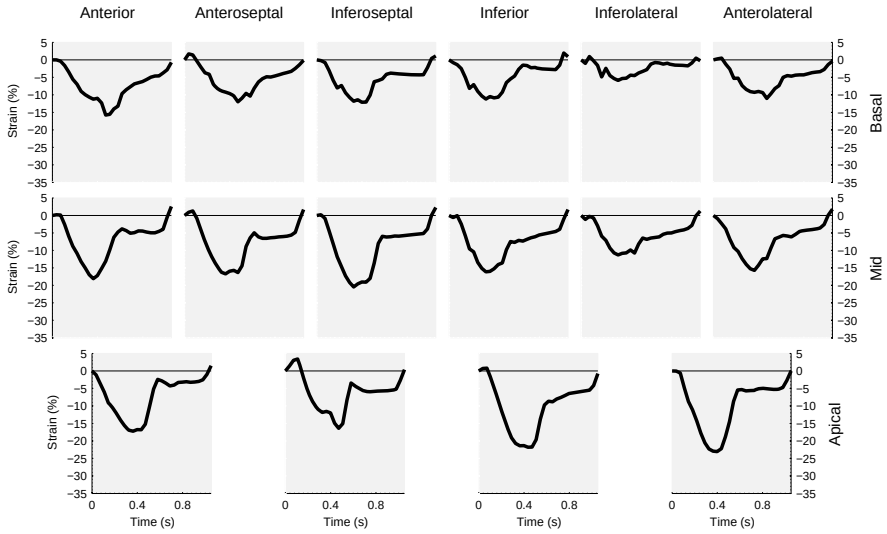

Figure C.10: Longitudinal strain in 16 left ventricular segments estimated by speckle tracking in a healthy subject.

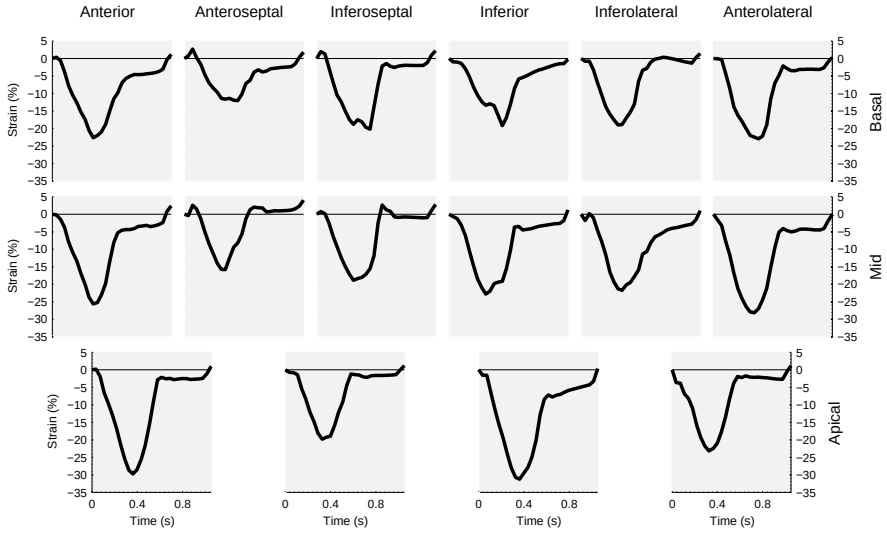

Figure C.11: Circumferential strain in 16 left ventricular segments estimated by speckle tracking in a healthy subject.

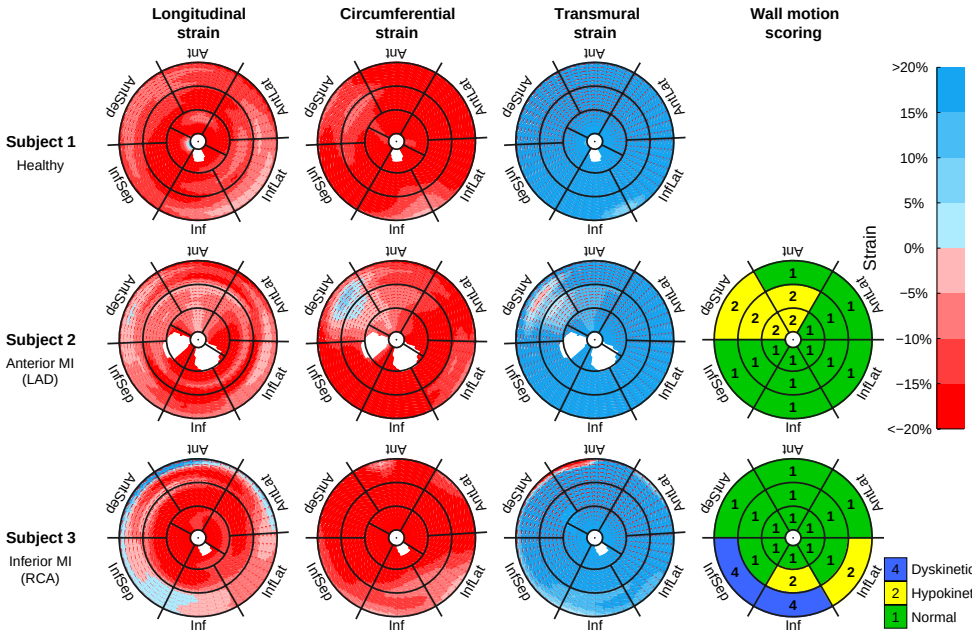

Figure C.12: Bulls-eye plots showing end-systolic longitudinal, circumferential and transmural strain estimated by 3D speckle tracking in three subjects, and wall motion scoring based on 2D apical images from the two patients. White spots correspond to areas with insufficient tracking. (*LAD: left anterior descending artery; RCA: right coronary artery; Ant: anterior; Inf: inferior, Sep: septal; Lat: lateral.*)

distribution in the LVs are seen in Fig. C.12. The white regions seen in the bulls-eye plots correspond to missing values caused by motion of tracked apical points out of the image volume. The results of the wall motion analysis for the two patients are displayed as bulls-eye plots in Fig. C.12. For the subject with anterior MI, a hypo- and dyskinetic area is apparent in the anterior and anteroseptal segments in the three strain plots. This area corresponds to the segments labeled as hypokinetic in the wall motion plot. For the subject with inferior MI, an area with reduced strain is seen in the basal inferoseptal to inferolateral segments. In the bulls-eye plot showing longitudinal strain, a distinct dyskinetic area is observed in the basal inferior and inferoseptal segments, corresponding to the area with reduced function shown by wall motion analysis. In addition, a thin dyskinetic area close to the base is seen in the anteroseptal to the anterolateral segments for the longitudinal and transmural strain plots.

Figure C.13 shows the change in end-systolic rotation from apex to base estimated by speckle tracking, and examples of apical and basal rotation traces from the healthy volunteer. The end-systolic rotation changed gradually from a small clockwise rotation

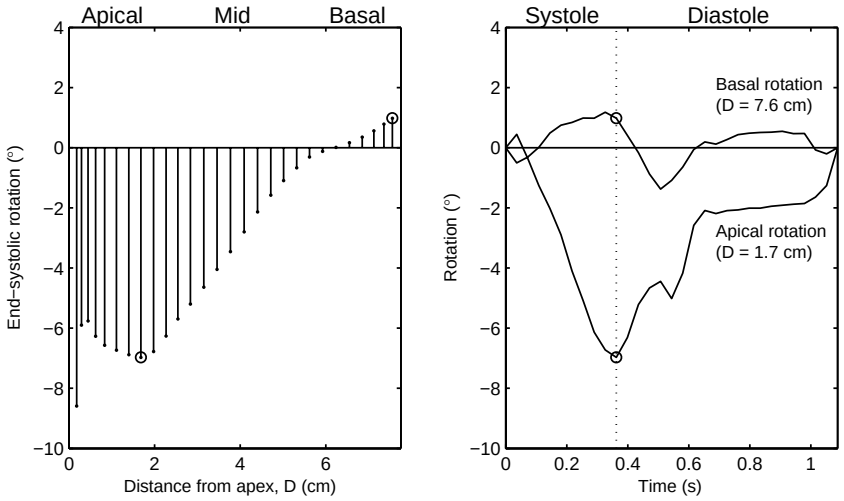

Figure C.13: Rotation in a healthy subject estimated by speckle tracking. Left: End-systolic rotation as a function of the distance to the apex. Right: Apical and basal rotation traces.

at the base to a larger counter-clockwise rotation at the apex.

Bidirectional speckle tracking and regularization of one LV mesh for a complete cardiac cycle took approximately 4 minutes on a 1600–MHz Intel Pentium M processor.

C.4 Discussion

C.4.1 General discussion of the 3D speckle tracking algorithm

The developed algorithm tracks tissue motion by SAD block matching and utilizes the correlation coefficients in order to achieve sub-voxel displacements. The search volume size is limited by pre-tracking of the AV-plane motion, and regularization of the displacement vectors is done by local smoothing of the components parallel and perpendicular to the tracking mesh. The method makes it possible to estimate longitudinal and circumferential strain in all LV segments and the change in LV rotation along the center axis. In addition, transmural strain is approximated by assuming volume conservation.

The block-matching approach is dependent on preservation of image features from frame to frame. Deformation and rotation around an axis that is perpendicular to the beams change the speckle pattern and lead to decorrelation in the block-matching. For a 3–MHz transducer, a paper by Meunier (1998) states that such rotation should be below about 4° and that the deformation should be below about 10% between frames to permit reliable speckle tracking. In sector-scans, lateral translation would also result in decorrelation of the speckle pattern, as this corresponds to a rotation relative to the

beam angle (Meunier and Bertrand, 1995; Trahey et al., 1986). Trahey et al. (1986) showed that a lateral displacement of approximately 40% of the effective aperture would remove the correlation of the speckle pattern. Local rotation around an axis parallel to the local beam direction should not change the speckle pattern. However, this will still cause a mismatch in the current block-matching implementation, which assumes that the VOI is subject to translation only and neglects any rotation or deformation of the tissue within the VOI. This could be solved by allowing rotation of the volume of interest, at the expense of computational efficiency. For the subjects in this study, with cycle lengths > 1 s and frame rate > 20 fps, it is expected that the frame-to-frame deformation and rotation is below the theoretical limits. However, the rotation and deformation would still lead to some decorrelation and thereby increase the possibility of erroneous displacement estimates.

The choice of the size of the search volume is an important factor in 3D speckle tracking. Too large search volumes will increase the computational cost and the risk of random matches far away from the source point. On the other hand, too small search volumes would always lead to erroneous matches, although closer to the source points. Another important factor is the amount of regularization performed on the tracking. Less spatial regularization of the displacements along the mesh would result in less smoothing of the borders between areas with high and low strain values, e.g. an infarct border zone. At the same time, it would also make the overall tracking more sensitive to errors originating from VOIs with erroneous displacement estimates. In other words, less regularization is expected to increase the method's sensitivity to detect small regions with reduced deformation, but would decrease the specificity. Spatial regularization may result in an underestimation of local excursion, and may also induce a bias in the displacement estimates in the case of systematic tendencies of the random tracking errors in each point.

Assessment of tracking quality is important for the interpretation of the results. Visual inspection of how well the tracked points follow the tissue can be difficult and time consuming in full volume data, and an automatic measure of tracking quality is therefore desirable. The correlation coefficient by itself is an unreliable quality parameter because a low value is not necessarily inconsistent with a precise and unambiguous displacement estimate. The shape of the correlation function around the best match would therefore probably be a better indicator of tracking quality. In patients with a steady heart rate, the amount of drifting during the cardiac cycle could be used as a quality measure. The divergence of the displacement estimates from adjacent points could also be used as a measure of tracking quality, as the myocardium is assumed to be a continuous medium. In the current study, exclusion of displacement estimates was done by a simple threshold on the correlation coefficients, which in this initial algorithm presentation deliberately was set very low in order to avoid unjustified exclusion of tracking points. A more advanced exclusion scheme could be advantageous in less optimal data sets.

The tracking of a complete cardiac cycle takes about 4 minutes using the current implementation and the tracking parameters in Table C.1. The tracking time is mainly determined by the size of the VOIs, the search volumes and the number of tracking points. The processing time is expected to be further reduced, with no significant

loss of tracking quality, by software optimization (e.g. by parallelization of the SAD-matching), optimal selection of tracking parameters and hardware upgrades. Omitting the backward tracking would reduce the tracking time with almost 50%, but this would also increase the impact of drift in the tracking. In addition, the processing time could be decreased by reducing the number of VOIs at the sacrifice of spatial resolution. With these speed improvements, 3D speckle tracking of the complete LV in less than a minute should be achievable. In this study, the LV geometry in the first frame was based on a set of user-placed points. This initialization process could be replaced by automatic or semiautomatic 3D segmentation (Angelini et al., 2005; Hansegård et al., 2007), making the overall deformation analysis faster and less user-dependent.

C.4.2 Testing of the algorithm on synthetic data

When the method was applied on simulated ultrasound data, the resulting traces of segmental strain showed good correspondence with the reference motion for both shape and magnitude (Figs. C.5 and C.6). However, the simulation results showed a systematic underestimation of the magnitudes of both circumferential and longitudinal strains that is not seen in studies with 2D speckle tracking (Amundsen et al., 2008). This might be a result of the spatial regularization of the displacement estimates, an effect of the relatively large ROIs used in this study, or a result of accumulation of errors in the subvoxel estimates.

The ischemic area is evident in the bulls-eye plots showing end-systolic strain in Fig. C.7, but the border zone between areas with high and low strain is somewhat smoothed due to the regularization of the tracking mesh. Some minor tracking artifacts are seen near the apex, especially for the inferoapical longitudinal strain.

The failure to track the rapid early systolic lengthening of the infarcted inferoapical segment in the simulation could be explained by the decorrelation of the speckle pattern associated with the large frame-to-frame deformation. It is therefore likely that increased frame rate would improve the tracking in this segment. The method was able to capture the torsional motion of the simulated LV (Fig. C.8), which demonstrates that the speckle tracking is following the tissue motion and not just the blood-tissue boundary.

C.4.3 Testing of the algorithm on human data

In the testing of algorithm on human data there was no known reference motion, but the results were qualitatively comparable with the results from coronary angiography and wall motion analysis. For the healthy subject, the strain traces had physiological shapes showing monotonic contraction in systole followed by elongation in diastole. The absolute ES strain values were in the lower range of normal values reported by MRI tagging (Bogaert, 2005) and 2D speckle tracking in ultrasound (Leitman et al., 2004; Serri et al., 2006). For the circumferential strain, the low strain values could be explained by the increase in circumferential contraction towards the endocardium, which has been previously reported by e.g. Clark et al. (1991). As the size of the VOI used in our study included much of the thickness of the wall, and the block-

matching approach probably is biased towards the epicardium where there is the least myocardial deformation, the absolute values of circumferential strain values from the speckle tracking methods could be expected to be lower than e.g. the subendocardial measurements in the MRI study by Bogaert (2005). The rotation pattern in Fig. C.13 is also in agreement with studies of normal hearts by 2D speckle tracking and MRI (Buchalter et al., 1990; Helle-Valle et al., 2005; Notomi et al., 2005): The base has a brief counter-clockwise rotation in early systole that is followed by a larger clockwise rotation, while at the apex the counter-clockwise rotation continues until end-systole. The unexpected drop in rotation values close to the apex could indicate some difficulties in tracking the rotation in the most apical region. This region is characterized by large frame-to-frame rotation close to the rotation axis that could be difficult to capture by the relatively large VOIs used in the block matching.

The results of the wall motion analysis were consistent with the culprit arteries identified by the coronary angiography. The wall motion scoring is principally based on wall thickening and is therefore expected to correlate best with the transmural strain values. In Fig. C.12, the transmural strain is seen to detect reduced contraction in the segments labeled as hypo- or dyskinetic by the wall motion analysis, but no transmural thickening is observed in the segments labeled as dyskinetic. The thin basal dyskinetic area seen in the bulls-eye plots from the patient with inferior MI is most possibly an artifact caused by tracking error close to the aortic valve. The spatial resolution in the circumferential direction is, as seen in Figs. C.7 and C.12, better by 3D speckle tracking than what are achievable using three apical 2D views. This makes it easier to detect small infarctions that do not coincide with the three standard apical views, estimate the area of the affected myocardium, and detect tracking artifacts.

C.4.4 Limitations

The ultrasound simulation simplifies the imaging process by assuming that the beam is focused at each image point. Nonlinear effects, tissue anisotropy, and image artifacts such as side-lobes, reverberations, phase aberrations and acoustic noise are not included in the current simulation model. Furthermore, the effect of gated acquisition and multiple line acquisition is neglected in the model. In the demonstration of the algorithm on human data, the method was applied on a very limited selection of subjects with adequate image quality. Ultrasound data with substantial parts of the LV myocardium outside the imaging volume, with conspicuous drop-outs or reverberations, or ambiguous wall definition due to low signal to noise ratio prohibited inclusion as an example subject. Assessment of feasibility, validity and reliability of the algorithm applied to a general population was beyond the scope of the present study. The pre-tracking of the axial AV-plane displacements assumes a standard apical view, and will not be suitable for views where the predominant AV-plane motion is not in the axial direction.

C.5 Conclusions

A new 3D speckle tracking method for assessment of regional left ventricular function from full-volume ultrasound recordings has been developed. The method was shown to be able to quantify regional myocardial function in simulated ultrasound data and in a selection of example subjects with good image quality, despite the limited temporal resolution offered by the present 4D ultrasound systems.

Strain and rotation estimated by speckle tracking in synthetic ultrasound data showed good agreement with the true motion of the underlying FE model, and was able to capture the position and extent of the MI. The method showed also reasonable traces for strain and rotation when applied to real ultrasound data from a healthy subject. In the two example patients, the strain plots revealed ischemic regions that were consistent with the results by wall motion scoring based on 2D apical images and by coronary angiography.

The tracking and regularization of a complete cardiac cycle takes currently about 4 minutes. This could probably be reduced further, thus, making 3D speckle tracking fast enough for clinical use.

C.6 Acknowledgements

We appreciate the support of Asbjørn Støylen (Department of Circulation and Medical Imaging, Norwegian University of Science and Technology) in performing the wall motion analysis.

References

Amundsen, B., J. Crosby, P. Steen, H. Torp, S. Slørdahl, and A. Støylen (2008). Regional myocardial long-axis strain and strain rate measured by different tissue Doppler and speckle tracking echocardiography methods: a comparison with tagged magnetic resonance imaging. *Eur. J. Echocardiogr.*.

Anderson, M. E. and G. E. Trahey (2006). *A seminar on k-space applied to medical ultrasound*. Duke University: Department of Biomedical Engineering.

Angelini, E., S. Homma, G. Pearson, J. Holmes, and A. Laine (2005). Segmentation of real-time three-dimensional ultrasound for quantification of ventricular function: a clinical study on right and left ventricles. *Ultrasound Med. Biol. 31*, 1143–1158.

Bogaert, J. (2005). *Cardiac Function*, pp. 99–142. Springer.

Brekke, S., S. I. Rabben, A. Haugen, G. U. Haugen, E. N. Steen, and H. G. Torp (2005). Real-time volume stitching in 4D echocardiography. *Proc. IEEE Ultrason. Symp.*, 1228–1231.

Buchalter, M. B., J. L. Weiss, W. J. Rogers, E. A. Zerhouni, M. L. Weisfeldt, R. Beyar, and E. P. Shapiro (1990). Noninvasive quantification of left ventricular rotational deformation in normal humans using magnetic resonance imaging myocardial tagging. *Circulation 81*, 1236–1244.

Cerqueira, M., N. Weissman, V. Dilsizian, A. Jacobs, S. Kaul, W. Laskey, D. Pennell, J. Rumberger, T. Ryan, and M. Verani (2002). Standardized myocardial segmentation and nomenclature for tomographic imaging of the heart: a statement for healthcare professionals from the Cardiac Imaging Committee of the Council on Clinical Cardiology of the American Heart Association. *Circulation 105*, 539–542.

Chen, X., H. Xie, R. Erkamp, K. Kim, C. Jia, J. Rubin, and M. O'Donnell (2005). 3-D correlation-based speckle tracking. *Ultrason. Imaging 27*, 21–36.

Clark, N., N. Reichek, P. Bergey, E. Hoffman, D. Brownson, L. Palmon, and L. Axel (1991). Circumferential myocardial shortening in the normal human left ventricle. Assessment by magnetic resonance imaging using spatial modulation of magnetization. *Circulation 84*, 67–74.

Elen, A., D. Loeckx, H. F. Choi, H. Gao, P. Claus, F. Maes, P. Suetens, and J. D'hooge (2007). Cardiac strain estimation using spatio-temporal elastic registration: In silico validation. *Proc. IEEE Ultrason. Symp.*, 1945–1948.

Geiman, B., L. Bohs, M. Anderson, S. Breit, and G. Trahey (2000). A novel interpolation strategy for estimating subsample speckle motion. *Phys. Med. Biol. 45*, 1541–1552.

Hansegård, J., F. Orderud, and S. I. Rabben (2007). Real-time active shape models for segmentation of 3D cardiac ultrasound. In W. G. Kropatsch, M. Kampel, and A. Hanbury (Eds.), *CAIP*, Volume 4673 of *Lecture Notes in Computer Science*, pp. 157–164. Springer.

Helle-Valle, T., J. Crosby, T. Edvardsen, E. Lyseggen, B. Amundsen, H. Smith, B. Rosen, J. Lima, H. Torp, H. Ihlen, and O. Smiseth (2005). New noninvasive method for assessment of left ventricular rotation: speckle tracking echocardiography. *Circulation 112*, 3149–3156.

Hergum, T., J. Crosby, M. Langhammer, and H. Torp (2006). The effect of including fiber orientation in simulated 3D ultrasound images of the heart. *Proc. IEEE Ultrason. Symp.*, 1991–1994.

Ingul, C., H. Torp, S. Aase, S. Berg, A. Støylen, and S. Slørdahl (2005). Automated analysis of strain rate and strain: Feasibility and clinical implications. *J. Am. Soc. Echocardiogr. 18*, 411–418.

Jensen, J. (2004). Simulation of advanced ultrasound systems using Field II. *Proc. IEEE Biomed. Imaging*, 636–639.

Jia, C., K. Kim, T. J. Kolias, J. M. Rubin, W. F. Weitzel, P. Yan, D. Dione, A. J. Sinusas, J. Duncan, and M. O'Donnell (2007). 4D elasticity imaging of PVA LV phantom integrated with pulsatile circulation system using 2D phased array. *Proc. IEEE Ultrason. Symp.*, 876–879.

Leitman, M., P. Lysyansky, S. Sidenko, V. Shir, E. Peleg, M. Binenbaum, E. Kaluski, R. Krakover, and Z. Vered (2004). Two-dimensional strain - a novel software for real-time quantitative echocardiographic assessment of myocardial function. *J. Am. Soc. Echocardiogr. 17*, 1021–1029.

Meunier, J. (1998). Tissue motion assessment from 3D echographic speckle tracking. *Phys. Med. Biol. 43*(5), 1241–1254.

Meunier, J. and M. Bertrand (1995). Ultrasonic texture motion analysis: Theory and simulation. *IEEE Trans. Med. Imaging 14*(2), 293–300.

Notomi, Y., P. Lysyansky, R. Setser, T. Shiota, Z. Popovic, M. Martin-Miklovic, J. Weaver, S. Oryszak, N. Greenberg, R. White, and J. Thomas (2005). Measurement of ventricular torsion by two-dimensional ultrasound speckle tracking imaging. *J. Am. Coll. Cardiol. 45*, 2034–2041.

Remme, E. W. and O. A. Smiseth (2007). Characteristic strain pattern of moderately ischemic myocardium investigated in a finite element simulation model. In *FIMH*, pp. 330–339.

Schiller, N., P. Shah, M. Crawford, A. DeMaria, R. Devereux, H. Feigenbaum, H. Gutgesell, N. Reichek, D. Sahn, and I. Schnittger (1989). Recommendations for quantitation of the left ventricle by two-dimensional echocardiography.

American Society of Echocardiography Committee on Standards, Subcommittee on Quantitation of Two-Dimensional Echocardiograms. *J. Am. Soc. Echocardiogr. 2*, 358–367.

Serri, K., P. Reant, M. Lafitte, M. Berhouet, V. Le Bouffos, R. Roudaut, and S. Lafitte (2006). Global and regional myocardial function quantification by two-dimensional strain: application in hypertrophic cardiomyopathy. *J. Am. Coll. Cardiol. 47*, 1175–1181.

Song, X., A. Myronenko, and D. J. Sahn (2007). Speckle tracking in 3D echocardiography with motion coherence. In *Computer Vision and Pattern Recognition, 2007. CVPR '07. IEEE Conference on*, Minneapolis, MN, pp. 1–7.

Suffoletto, M., K. Dohi, M. Cannesson, S. Saba, and J. Gorcsan (2006). Novel speckle-tracking radial strain from routine black-and-white echocardiographic images to quantify dyssynchrony and predict response to cardiac resynchronization therapy. *Circulation 113*, 960–968.

Trahey, G. E., S. W. Smith, and O. T. von Ramm (1986). Speckle pattern correlation with lateral aperture translation: Experimental results and implications for spatial compounding. *IEEE Trans. Ultrason. Ferroelectr. Freq. Control 33*(3), 257–264.

von Ramm, O. T., S. W. Smith, and J. Pavy, H. G. (1991). High-speed ultrasound volumetric imaging system. II. Parallelprocessing and image display. *IEEE Trans. Ultrason. Ferroelectr. Freq. Control 38*(2), 109–115.

Walker, W. F. and G. E. Trahey (1998). The application of k-space in pulse echo ultrasound. *IEEE Trans. Ultrason. Ferroelectr. Freq. Control 45*, 541–558.

Westerweel, J. (1993). Digital particle image velocimetry: theory and application.

Yu, W., P. Yan, A. Sinusas, K. Thiele, and J. Duncan (2006). Towards pointwise motion tracking in echocardiographic image sequences–comparing the reliability of different features for speckle tracking. *Med. Image Anal. 10*, 495–508.

Paper D

Is not included due to copyright

Dissertations at the Faculty of Medicine, NTNU

1977

1. Knut Joachim Berg: EFFECT OF ACETYLSALICYLIC ACID ON RENAL FUNCTION
2. Karl Erik Viken and Arne Ødegaard: STUDIES ON HUMAN MONOCYTES CULTURED *IN VITRO*

1978

3. Karel Bjørn Cyvin: CONGENITAL DISLOCATION OF THE HIP JOINT.
4. Alf O. Brubakk: METHODS FOR STUDYING FLOW DYNAMICS IN THE LEFT VENTRICLE AND THE AORTA IN MAN.

1979

5. Geirmund Unsgaard: CYTOSTATIC AND IMMUNOREGULATORY ABILITIES OF HUMAN BLOOD MONOCYTES CULTURED IN VITRO

1980

6. Størker Jørstad: URAEMIC TOXINS
7. Arne Olav Jenssen: SOME RHEOLOGICAL, CHEMICAL AND STRUCTURAL PROPERTIES OF MUCOID SPUTUM FROM PATIENTS WITH CHRONIC OBSTRUCTIVE BRONCHITIS

1981

8. Jens Hammerstrøm: CYTOSTATIC AND CYTOLYTIC ACTIVITY OF HUMAN MONOCYTES AND EFFUSION MACROPHAGES AGAINST TUMOR CELLS *IN VITRO*

1983

9. Tore Syversen: EFFECTS OF METHYLMERCURY ON RAT BRAIN PROTEIN.
10. Torbjørn Iversen: SQUAMOUS CELL CARCINOMA OF THE VULVA.

1984

11. Tor-Erik Widerøe: ASPECTS OF CONTINUOUS AMBULATORY PERITONEAL DIALYSIS.
12. Anton Hole: ALTERATIONS OF MONOCYTE AND LYMPHOCYTE FUNCTIONS IN REALTION TO SURGERY UNDER EPIDURAL OR GENERAL ANAESTHESIA.
13. Terje Terjesen: FRACTURE HEALING AND STRESS-PROTECTION AFTER METAL PLATE FIXATION AND EXTERNAL FIXATION.
14. Carsten Saunte: CLUSTER HEADACHE SYNDROME.
15. Inggard Lereim: TRAFFIC ACCIDENTS AND THEIR CONSEQUENCES.
16. Bjørn Magne Eggen: STUDIES IN CYTOTOXICITY IN HUMAN ADHERENT MONONUCLEAR BLOOD CELLS.
17. Trond Haug: FACTORS REGULATING BEHAVIORAL EFFECTS OG DRUGS.

1985

18. Sven Erik Gisvold: RESUSCITATION AFTER COMPLETE GLOBAL BRAIN ISCHEMIA.
19. Terje Espevik: THE CYTOSKELETON OF HUMAN MONOCYTES.
20. Lars Bevanger: STUDIES OF THE Ibc (c) PROTEIN ANTIGENS OF GROUP B STREPTOCOCCI.
21. Ole-Jan Iversen: RETROVIRUS-LIKE PARTICLES IN THE PATHOGENESIS OF PSORIASIS.
22. Lasse Eriksen: EVALUATION AND TREATMENT OF ALCOHOL DEPENDENT BEHAVIOUR.
23. Per I. Lundmo: ANDROGEN METABOLISM IN THE PROSTATE.

1986

24. Dagfinn Berntzen: ANALYSIS AND MANAGEMENT OF EXPERIMENTAL AND CLINICAL PAIN.
25. Odd Arnold Kildahl-Andersen: PRODUCTION AND CHARACTERIZATION OF MONOCYTE-DERIVED CYTOTOXIN AND ITS ROLE IN MONOCYTE-MEDIATED CYTOTOXICITY.
26. Ola Dale: VOLATILE ANAESTHETICS.

1987

27. Per Martin Kleveland: STUDIES ON GASTRIN.
28. Audun N. Øksendal: THE CALCIUM PARADOX AND THE HEART.
29. Vilhjalmur R. Finsen: HIP FRACTURES

1988

30. Rigmor Austgulen: TUMOR NECROSIS FACTOR: A MONOCYTE-DERIVED REGULATOR OF CELLULAR GROWTH.
31. Tom-Harald Edna: HEAD INJURIES ADMITTED TO HOSPITAL.
32. Joseph D. Borsi: NEW ASPECTS OF THE CLINICAL PHARMACOKINETICS OF METHOTREXATE.
33. Olav F. M. Sellevold: GLUCOCORTICOIDS IN MYOCARDIAL PROTECTION.
34. Terje Skjærpe: NONINVASIVE QUANTITATION OF GLOBAL PARAMETERS ON LEFT VENTRICULAR FUNCTION: THE SYSTOLIC PULMONARY ARTERY PRESSURE AND CARDIAC OUTPUT.
35. Eyvind Rødahl: STUDIES OF IMMUNE COMPLEXES AND RETROVIRUS-LIKE ANTIGENS IN PATIENTS WITH ANKYLOSING SPONDYLITIS.
36. Ketil Thorstensen: STUDIES ON THE MECHANISMS OF CELLULAR UPTAKE OF IRON FROM TRANSFERRIN.
37. Anna Midelfart: STUDIES OF THE MECHANISMS OF ION AND FLUID TRANSPORT IN THE BOVINE CORNEA.
38. Eirik Helseth: GROWTH AND PLASMINOGEN ACTIVATOR ACTIVITY OF HUMAN GLIOMAS AND BRAIN METASTASES - WITH SPECIAL REFERENCE TO TRANSFORMING GROWTH FACTOR BETA AND THE EPIDERMAL GROWTH FACTOR RECEPTOR.
39. Petter C. Borchgrevink: MAGNESIUM AND THE ISCHEMIC HEART.
40. Kjell-Arne Rein: THE EFFECT OF EXTRACORPOREAL CIRCULATION ON SUBCUTANEOUS TRANSCAPILLARY FLUID BALANCE.
41. Arne Kristian Sandvik: RAT GASTRIC HISTAMINE.
42. Carl Bredo Dahl: ANIMAL MODELS IN PSYCHIATRY.

1989

43. Torbjørn A. Fredriksen: CERVICOGENIC HEADACHE.
44. Rolf A. Walstad: CEFTAZIDIME.
45. Rolf Salvesen: THE PUPIL IN CLUSTER HEADACHE.
46. Nils Petter Jørgensen: DRUG EXPOSURE IN EARLY PREGNANCY.
47. Johan C. Ræder: PREMEDICATION AND GENERAL ANAESTHESIA IN OUTPATIENT GYNECOLOGICAL SURGERY.
48. M. R. Shalaby: IMMUNOREGULATORY PROPERTIES OF TNF-α AND THE RELATED CYTOKINES.
49. Anders Waage: THE COMPLEX PATTERN OF CYTOKINES IN SEPTIC SHOCK.
50. Bjarne Christian Eriksen: ELECTROSTIMULATION OF THE PELVIC FLOOR IN FEMALE URINARY INCONTINENCE.
51. Tore B. Halvorsen: PROGNOSTIC FACTORS IN COLORECTAL CANCER.

1990

52. Asbjørn Nordby: CELLULAR TOXICITY OF ROENTGEN CONTRAST MEDIA.
53. Kåre E. Tvedt: X-RAY MICROANALYSIS OF BIOLOGICAL MATERIAL.
54. Tore C. Stiles: COGNITIVE VULNERABILITY FACTORS IN THE DEVELOPMENT AND MAINTENANCE OF DEPRESSION.
55. Eva Hofsli: TUMOR NECROSIS FACTOR AND MULTIDRUG RESISTANCE.
56. Helge S. Haarstad: TROPHIC EFFECTS OF CHOLECYSTOKININ AND SECRETIN ON THE RAT PANCREAS.
57. Lars Engebretsen: TREATMENT OF ACUTE ANTERIOR CRUCIATE LIGAMENT INJURIES.
58. Tarjei Rygnestad: DELIBERATE SELF-POISONING IN TRONDHEIM.
59. Arne Z. Henriksen: STUDIES ON CONSERVED ANTIGENIC DOMAINS ON MAJOR OUTER MEMBRANE PROTEINS FROM ENTEROBACTERIA.
60. Steinar Westin: UNEMPLOYMENT AND HEALTH: Medical and social consequences of a factory closure in a ten-year controlled follow-up study.
61. Ylva Sahlin: INJURY REGISTRATION, a tool for accident preventive work.
62. Helge Bjørnstad Pettersen: BIOSYNTHESIS OF COMPLEMENT BY HUMAN ALVEOLAR MACROPHAGES WITH SPECIAL REFERENCE TO SARCOIDOSIS.
63. Berit Schei: TRAPPED IN PAINFUL LOVE.
64. Lars J. Vatten: PROSPECTIVE STUDIES OF THE RISK OF BREAST CANCER IN A COHORT OF NORWEGIAN WOMAN.

1991

65. Kåre Bergh: APPLICATIONS OF ANTI-C5a SPECIFIC MONOCLONAL ANTIBODIES FOR THE ASSESSMENT OF COMPLEMENT ACTIVATION.
66. Svein Svenningsen: THE CLINICAL SIGNIFICANCE OF INCREASED FEMORAL ANTEVERSION.
67. Olbjørn Klepp: NONSEMINOMATOUS GERM CELL TESTIS CANCER: THERAPEUTIC OUTCOME AND PROGNOSTIC FACTORS.
68. Trond Sand: THE EFFECTS OF CLICK POLARITY ON BRAINSTEM AUDITORY EVOKED POTENTIALS AMPLITUDE, DISPERSION, AND LATENCY VARIABLES.
69. Kjetil B. Åsbakk: STUDIES OF A PROTEIN FROM PSORIATIC SCALE, PSO P27, WITH RESPECT TO ITS POTENTIAL ROLE IN IMMUNE REACTIONS IN PSORIASIS.
70. Arnulf Hestnes: STUDIES ON DOWN'S SYNDROME.
71. Randi Nygaard: LONG-TERM SURVIVAL IN CHILDHOOD LEUKEMIA.
72. Bjørn Hagen: THIO-TEPA.
73. Svein Anda: EVALUATION OF THE HIP JOINT BY COMPUTED TOMOGRAMPHY AND ULTRASONOGRAPHY.

1992

74. Martin Svartberg: AN INVESTIGATION OF PROCESS AND OUTCOME OF SHORT-TERM PSYCHODYNAMIC PSYCHOTHERAPY.
75. Stig Arild Slørdahl: AORTIC REGURGITATION.
76. Harold C Sexton: STUDIES RELATING TO THE TREATMENT OF SYMPTOMATIC NON-PSYCHOTIC PATIENTS.
77. Maurice B. Vincent: VASOACTIVE PEPTIDES IN THE OCULAR/FOREHEAD AREA.
78. Terje Johannessen: CONTROLLED TRIALS IN SINGLE SUBJECTS.
79. Turid Nilsen: PYROPHOSPHATE IN HEPATOCYTE IRON METABOLISM.
80. Olav Haraldseth: NMR SPECTROSCOPY OF CEREBRAL ISCHEMIA AND REPERFUSION IN RAT.
81. Eiliv Brenna: REGULATION OF FUNCTION AND GROWTH OF THE OXYNTIC MUCOSA.

1993

82. Gunnar Bovim: CERVICOGENIC HEADACHE.
83. Jarl Arne Kahn: ASSISTED PROCREATION.
84. Bjørn Naume: IMMUNOREGULATORY EFFECTS OF CYTOKINES ON NK CELLS.
85. Rune Wiseth: AORTIC VALVE REPLACEMENT.
86. Jie Ming Shen: BLOOD FLOW VELOCITY AND RESPIRATORY STUDIES.
87. Piotr Kruszewski: SUNCT SYNDROME WITH SPECIAL REFERENCE TO THE AUTONOMIC NERVOUS SYSTEM.
88. Mette Haase Moen: ENDOMETRIOSIS.
89. Anne Vik: VASCULAR GAS EMBOLISM DURING AIR INFUSION AND AFTER DECOMPRESSION IN PIGS.
90. Lars Jacob Stovner: THE CHIARI TYPE I MALFORMATION.
91. Kjell Å. Salvesen: ROUTINE ULTRASONOGRAPHY IN UTERO AND DEVELOPMENT IN CHILDHOOD.

1994

92. Nina-Beate Liabakk: DEVELOPMENT OF IMMUNOASSAYS FOR TNF AND ITS SOLUBLE RECEPTORS.
93. Sverre Helge Torp: *erb*B ONCOGENES IN HUMAN GLIOMAS AND MENINGIOMAS.
94. Olav M. Linaker: MENTAL RETARDATION AND PSYCHIATRY. Past and present.
95. Per Oscar Feet: INCREASED ANTIDEPRESSANT AND ANTIPANIC EFFECT IN COMBINED TREATMENT WITH DIXYRAZINE AND TRICYCLIC ANTIDEPRESSANTS.
96. Stein Olav Samstad: CROSS SECTIONAL FLOW VELOCITY PROFILES FROM TWO-DIMENSIONAL DOPPLER ULTRASOUND: Studies on early mitral blood flow.
97. Bjørn Backe: STUDIES IN ANTENATAL CARE.
98. Gerd Inger Ringdal: QUALITY OF LIFE IN CANCER PATIENTS.
99. Torvid Kiserud: THE DUCTUS VENOSUS IN THE HUMAN FETUS.
100. Hans E. Fjøsne: HORMONAL REGULATION OF PROSTATIC METABOLISM.
101. Eylert Brodtkorb: CLINICAL ASPECTS OF EPILEPSY IN THE MENTALLY RETARDED.
102. Roar Juul: PEPTIDERGIC MECHANISMS IN HUMAN SUBARACHNOID HEMORRHAGE.
103. Unni Syversen: CHROMOGRANIN A. Phsysiological and Clinical Role.

1995

104. Odd Gunnar Brakstad: THERMOSTABLE NUCLEASE AND THE *nuc* GENE IN THE DIAGNOSIS OF *Staphylococcus aureus* INFECTIONS.
105. Terje Engan: NUCLEAR MAGNETIC RESONANCE (NMR) SPECTROSCOPY OF PLASMA IN MALIGNANT DISEASE.
106. Kirsten Rasmussen: VIOLENCE IN THE MENTALLY DISORDERED.
107. Finn Egil Skjeldestad: INDUCED ABORTION: Timetrends and Determinants.
108. Roar Stenseth: THORACIC EPIDURAL ANALGESIA IN AORTOCORONARY BYPASS SURGERY.
109. Arild Faxvaag: STUDIES OF IMMUNE CELL FUNCTION *in mice infected with* MURINE RETROVIRUS.

1996

110. Svend Aakhus: NONINVASIVE COMPUTERIZED ASSESSMENT OF LEFT VENTRICULAR FUNCTION AND SYSTEMIC ARTERIAL PROPERTIES. Methodology and some clinical applications.
111. Klaus-Dieter Bolz: INTRAVASCULAR ULTRASONOGRAPHY.
112. Petter Aadahl: CARDIOVASCULAR EFFECTS OF THORACIC AORTIC CROSS-CLAMPING.
113. Sigurd Steinshamn: CYTOKINE MEDIATORS DURING GRANULOCYTOPENIC INFECTIONS.
114. Hans Stifoss-Hanssen: SEEKING MEANING OR HAPPINESS?
115. Anne Kvikstad: LIFE CHANGE EVENTS AND MARITAL STATUS IN RELATION TO RISK AND PROGNOSIS OF CANCER.
116. Torbjørn Grøntvedt: TREATMENT OF ACUTE AND CHRONIC ANTERIOR CRUCIATE LIGAMENT INJURIES. A clinical and biomechanical study.
117. Sigrid Hørven Wigers: CLINICAL STUDIES OF FIBROMYALGIA WITH FOCUS ON ETIOLOGY, TREATMENT AND OUTCOME.
118. Jan Schjøtt: MYOCARDIAL PROTECTION: Functional and Metabolic Characteristics of Two Endogenous Protective Principles.
119. Marit Martinussen: STUDIES OF INTESTINAL BLOOD FLOW AND ITS RELATION TO TRANSITIONAL CIRCULATORY ADAPATION IN NEWBORN INFANTS.
120. Tomm B. Müller: MAGNETIC RESONANCE IMAGING IN FOCAL CEREBRAL ISCHEMIA.
121. Rune Haaverstad: OEDEMA FORMATION OF THE LOWER EXTREMITIES.
122. Magne Børset: THE ROLE OF CYTOKINES IN MULTIPLE MYELOMA, WITH SPECIAL REFERENCE TO HEPATOCYTE GROWTH FACTOR.
123. Geir Smedslund: A THEORETICAL AND EMPIRICAL INVESTIGATION OF SMOKING, STRESS AND DISEASE: RESULTS FROM A POPULATION SURVEY.

1997

124. Torstein Vik: GROWTH, MORBIDITY, AND PSYCHOMOTOR DEVELOPMENT IN INFANTS WHO WERE GROWTH RETARDED *IN UTERO*.
125. Siri Forsmo: ASPECTS AND CONSEQUENCES OF OPPORTUNISTIC SCREENING FOR CERVICAL CANCER. Results based on data from three Norwegian counties.
126. Jon S. Skranes: CEREBRAL MRI AND NEURODEVELOPMENTAL OUTCOME IN VERY LOW BIRTH WEIGHT (VLBW) CHILDREN. A follow-up study of a geographically based year cohort of VLBW children at ages one and six years.
127. Knut Bjørnstad: COMPUTERIZED ECHOCARDIOGRAPHY FOR EVALUTION OF CORONARY ARTERY DISEASE.
128. Grethe Elisabeth Borchgrevink: DIAGNOSIS AND TREATMENT OF WHIPLASH/NECK SPRAIN INJURIES CAUSED BY CAR ACCIDENTS.
129. Tor Elsås: NEUROPEPTIDES AND NITRIC OXIDE SYNTHASE IN OCULAR AUTONOMIC AND SENSORY NERVES.
130. Rolf W. Gråwe: EPIDEMIOLOGICAL AND NEUROPSYCHOLOGICAL PERSPECTIVES ON SCHIZOPHRENIA.
131. Tonje Strømholm: CEREBRAL HAEMODYNAMICS DURING THORACIC AORTIC CROSSCLAMPING. An experimental study in pigs.

1998

132. Martinus Bråten: STUDIES ON SOME PROBLEMS REALTED TO INTRAMEDULLARY NAILING OF FEMORAL FRACTURES.
133. Ståle Nordgård: PROLIFERATIVE ACTIVITY AND DNA CONTENT AS PROGNOSTIC INDICATORS IN ADENOID CYSTIC CARCINOMA OF THE HEAD AND NECK.

134. Egil Lien: SOLUBLE RECEPTORS FOR **TNF** AND **LPS**: RELEASE PATTERN AND POSSIBLE SIGNIFICANCE IN DISEASE.
135. Marit Bjørgaas: HYPOGLYCAEMIA IN CHILDREN WITH DIABETES MELLITUS
136. Frank Skorpen: GENETIC AND FUNCTIONAL ANALYSES OF DNA REPAIR IN HUMAN CELLS.
137. Juan A. Pareja: SUNCT SYNDROME. ON THE CLINICAL PICTURE. ITS DISTINCTION FROM OTHER, SIMILAR HEADACHES.
138. Anders Angelsen: NEUROENDOCRINE CELLS IN HUMAN PROSTATIC CARCINOMAS AND THE PROSTATIC COMPLEX OF RAT, GUINEA PIG, CAT AND DOG.
139. Fabio Antonaci: CHRONIC PAROXYSMAL HEMICRANIA AND HEMICRANIA CONTINUA: TWO DIFFERENT ENTITIES?
140. Sven M. Carlsen: ENDOCRINE AND METABOLIC EFFECTS OF METFORMIN WITH SPECIAL EMPHASIS ON CARDIOVASCULAR RISK FACTORES.

1999

141. Terje A. Murberg: DEPRESSIVE SYMPTOMS AND COPING AMONG PATIENTS WITH CONGESTIVE HEART FAILURE.
142. Harm-Gerd Karl Blaas: THE EMBRYONIC EXAMINATION. Ultrasound studies on the development of the human embryo.
143. Noèmi Becser Andersen: THE CEPHALIC SENSORY NERVES IN UNILATERAL HEADACHES. Anatomical background and neurophysiological evaluation.
144. Eli-Janne Fiskerstrand: LASER TREATMENT OF PORT WINE STAINS. A study of the efficacy and limitations of the pulsed dye laser. Clinical and morfological analyses aimed at improving the therapeutic outcome.
145. Bård Kulseng: A STUDY OF ALGINATE CAPSULE PROPERTIES AND CYTOKINES IN RELATION TO INSULIN DEPENDENT DIABETES MELLITUS.
146. Terje Haug: STRUCTURE AND REGULATION OF THE HUMAN UNG GENE ENCODING URACIL-DNA GLYCOSYLASE.
147. Heidi Brurok: MANGANESE AND THE HEART. A Magic Metal with Diagnostic and Therapeutic Possibilites.
148. Agnes Kathrine Lie: DIAGNOSIS AND PREVALENCE OF HUMAN PAPILLOMAVIRUS INFECTION IN CERVICAL INTRAEPITELIAL NEOPLASIA. Relationship to Cell Cycle Regulatory Proteins and HLA DQBI Genes.
149. Ronald Mårvik: PHARMACOLOGICAL, PHYSIOLOGICAL AND PATHOPHYSIOLOGICAL STUDIES ON ISOLATED STOMACS.
150. Ketil Jarl Holen: THE ROLE OF ULTRASONOGRAPHY IN THE DIAGNOSIS AND TREATMENT OF HIP DYSPLASIA IN NEWBORNS.
151. Irene Hetlevik: THE ROLE OF CLINICAL GUIDELINES IN CARDIOVASCULAR RISK INTERVENTION IN GENERAL PRACTICE.
152. Katarina Tunòn: ULTRASOUND AND PREDICTION OF GESTATIONAL AGE.
153. Johannes Soma: INTERACTION BETWEEN THE LEFT VENTRICLE AND THE SYSTEMIC ARTERIES.
154. Arild Aamodt: DEVELOPMENT AND PRE-CLINICAL EVALUATION OF A CUSTOM-MADE FEMORAL STEM.
155. Agnar Tegnander: DIAGNOSIS AND FOLLOW-UP OF CHILDREN WITH SUSPECTED OR KNOWN HIP DYSPLASIA.
156. Bent Indredavik: STROKE UNIT TREATMENT: SHORT AND LONG-TERM EFFECTS
157. Jolanta Vanagaite Vingen: PHOTOPHOBIA AND PHONOPHOBIA IN PRIMARY HEADACHES

2000

158. Ola Dalsegg Sæther: PATHOPHYSIOLOGY DURING PROXIMAL AORTIC CROSS-CLAMPING CLINICAL AND EXPERIMENTAL STUDIES
159. xxxxxxxxx (blind number)
160. Christina Vogt Isaksen: PRENATAL ULTRASOUND AND POSTMORTEM FINDINGS – A TEN YEAR CORRELATIVE STUDY OF FETUSES AND INFANTS WITH DEVELOPMENTAL ANOMALIES.
161. Holger Seidel: HIGH-DOSE METHOTREXATE THERAPY IN CHILDREN WITH ACUTE LYMPHOCYTIC LEUKEMIA: DOSE, CONCENTRATION, AND EFFECT CONSIDERATIONS.
162. Stein Hallan: IMPLEMENTATION OF MODERN MEDICAL DECISION ANALYSIS INTO CLINICAL DIAGNOSIS AND TREATMENT.

163. Malcolm Sue-Chu: INVASIVE AND NON-INVASIVE STUDIES IN CROSS-COUNTRY SKIERS WITH ASTHMA-LIKE SYMPTOMS.
164. Ole-Lars Brekke: EFFECTS OF ANTIOXIDANTS AND FATTY ACIDS ON TUMOR NECROSIS FACTOR-INDUCED CYTOTOXICITY.
165. Jan Lundbom: AORTOCORONARY BYPASS SURGERY: CLINICAL ASPECTS, COST CONSIDERATIONS AND WORKING ABILITY.
166. John-Anker Zwart: LUMBAR NERVE ROOT COMPRESSION, BIOCHEMICAL AND NEUROPHYSIOLOGICAL ASPECTS.
167. Geir Falck: HYPEROSMOLALITY AND THE HEART.
168. Eirik Skogvoll: CARDIAC ARREST Incidence, Intervention and Outcome.
169. Dalius Bansevicius: SHOULDER-NECK REGION IN CERTAIN HEADACHES AND CHRONIC PAIN SYNDROMES.
170. Bettina Kinge: REFRACTIVE ERRORS AND BIOMETRIC CHANGES AMONG UNIVERSITY STUDENTS IN NORWAY.
171. Gunnar Qvigstad: CONSEQUENCES OF HYPERGASTRINEMIA IN MAN
172. Hanne Ellekjær: EPIDEMIOLOGICAL STUDIES OF STROKE IN A NORWEGIAN POPULATION. INCIDENCE, RISK FACTORS AND PROGNOSIS
173. Hilde Grimstad: VIOLENCE AGAINST WOMEN AND PREGNANCY OUTCOME.
174. Astrid Hjelde: SURFACE TENSION AND COMPLEMENT ACTIVATION: Factors influencing bubble formation and bubble effects after decompression.
175. Kjell A. Kvistad: MR IN BREAST CANCER – A CLINICAL STUDY.
176. Ivar Rossvoll: ELECTIVE ORTHOPAEDIC SURGERY IN A DEFINED POPULATION. Studies on demand, waiting time for treatment and incapacity for work.
177. Carina Seidel: PROGNOSTIC VALUE AND BIOLOGICAL EFFECTS OF HEPATOCYTE GROWTH FACTOR AND SYNDECAN-1 IN MULTIPLE MYELOMA.

2001

178. Alexander Wahba: THE INFLUENCE OF CARDIOPULMONARY BYPASS ON PLATELET FUNCTION AND BLOOD COAGULATION – DETERMINANTS AND CLINICAL CONSEQUENSES
179. Marcus Schmitt-Egenolf: THE RELEVANCE OF THE MAJOR hISTOCOMPATIBILITY COMPLEX FOR THE GENETICS OF PSORIASIS
180. Odrun Arna Gederaas: BIOLOGICAL MECHANISMS INVOLVED IN 5-AMINOLEVULINIC ACID BASED PHOTODYNAMIC THERAPY
181. Pål Richard Romundstad: CANCER INCIDENCE AMONG NORWEGIAN ALUMINIUM WORKERS
182. Henrik Hjorth-Hansen: NOVEL CYTOKINES IN GROWTH CONTROL AND BONE DISEASE OF MULTIPLE MYELOMA
183. Gunnar Morken: SEASONAL VARIATION OF HUMAN MOOD AND BEHAVIOUR
184. Bjørn Olav Haugen: MEASUREMENT OF CARDIAC OUTPUT AND STUDIES OF VELOCITY PROFILES IN AORTIC AND MITRAL FLOW USING TWO- AND THREE-DIMENSIONAL COLOUR FLOW IMAGING
185. Geir Bråthen: THE CLASSIFICATION AND CLINICAL DIAGNOSIS OF ALCOHOL-RELATED SEIZURES
186. Knut Ivar Aasarød: RENAL INVOLVEMENT IN INFLAMMATORY RHEUMATIC DISEASE. A Study of Renal Disease in Wegener's Granulomatosis and in Primary Sjögren's Syndrome
187. Trude Helen Flo: RESEPTORS INVOLVED IN CELL ACTIVATION BY DEFINED URONIC ACID POLYMERS AND BACTERIAL COMPONENTS
188. Bodil Kavli: HUMAN URACIL-DNA GLYCOSYLASES FROM THE UNG GENE: STRUCTRUAL BASIS FOR SUBSTRATE SPECIFICITY AND REPAIR
189. Liv Thommesen: MOLECULAR MECHANISMS INVOLVED IN TNF- AND GASTRIN-MEDIATED GENE REGULATION
190. Turid Lingaas Holmen: SMOKING AND HEALTH IN ADOLESCENCE; THE NORD-TRØNDELAG HEALTH STUDY, 1995-97
191. Øyvind Hjertner: MULTIPLE MYELOMA: INTERACTIONS BETWEEN MALIGNANT PLASMA CELLS AND THE BONE MICROENVIRONMENT
192. Asbjørn Støylen: STRAIN RATE IMAGING OF THE LEFT VENTRICLE BY ULTRASOUND. FEASIBILITY, CLINICAL VALIDATION AND PHYSIOLOGICAL ASPECTS

193. Kristian Midthjell: DIABETES IN ADULTS IN NORD-TRØNDELAG. PUBLIC HEALTH ASPECTS OF DIABETES MELLITUS IN A LARGE, NON-SELECTED NORWEGIAN POPULATION.
194. Guanglin Cui: FUNCTIONAL ASPECTS OF THE ECL CELL IN RODENTS
195. Ulrik Wisløff: CARDIAC EFFECTS OF AEROBIC ENDURANCE TRAINING: HYPERTROPHY, CONTRACTILITY AND CALCUIM HANDLING IN NORMAL AND FAILING HEART
196. Øyvind Halaas: MECHANISMS OF IMMUNOMODULATION AND CELL-MEDIATED CYTOTOXICITY INDUCED BY BACTERIAL PRODUCTS
197. Tore Amundsen: PERFUSION MR IMAGING IN THE DIAGNOSIS OF PULMONARY EMBOLISM
198. Nanna Kurtze: THE SIGNIFICANCE OF ANXIETY AND DEPRESSION IN FATIQUE AND PATTERNS OF PAIN AMONG INDIVIDUALS DIAGNOSED WITH FIBROMYALGIA: RELATIONS WITH QUALITY OF LIFE, FUNCTIONAL DISABILITY, LIFESTYLE, EMPLOYMENT STATUS, CO-MORBIDITY AND GENDER
199. Tom Ivar Lund Nilsen: PROSPECTIVE STUDIES OF CANCER RISK IN NORD-TRØNDELAG: THE HUNT STUDY. Associations with anthropometric, socioeconomic, and lifestyle risk factors
200. Asta Kristine Håberg: A NEW APPROACH TO THE STUDY OF MIDDLE CEREBRAL ARTERY OCCLUSION IN THE RAT USING MAGNETIC RESONANCE TECHNIQUES

2002

201. Knut Jørgen Arntzen: PREGNANCY AND CYTOKINES
202. Henrik Døllner: INFLAMMATORY MEDIATORS IN PERINATAL INFECTIONS
203. Asta Bye: LOW FAT, LOW LACTOSE DIET USED AS PROPHYLACTIC TREATMENT OF ACUTE INTESTINAL REACTIONS DURING PELVIC RADIOTHERAPY. A PROSPECTIVE RANDOMISED STUDY.
204. Sylvester Moyo: STUDIES ON STREPTOCOCCUS AGALACTIAE (GROUP B STREPTOCOCCUS) SURFACE-ANCHORED MARKERS WITH EMPHASIS ON STRAINS AND HUMAN SERA FROM ZIMBABWE.
205. Knut Hagen: HEAD-HUNT: THE EPIDEMIOLOGY OF HEADACHE IN NORD-TRØNDELAG
206. Li Lixin: ON THE REGULATION AND ROLE OF UNCOUPLING PROTEIN-2 IN INSULIN PRODUCING ß-CELLS
207. Anne Hildur Henriksen: SYMPTOMS OF ALLERGY AND ASTHMA VERSUS MARKERS OF LOWER AIRWAY INFLAMMATION AMONG ADOLESCENTS
208. Egil Andreas Fors: NON-MALIGNANT PAIN IN RELATION TO PSYCHOLOGICAL AND ENVIRONTENTAL FACTORS. EXPERIENTAL AND CLINICAL STUDES OF PAIN WITH FOCUS ON FIBROMYALGIA
209. Pål Klepstad: MORPHINE FOR CANCER PAIN
210. Ingunn Bakke: MECHANISMS AND CONSEQUENCES OF PEROXISOME PROLIFERATOR-INDUCED HYPERFUNCTION OF THE RAT GASTRIN PRODUCING CELL
211. Ingrid Susann Gribbestad: MAGNETIC RESONANCE IMAGING AND SPECTROSCOPY OF BREAST CANCER
212. Rønnaug Astri Ødegård: PREECLAMPSIA – MATERNAL RISK FACTORS AND FETAL GROWTH
213. Johan Haux: STUDIES ON CYTOTOXICITY INDUCED BY HUMAN NATURAL KILLER CELLS AND DIGITOXIN
214. Turid Suzanne Berg-Nielsen: PARENTING PRACTICES AND MENTALLY DISORDERED ADOLESCENTS
215. Astrid Rydning: BLOOD FLOW AS A PROTECTIVE FACTOR FOR THE STOMACH MUCOSA. AN EXPERIMENTAL STUDY ON THE ROLE OF MAST CELLS AND SENSORY AFFERENT NEURONS

2003

216. Jan Pål Loennechen: HEART FAILURE AFTER MYOCARDIAL INFARCTION. Regional Differences, Myocyte Function, Gene Expression, and Response to Cariporide, Losartan, and Exercise Training.
217. Elisabeth Qvigstad: EFFECTS OF FATTY ACIDS AND OVER-STIMULATION ON INSULIN SECRETION IN MAN

218. Arne Åsberg: EPIDEMIOLOGICAL STUDIES IN HEREDITARY HEMOCHROMATOSIS: PREVALENCE, MORBIDITY AND BENEFIT OF SCREENING.
219. Johan Fredrik Skomsvoll: REPRODUCTIVE OUTCOME IN WOMEN WITH RHEUMATIC DISEASE. A population registry based study of the effects of inflammatory rheumatic disease and connective tissue disease on reproductive outcome in Norwegian women in 1967-1995.
220. Siv Mørkved: URINARY INCONTINENCE DURING PREGNANCY AND AFTER DELIVERY: EFFECT OF PELVIC FLOOR MUSCLE TRAINING IN PREVENTION AND TREATMENT
221. Marit S. Jordhøy: THE IMPACT OF COMPREHENSIVE PALLIATIVE CARE
222. Tom Christian Martinsen: HYPERGASTRINEMIA AND HYPOACIDITY IN RODENTS – CAUSES AND CONSEQUENCES
223. Solveig Tingulstad: CENTRALIZATION OF PRIMARY SURGERY FOR OVARAIN CANCER. FEASIBILITY AND IMPACT ON SURVIVAL
224. Haytham Eloqayli: METABOLIC CHANGES IN THE BRAIN CAUSED BY EPILEPTIC SEIZURES
225. Torunn Bruland: STUDIES OF EARLY RETROVIRUS-HOST INTERACTIONS – VIRAL DETERMINANTS FOR PATHOGENESIS AND THE INFLUENCE OF SEX ON THE SUSCEPTIBILITY TO FRIEND MURINE LEUKAEMIA VIRUS INFECTION
226. Torstein Hole: DOPPLER ECHOCARDIOGRAPHIC EVALUATION OF LEFT VENTRICULAR FUNCTION IN PATIENTS WITH ACUTE MYOCARDIAL INFARCTION
227. Vibeke Nossum: THE EFFECT OF VASCULAR BUBBLES ON ENDOTHELIAL FUNCTION
228. Sigurd Fasting: ROUTINE BASED RECORDING OF ADVERSE EVENTS DURING ANAESTHESIA – APPLICATION IN QUALITY IMPROVEMENT AND SAFETY
229. Solfrid Romundstad: EPIDEMIOLOGICAL STUDIES OF MICROALBUMINURIA. THE NORD-TRØNDELAG HEALTH STUDY 1995-97 (HUNT 2)
230. Geir Torheim: PROCESSING OF DYNAMIC DATA SETS IN MAGNETIC RESONANCE IMAGING
231. Catrine Ahlén: SKIN INFECTIONS IN OCCUPATIONAL SATURATION DIVERS IN THE NORTH SEA AND THE IMPACT OF THE ENVIRONMENT
232. Arnulf Langhammer: RESPIRATORY SYMPTOMS, LUNG FUNCTION AND BONE MINERAL DENSITY IN A COMPREHENSIVE POPULATION SURVEY. THE NORD-TRØNDELAG HEALTH STUDY 1995-97. THE BRONCHIAL OBSTRUCTION IN NORD-TRØNDELAG STUDY
233. Einar Kjelsås: EATING DISORDERS AND PHYSICAL ACTIVITY IN NON-CLINICAL SAMPLES
234. Arne Wibe: RECTAL CANCER TREATMENT IN NORWAY – STANDARDISATION OF SURGERY AND QUALITY ASSURANCE

2004

235. Eivind Witsø: BONE GRAFT AS AN ANTIBIOTIC CARRIER
236. Anne Mari Sund: DEVELOPMENT OF DEPRESSIVE SYMPTOMS IN EARLY ADOLESCENCE
237. Hallvard Lærum: EVALUATION OF ELECTRONIC MEDICAL RECORDS – A CLINICAL TASK PERSPECTIVE
238. Gustav Mikkelsen: ACCESSIBILITY OF INFORMATION IN ELECTRONIC PATIENT RECORDS; AN EVALUATION OF THE ROLE OF DATA QUALITY
239. Steinar Krokstad: SOCIOECONOMIC INEQUALITIES IN HEALTH AND DISABILITY. SOCIAL EPIDEMIOLOGY IN THE NORD-TRØNDELAG HEALTH STUDY (HUNT), NORWAY
240. Arne Kristian Myhre: NORMAL VARIATION IN ANOGENITAL ANATOMY AND MICROBIOLOGY IN NON-ABUSED PRESCHOOL CHILDREN
241. Ingunn Dybedal: NEGATIVE REGULATORS OF HEMATOPOIETEC STEM AND PROGENITOR CELLS
242. Beate Sitter: TISSUE CHARACTERIZATION BY HIGH RESOLUTION MAGIC ANGLE SPINNING MR SPECTROSCOPY
243. Per Arne Aas: MACROMOLECULAR MAINTENANCE IN HUMAN CELLS – REPAIR OF URACIL IN DNA AND METHYLATIONS IN DNA AND RNA
244. Anna Bofin: FINE NEEDLE ASPIRATION CYTOLOGY IN THE PRIMARY INVESTIGATION OF BREAST TUMOURS AND IN THE DETERMINATION OF TREATMENT STRATEGIES

245. Jim Aage Nøttestad: DEINSTITUTIONALIZATION AND MENTAL HEALTH CHANGES AMONG PEOPLE WITH MENTAL RETARDATION
246. Reidar Fossmark: GASTRIC CANCER IN JAPANESE COTTON RATS
247. Wibeke Nordhøy: MANGANESE AND THE HEART, INTRACELLULAR MR RELAXATION AND WATER EXCHANGE ACROSS THE CARDIAC CELL MEMBRANE

2005

248. Sturla Molden: QUANTITATIVE ANALYSES OF SINGLE UNITS RECORDED FROM THE HIPPOCAMPUS AND ENTORHINAL CORTEX OF BEHAVING RATS
249. Wenche Brenne Drøyvold: EPIDEMIOLOGICAL STUDIES ON WEIGHT CHANGE AND HEALTH IN A LARGE POPULATION. THE NORD-TRØNDELAG HEALTH STUDY (HUNT)
250. Ragnhild Støen: ENDOTHELIUM-DEPENDENT VASODILATION IN THE FEMORAL ARTERY OF DEVELOPING PIGLETS
251. Aslak Steinsbekk: HOMEOPATHY IN THE PREVENTION OF UPPER RESPIRATORY TRACT INFECTIONS IN CHILDREN
252. Hill-Aina Steffenach: MEMORY IN HIPPOCAMPAL AND CORTICO-HIPPOCAMPAL CIRCUITS
253. Eystein Stordal: ASPECTS OF THE EPIDEMIOLOGY OF DEPRESSIONS BASED ON SELF-RATING IN A LARGE GENERAL HEALTH STUDY (THE HUNT-2 STUDY)
254. Viggo Pettersen: FROM MUSCLES TO SINGING: THE ACTIVITY OF ACCESSORY BREATHING MUSCLES AND THORAX MOVEMENT IN CLASSICAL SINGING
255. Marianne Fyhn: SPATIAL MAPS IN THE HIPPOCAMPUS AND ENTORHINAL CORTEX
256. Robert Valderhaug: OBSESSIVE-COMPULSIVE DISORDER AMONG CHILDREN AND ADOLESCENTS: CHARACTERISTICS AND PSYCHOLOGICAL MANAGEMENT OF PATIENTS IN OUTPATIENT PSYCHIATRIC CLINICS
257. Erik Skaaheim Haug: INFRARENAL ABDOMINAL AORTIC ANEURYSMS – COMORBIDITY AND RESULTS FOLLOWING OPEN SURGERY
258. Daniel Kondziella: GLIAL-NEURONAL INTERACTIONS IN EXPERIMENTAL BRAIN DISORDERS
259. Vegard Heimly Brun: ROUTES TO SPATIAL MEMORY IN HIPPOCAMPAL PLACE CELLS
260. Kenneth McMillan: PHYSIOLOGICAL ASSESSMENT AND TRAINING OF ENDURANCE AND STRENGTH IN PROFESSIONAL YOUTH SOCCER PLAYERS
261. Marit Sæbø Indredavik: MENTAL HEALTH AND CEREBRAL MAGNETIC RESONANCE IMAGING IN ADOLESCENTS WITH LOW BIRTH WEIGHT
262. Ole Johan Kemi: ON THE CELLULAR BASIS OF AEROBIC FITNESS, INTENSITY-DEPENDENCE AND TIME-COURSE OF CARDIOMYOCYTE AND ENDOTHELIAL ADAPTATIONS TO EXERCISE TRAINING
263. Eszter Vanky: POLYCYSTIC OVARY SYNDROME – METFORMIN TREATMENT IN PREGNANCY
264. Hild Fjærtoft: EXTENDED STROKE UNIT SERVICE AND EARLY SUPPORTED DISCHARGE. SHORT AND LONG-TERM EFFECTS
265. Grete Dyb: POSTTRAUMATIC STRESS REACTIONS IN CHILDREN AND ADOLESCENTS
266. Vidar Fykse: SOMATOSTATIN AND THE STOMACH
267. Kirsti Berg: OXIDATIVE STRESS AND THE ISCHEMIC HEART: A STUDY IN PATIENTS UNDERGOING CORONARY REVASCULARIZATION
268. Björn Inge Gustafsson: THE SEROTONIN PRODUCING ENTEROCHROMAFFIN CELL, AND EFFECTS OF HYPERSEROTONINEMIA ON HEART AND BONE

2006

269. Torstein Baade Rø: EFFECTS OF BONE MORPHOGENETIC PROTEINS, HEPATOCYTE GROWTH FACTOR AND INTERLEUKIN-21 IN MULTIPLE MYELOMA
270. May-Britt Tessem: METABOLIC EFFECTS OF ULTRAVIOLET RADIATION ON THE ANTERIOR PART OF THE EYE
271. Anne-Sofie Helvik: COPING AND EVERYDAY LIFE IN A POPULATION OF ADULTS WITH HEARING IMPAIRMENT
272. Therese Standal: MULTIPLE MYELOMA: THE INTERPLAY BETWEEN MALIGNANT PLASMA CELLS AND THE BONE MARROW MICROENVIRONMENT

273. Ingvild Saltvedt: TREATMENT OF ACUTELY SICK, FRAIL ELDERLY PATIENTS IN A GERIATRIC EVALUATION AND MANAGEMENT UNIT – RESULTS FROM A PROSPECTIVE RANDOMISED TRIAL
274. Birger Henning Endreseth: STRATEGIES IN RECTAL CANCER TREATMENT – FOCUS ON EARLY RECTAL CANCER AND THE INFLUENCE OF AGE ON PROGNOSIS
275. Anne Mari Aukan Rokstad: ALGINATE CAPSULES AS BIOREACTORS FOR CELL THERAPY
276. Mansour Akbari: HUMAN BASE EXCISION REPAIR FOR PRESERVATION OF GENOMIC STABILITY
277. Stein Sundstrøm: IMPROVING TREATMENT IN PATIENTS WITH LUNG CANCER – RESULTS FROM TWO MULITCENTRE RANDOMISED STUDIES
278. Hilde Pleym: BLEEDING AFTER CORONARY ARTERY BYPASS SURGERY - STUDIES ON HEMOSTATIC MECHANISMS, PROPHYLACTIC DRUG TREATMENT AND EFFECTS OF AUTOTRANSFUSION
279. Line Merethe Oldervoll: PHYSICAL ACTIVITY AND EXERCISE INTERVENTIONS IN CANCER PATIENTS
280. Boye Welde: THE SIGNIFICANCE OF ENDURANCE TRAINING, RESISTANCE TRAINING AND MOTIVATIONAL STYLES IN ATHLETIC PERFORMANCE AMONG ELITE JUNIOR CROSS-COUNTRY SKIERS
281. Per Olav Vandvik: IRRITABLE BOWEL SYNDROME IN NORWAY, STUDIES OF PREVALENCE, DIAGNOSIS AND CHARACTERISTICS IN GENERAL PRACTICE AND IN THE POPULATION
282. Idar Kirkeby-Garstad: CLINICAL PHYSIOLOGY OF EARLY MOBILIZATION AFTER CARDIAC SURGERY
283. Linn Getz: SUSTAINABLE AND RESPONSIBLE PREVENTIVE MEDICINE. CONCEPTUALISING ETHICAL DILEMMAS ARISING FROM CLINICAL IMPLEMENTATION OF ADVANCING MEDICAL TECHNOLOGY
284. Eva Tegnander: DETECTION OF CONGENITAL HEART DEFECTS IN A NON-SELECTED POPULATION OF 42,381 FETUSES
285. Kristin Gabestad Nørsett: GENE EXPRESSION STUDIES IN GASTROINTESTINAL PATHOPHYSIOLOGY AND NEOPLASIA
286. Per Magnus Haram: GENETIC VS. AQUIRED FITNESS: METABOLIC, VASCULAR AND CARDIOMYOCYTE ADAPTATIONS
287. Agneta Johansson: GENERAL RISK FACTORS FOR GAMBLING PROBLEMS AND THE PREVALENCE OF PATHOLOGICAL GAMBLING IN NORWAY
288. Svein Artur Jensen: THE PREVALENCE OF SYMPTOMATIC ARTERIAL DISEASE OF THE LOWER LIMB
289. Charlotte Björk Ingul: QUANITIFICATION OF REGIONAL MYOCARDIAL FUNCTION BY STRAIN RATE AND STRAIN FOR EVALUATION OF CORONARY ARTERY DISEASE. AUTOMATED VERSUS MANUAL ANALYSIS DURING ACUTE MYOCARDIAL INFARCTION AND DOBUTAMINE STRESS ECHOCARDIOGRAPHY
290. Jakob Nakling: RESULTS AND CONSEQUENCES OF ROUTINE ULTRASOUND SCREENING IN PREGNANCY – A GEOGRAPHIC BASED POPULATION STUDY
291. Anne Engum: DEPRESSION AND ANXIETY – THEIR RELATIONS TO THYROID DYSFUNCTION AND DIABETES IN A LARGE EPIDEMIOLOGICAL STUDY
292. Ottar Bjerkeset: ANXIETY AND DEPRESSION IN THE GENERAL POPULATION: RISK FACTORS, INTERVENTION AND OUTCOME – THE NORD-TRØNDELAG HEALTH STUDY (HUNT)
293. Jon Olav Drogset: RESULTS AFTER SURGICAL TREATMENT OF ANTERIOR CRUCIATE LIGAMENT INJURIES – A CLINICAL STUDY
294. Lars Fosse: MECHANICAL BEHAVIOUR OF COMPACTED MORSELLISED BONE – AN EXPERIMENTAL IN VITRO STUDY
295. Gunilla Klensmeden Fosse: MENTAL HEALTH OF PSYCHIATRIC OUTPATIENTS BULLIED IN CHILDHOOD
296. Paul Jarle Mork: MUSCLE ACTIVITY IN WORK AND LEISURE AND ITS ASSOCIATION TO MUSCULOSKELETAL PAIN
297. Björn Stenström: LESSONS FROM RODENTS: I: MECHANISMS OF OBESITY SURGERY – ROLE OF STOMACH. II: CARCINOGENIC EFFECTS OF *HELICOBACTER PYLORI* AND SNUS IN THE STOMACH

2007

298. Haakon R. Skogseth: INVASIVE PROPERTIES OF CANCER – A TREATMENT TARGET ? IN VITRO STUDIES IN HUMAN PROSTATE CANCER CELL LINES
299. Janniche Hammer: GLUTAMATE METABOLISM AND CYCLING IN MESIAL TEMPORAL LOBE EPILEPSY
300. May Britt Drugli: YOUNG CHILDREN TREATED BECAUSE OF ODD/CD: CONDUCT PROBLEMS AND SOCIAL COMPETENCIES IN DAY-CARE AND SCHOOL SETTINGS
301. Arne Skjold: MAGNETIC RESONANCE KINETICS OF MANGANESE DIPYRIDOXYL DIPHOSPHATE (MnDPDP) IN HUMAN MYOCARDIUM. STUDIES IN HEALTHY VOLUNTEERS AND IN PATIENTS WITH RECENT MYOCARDIAL INFARCTION
302. Siri Malm: LEFT VENTRICULAR SYSTOLIC FUNCTION AND MYOCARDIAL PERFUSION ASSESSED BY CONTRAST ECHOCARDIOGRAPHY
303. Valentina Maria do Rosario Cabral Iversen: MENTAL HEALTH AND PSYCHOLOGICAL ADAPTATION OF CLINICAL AND NON-CLINICAL MIGRANT GROUPS
304. Lasse Løvstakken: SIGNAL PROCESSING IN DIAGNOSTIC ULTRASOUND: ALGORITHMS FOR REAL-TIME ESTIMATION AND VISUALIZATION OF BLOOD FLOW VELOCITY
305. Elisabeth Olstad: GLUTAMATE AND GABA: MAJOR PLAYERS IN NEURONAL METABOLISM
306. Lilian Leistad: THE ROLE OF CYTOKINES AND PHOSPHOLIPASE A_2S IN ARTICULAR CARTILAGE CHONDROCYTES IN RHEUMATOID ARTHRITIS AND OSTEOARTHRITIS
307. Arne Vaaler: EFFECTS OF PSYCHIATRIC INTENSIVE CARE UNIT IN AN ACUTE PSYCIATHRIC WARD
308. Mathias Toft: GENETIC STUDIES OF LRRK2 AND PINK1 IN PARKINSON'S DISEASE
309. Ingrid Løvold Mostad: IMPACT OF DIETARY FAT QUANTITY AND QUALITY IN TYPE 2 DIABETES WITH EMPHASIS ON MARINE N-3 FATTY ACIDS
310. Torill Eidhammer Sjøbakk: MR DETERMINED BRAIN METABOLIC PATTERN IN PATIENTS WITH BRAIN METASTASES AND ADOLESCENTS WITH LOW BIRTH WEIGHT
311. Vidar Beisvåg: PHYSIOLOGICAL GENOMICS OF HEART FAILURE: FROM TECHNOLOGY TO PHYSIOLOGY
312. Olav Magnus Søndenå Fredheim: HEALTH RELATED QUALITY OF LIFE ASSESSMENT AND ASPECTS OF THE CLINICAL PHARMACOLOGY OF METHADONE IN PATIENTS WITH CHRONIC NON-MALIGNANT PAIN
313. Anne Brantberg: FETAL AND PERINATAL IMPLICATIONS OF ANOMALIES IN THE GASTROINTESTINAL TRACT AND THE ABDOMINAL WALL
314. Erik Solligård: GUT LUMINAL MICRODIALYSIS
315. Elin Tollefsen: RESPIRATORY SYMPTOMS IN A COMPREHENSIVE POPULATION BASED STUDY AMONG ADOLESCENTS 13-19 YEARS. YOUNG-HUNT 1995-97 AND 2000-01; THE NORD-TRØNDELAG HEALTH STUDIES (HUNT)
316. Anne-Tove Brenne: GROWTH REGULATION OF MYELOMA CELLS
317. Heidi Knobel: FATIGUE IN CANCER TREATMENT – ASSESSMENT, COURSE AND ETIOLOGY
318. Torbjørn Dahl: CAROTID ARTERY STENOSIS. DIAGNOSTIC AND THERAPEUTIC ASPECTS
319. Inge-Andre Rasmussen jr.: FUNCTIONAL AND DIFFUSION TENSOR MAGNETIC RESONANCE IMAGING IN NEUROSURGICAL PATIENTS
320. Grete Helen Bratberg: PUBERTAL TIMING – ANTECEDENT TO RISK OR RESILIENCE ? EPIDEMIOLOGICAL STUDIES ON GROWTH, MATURATION AND HEALTH RISK BEHAVIOURS; THE YOUNG HUNT STUDY, NORD-TRØNDELAG, NORWAY
321. Sveinung Sørhaug: THE PULMONARY NEUROENDOCRINE SYSTEM. PHYSIOLOGICAL, PATHOLOGICAL AND TUMOURIGENIC ASPECTS
322. Olav Sande Eftedal: ULTRASONIC DETECTION OF DECOMPRESSION INDUCED VASCULAR MICROBUBBLES
323. Rune Bang Leistad: PAIN, AUTONOMIC ACTIVATION AND MUSCULAR ACTIVITY RELATED TO EXPERIMENTALLY-INDUCED COGNITIVE STRESS IN HEADACHE PATIENTS
324. Svein Brekke: TECHNIQUES FOR ENHANCEMENT OF TEMPORAL RESOLUTION IN THREE-DIMENSIONAL ECHOCARDIOGRAPHY
325. Kristian Bernhard Nilsen: AUTONOMIC ACTIVATION AND MUSCLE ACTIVITY IN RELATION TO MUSCULOSKELETAL PAIN

326. Anne Irene Hagen: HEREDITARY BREAST CANCER IN NORWAY. DETECTION AND PROGNOSIS OF BREAST CANCER IN FAMILIES WITH *BRCA1*GENE MUTATION
327. Ingebjørg S. Juel : INTESTINAL INJURY AND RECOVERY AFTER ISCHEMIA. AN EXPERIMENTAL STUDY ON RESTITUTION OF THE SURFACE EPITHELIUM, INTESTINAL PERMEABILITY, AND RELEASE OF BIOMARKERS FROM THE MUCOSA
328. Runa Heimstad: POST-TERM PREGNANCY
329. Jan Egil Afset: ROLE OF ENTEROPATHOGENIC *ESCHERICHIA COLI* IN CHILDHOOD DIARRHOEA IN NORWAY
330. Bent Håvard Hellum: *IN VITRO* INTERACTIONS BETWEEN MEDICINAL DRUGS AND HERBS ON CYTOCHROME P-450 METABOLISM AND P-GLYCOPROTEIN TRANSPORT
331. Morten André Høydal: CARDIAC DYSFUNCTION AND MAXIMAL OXYGEN UPTAKE MYOCARDIAL ADAPTATION TO ENDURANCE TRAINING

2008

332. Andreas Møllerløkken: REDUCTION OF VASCULAR BUBBLES: METHODS TO PREVENT THE ADVERSE EFFECTS OF DECOMPRESSION
333. Anne Hege Aamodt: COMORBIDITY OF HEADACHE AND MIGRAINE IN THE NORD-TRØNDELAG HEALTH STUDY 1995-97
334. Brage Høyem Amundsen: MYOCARDIAL FUNCTION QUANTIFIED BY SPECKLE TRACKING AND TISSUE DOPPLER ECHOCARDIOGRAPHY – VALIDATION AND APPLICATION IN EXERCISE TESTING AND TRAINING
335. Inger Anne Næss: INCIDENCE, MORTALITY AND RISK FACTORS OF FIRST VENOUS THROMBOSIS IN A GENERAL POPULATION. RESULTS FROM THE SECOND NORD-TRØNDELAG HEALTH STUDY (HUNT2)
336. Vegard Bugten: EFFECTS OF POSTOPERATIVE MEASURES AFTER FUNCTIONAL ENDOSCOPIC SINUS SURGERY
337. Morten Bruvold: MANGANESE AND WATER IN CARDIAC MAGNETIC RESONANCE IMAGING
338. Miroslav Fris: THE EFFECT OF SINGLE AND REPEATED ULTRAVIOLET RADIATION ON THE ANTERIOR SEGMENT OF THE RABBIT EYE
339. Svein Arne Aase: METHODS FOR IMPROVING QUALITY AND EFFICIENCY IN QUANTITATIVE ECHOCARDIOGRAPHY – ASPECTS OF USING HIGH FRAME RATE
340. Roger Almvik: ASSESSING THE RISK OF VIOLENCE: DEVELOPMENT AND VALIDATION OF THE BRØSET VIOLENCE CHECKLIST
341. Ottar Sundheim: STRUCTURE-FUNCTION ANALYSIS OF HUMAN ENZYMES INITIATING NUCLEOBASE REPAIR IN DNA AND RNA
342. Anne Mari Undheim: SHORT AND LONG-TERM OUTCOME OF EMOTIONAL AND BEHAVIOURAL PROBLEMS IN YOUNG ADOLESCENTS WITH AND WITHOUT READING DIFFICULTIES
343. Helge Garåsen: THE TRONDHEIM MODEL. IMPROVING THE PROFESSIONAL COMMUNICATION BETWEEN THE VARIOUS LEVELS OF HEALTH CARE SERVICES AND IMPLEMENTATION OF INTERMEDIATE CARE AT A COMMUNITY HOSPITAL COULD PROVIDE BETTER CARE FOR OLDER PATIENTS. SHORT AND LONG TERM EFFECTS
344. Olav A. Foss: "THE ROTATION RATIOS METHOD". A METHOD TO DESCRIBE ALTERED SPATIAL ORIENTATION IN SEQUENTIAL RADIOGRAPHS FROM ONE PELVIS
345. Bjørn Olav Åsvold: THYROID FUNCTION AND CARDIOVASCULAR HEALTH
346. Torun Margareta Melø: NEURONAL GLIAL INTERACTIONS IN EPILEPSY
347. Irina Poliakova Eide: FETAL GROWTH RESTRICTION AND PRE-ECLAMPSIA: SOME CHARACTERISTICS OF FETO-MATERNAL INTERACTIONS IN DECIDUA BASALIS
348. Torunn Askim: RECOVERY AFTER STROKE. ASSESSMENT AND TREATMENT; WITH FOCUS ON MOTOR FUNCTION
349. Ann Elisabeth Åsberg: NEUTROPHIL ACTIVATION IN A ROLLER PUMP MODEL OF CARDIOPULMONARY BYPASS. INFLUENCE ON BIOMATERIAL, PLATELETS AND COMPLEMENT
350. Lars Hagen: REGULATION OF DNA BASE EXCISION REPAIR BY PROTEIN INTERACTIONS AND POST TRANSLATIONAL MODIFICATIONS
351. Sigrun Beate Kjøtrød: POLYCYSTIC OVARY SYNDROME – METFORMIN TREATMENT IN ASSISTED REPRODUCTION

352. Steven Keita Nishiyama: PERSPECTIVES ON LIMB-VASCULAR HETEROGENEITY: IMPLICATIONS FOR HUMAN AGING, SEX, AND EXERCISE
353. Sven Peter Näsholm: ULTRASOUND BEAMS FOR ENHANCED IMAGE QUALITY
354. Jon Ståle Ritland: PRIMARY OPEN-ANGLE GLAUCOMA & EXFOLIATIVE GLAUCOMA. SURVIVAL, COMORBIDITY AND GENETICS
355. Sigrid Botne Sando: ALZHEIMER'S DISEASE IN CENTRAL NORWAY. GENETIC AND EDUCATIONAL ASPECTS
356. Parvinder Kaur: CELLULAR AND MOLECULAR MECHANISMS BEHIND METHYLMERCURY-INDUCED NEUROTOXICITY
357. Ismail Cüneyt Güzey: DOPAMINE AND SEROTONIN RECEPTOR AND TRANSPORTER GENE POLYMORPHISMS AND EXTRAPYRAMIDAL SYMPTOMS. STUDIES IN PARKINSON'S DISEASE AND IN PATIENTS TREATED WITH ANTIPSYCHOTIC OR ANTIDEPRESSANT DRUGS
358. Brit Dybdahl: EXTRA-CELLULAR INDUCIBLE HEAT-SHOCK PROTEIN 70 (Hsp70) – A ROLE IN THE INFLAMMATORY RESPONSE ?
359. Kristoffer Haugarvoll: IDENTIFYING GENETIC CAUSES OF PARKINSON'S DISEASE IN NORWAY
360. Nadra Nilsen: TOLL.LIKE RECEPTOR – EXPRESSION, REGULATION AND SIGNALING
361. Johan Håkon Bjørngaard: PATIENT SATISFACTION WITH OUTPATIENT MENTAL HEALTH SERVICES – THE INFLUENCE OF ORGANIZATIONAL FACTORS.
362. Kjetil Høydal : EFFECTS OF HIGH INTENSITY AEROBIC TRAINING IN HEALTHY SUBJECTS AND CORONARY ARTERY DISEASE PATIENTS; THE IMPORTANCE OF INTENSITY,, DURATION AND FREQUENCY OF TRAINING.
363. Trine Karlsen: TRAINING IS MEDICINE: ENDURANCE AND STRENGTH TRAINING IN CORONARY ARTERY DISEASE AND HEALTH.
364. Marte Thuen: MANGANASE-ENHANCED AND DIFFUSION TENSOR MR IMAGING OF THE NORMAL, INJURED AND REGENERATING RAT VISUAL PATHWAY
365. Cathrine Broberg Vågbø: DIRECT REPAIR OF ALKYLATION DAMAGE IN DNA AND RNA BY 2-OXOGLUTARATE- AND IRON-DEPENDENT DIOXYGENASES
366. Arnt Erik Tjønna: AEROBIC EXERCISE AND CARDIOVASCULAR RISK FACTORS IN OVERWEIGHT AND OBESE ADOLESCENTS AND ADULTS
367. Marianne W. Furnes: FEEDING BEHAVIOR AND BODY WEIGHT DEVELOPMENT: LESSONS FROM RATS
368. Lene N. Johannessen: FUNGAL PRODUCTS AND INFLAMMATORY RESPONSES IN HUMAN MONOCYTES AND EPITHELIAL CELLS
369. Anja Bye: GENE EXPRESSION PROFILING OF *INHERITED* AND *ACQUIRED* MAXIMAL OXYGEN UPTAKE – RELATIONS TO THE METABOLIC SYNDROME.
370. Oluf Dimitri Røe: MALIGNANT MESOTHELIOMA: VIRUS, BIOMARKERS AND GENES. A TRANSLATIONAL APPROACH
371. Ane Cecilie Dale: DIABETES MELLITUS AND FATAL ISCHEMIC HEART DISEASE. ANALYSES FROM THE HUNT1 AND 2 STUDIES
372. Jacob Christian Hølen: PAIN ASSESSMENT IN PALLIATIVE CARE: VALIDATION OF METHODS FOR SELF-REPORT AND BEHAVIOURAL ASSESSMENT
373. Erming Tian: THE GENETIC IMPACTS IN THE ONCOGENESIS OF MULTIPLE MYELOMA
374. Ole Bosnes: KLINISK UTPRØVING AV NORSKE VERSJONER AV NOEN SENTRALE TESTER PÅ KOGNITIV FUNKSJON
375. Ola M. Rygh: 3D ULTRASOUND BASED NEURONAVIGATION IN NEUROSURGERY. A CLINICAL EVALUATION
376. Astrid Kamilla Stunes: ADIPOKINES, PEROXISOME PROFILERATOR ACTIVATED RECEPTOR (PPAR) AGONISTS AND SEROTONIN. COMMON REGULATORS OF BONE AND FAT METABOLISM
377. Silje Engdal: HERBAL REMEDIES USED BY NORWEGIAN CANCER PATIENTS AND THEIR ROLE IN HERB-DRUG INTERACTIONS
378. Kristin Offerdal: IMPROVED ULTRASOUND IMAGING OF THE FETUS AND ITS CONSEQUENCES FOR SEVERE AND LESS SEVERE ANOMALIES
379. Øivind Rognmo: HIGH-INTENSITY AEROBIC EXERCISE AND CARDIOVASCULAR HEALTH
380. Jo-Åsmund Lund: RADIOTHERAPY IN ANAL CARCINOMA AND PROSTATE CANCER

2009

381. Tore Grüner Bjåstad: HIGH FRAME RATE ULTRASOUND IMAGING USING PARALLEL BEAMFORMING
382. Erik Søndenaa: INTELLECTUAL DISABILITIES IN THE CRIMINAL JUSTICE SYSTEM
383. Berit Rostad: SOCIAL INEQUALITIES IN WOMEN'S HEALTH, HUNT 1984-86 AND 1995-97, THE NORD-TRØNDELAG HEALTH STUDY (HUNT)
384. Jonas Crosby: ULTRASOUND-BASED QUANTIFICATION OF MYOCARDIAL DEFORMATION AND ROTATION